UNIVERSIDADE ESTADUAL DE CAMPINAS
FACULDADE DE ENGENHARIA ELÉTRICA E DE COMPUTAÇÃO

Julian Leonel Pita Ruiz

CMOS-Compatible Compact Photonic Antennas

Antenas fotônicas compactas compatíveis com a tecnologia CMOS

Campinas
2018

Julian leonel Pita Ruiz

CMOS-Compatible Compact Photonic Antennas

Antenas fotônicas compactas compatíveis com a tecnologia CMOS

Thesis presented to the Faculty of Electrical and Computing Engineering of the University of Campinas in partial fulfillment of the requirements for the degree of Doctor, in the area of Telecommunications and Telematics.

Tese apresentada à Faculdade de Engenharia Elétrica e de Computação da Universidade Estadual de Campinas como parte dos requisitos exigidos para a obtenção do título de Doutor em Engenharia Elétrica, na Àrea de Telecomunicações e Telemática.

Supervisor/Orientador: Lucas Heitzmann Gabrielli

Este exemplar corresponde à versão final da tese defendida pelo aluno Julián Leonel Pita Ruiz, e orientada pelo Prof. Dr. Lucas Heitzmann Gabrielli .

Campinas
2018

Agência(s) de fomento e nº(s) de processo(s): CAPES

Ficha catalográfica
Universidade Estadual de Campinas
Biblioteca da Área de Engenharia e Arquitetura
Rose Meire da Silva - CRB 8/5974

P68c

Pita Ruiz, Julian Leonel, 1989-
CMOS-compatible compact photonic antennas / Julian Leonel Pita Ruiz. – Campinas, SP : [s.n.], 2018.

Orientador: Lucas Heitzmann Gabrielli.
Tese (doutorado) – Universidade Estadual de Campinas, Faculdade de Engenharia Elétrica e de Computação.

1. Antenas. 2. Fotônica. 3. Dispositivos dielétricos. I. Lucas Heitzmann Gabrielli, 1982-. II. Universidade Estadual de Campinas. Faculdade de Engenharia Elétrica e de Computação. III. Título.

Informações para Biblioteca Digital

Título em outro idioma:

Antenas fotônicas compactas compatíveis com a tecnologia CMOS

Palavras-chave em inglês:
Antena
Antenna arrays
Photonics
CMOS
Área de concentração: Telecomunicações e Telemática
Titulação: Doutor em Engenharia Elétrica
Banca examinadora:
Lucas Heitzmann Gabrielli [Orientador]
Danilo Henrique Spadoti
Roberto Ricardo Panepucci
Paulo Clóvis Dainese Junior
Cesar José Bonjuani Pagan
Data de defesa: 03-10-2018
Programa de Pós-Graduação: Engenharia Elétrica

Comissão Julgadora – Tese de Doutorado

Candidato: Julian leonel Pita Ruiz **RA:** 153935

Data da defesa: 03 de Outubro de 2018

Título da Tese: "CMOS-Compatible Compact Photonic Antennas."

Prof. Dr. Lucas Heitzmann Gabrielli (Presidente, FEEC/UNICAMP)
Prof. Dr. Danilo Henrique Spadoti (UNIFEI)
Dr. Roberto Ricardo Panepucci (CTI – Renato Archer)
Prof. Dr. Paulo Clóvis Dainese Junior (IFGW/UNICAMP)
Prof. Dr. Cesar José Bonjuani Pagan (FEEC/UNICAMP)

A ata de defesa, com as respectivas assinaturas dos membros da Comissão Julgadora, encontra-se no processo de vida acadêmica do aluno.

To my parents Alicia and Angel.
To my son Santiago.
To my nephew Jorge.
To my sisters Ana and Vanessa.
To my beautiful wife Nataly.

"If you are neutral in situations of injustice, you have chosen the side of the oppressor".
—Desmond Mpilo Tutu

Acknowledgements

During my doctorate the support of many people was essential to achieve this thesis, so I want to leave here my sincere thanks to these people. Not without first expressing my special thanks to my parents. Thank you for all the effort and dedication you daily made so that I could have the opportunity to attend university. Ana, thank you very much for helping me take care of Santy, and for your support and affection. And, of course, the engine of my life, my dear wife Nataly, thank you for all your work and for your unconditional love.

To my advisor, Lucas Gabrielli, my widest thanks for sharing his knowledge and for his great effort to provide me with all the required tools to develop a good doctorate. I also thank Professor Hugo Figueroa for opening the doors to the Advanced Electromagnetism and Computational Research Group (GEMAC).

I thank Professor Paulo Dainese, first for receiving me in his research group, and second, for his contributions and criticisms that were instrumental in bringing this work to a successful conclusion. I also thank Professor Hugo Fragnito for allowing me to work in the Optical Communications Laboratory (LCO).

To Professor Ivan Aldaya my special thanks, since during his postdoctoral stay at the LCO he worked on my side most of the time. His reflections about my work and, above all, his reflections on history made the dawns of work more bearable.

Sincere thanks to all the people of LCO: Paulão, Vagner, Maicon, Simone, Eliane, Francinvaldo, and Erick, thanks for all these years. I also thank CCS-nano for its infrastructure and staff, Raluca, Luana, Fred, Emilio, and all others, thank you very much for the support during the manufacturing processes. I also thank the LPD staff, especially Totó, who supported me a lot in the clean room.

To my colleague from the National University of Colombia Luis de Oro, thank you for informing me about the scholarships of the OEA that offer the possibility of studying in Brazil. And a special thanks to Professor Ruben Romero and Professor Jozue Vieira Filho who, even without obtaining a grant from the OEA, they offered me the opportunity to study here. I also thank the CAPES, CNPq, FAPESP, and Fotonicom for the financial support granted during the period of my doctorate.

To my friends, Saúl, Flaco, Luisão, Pipe, Diego, Hansen, Darwin, Jhonattan, Juanchito, Leandro, Iñaki, and Primãos, we will move on.

Resumo

A área das antenas fotônicas desenvolveu-se muito nos últimos anos, com aplicações diretas em detecção de luz e avaliação de distância (LIDAR), microscopia, fotovoltaica, holografia, e as comunicações inter-chip e intra-chip — entre outras. Da ampla variedade de antenas relatadas na literatura, as antenas fotônicas compatíveis com a tecnologia de semicondutores de óxido metálico complementar (CMOS) são candidatas promissoras para resolver o gargalo das comunicações em nível de chip, e também prometem levar a tecnologia LIDAR para aplicações comerciais viáveis de última geração como os carros autônomos. Dentre as antenas propostas na literatura a antena do tipo grade é a mais utilizada devido a sua facilidade de projeção e fabricação, e a seu desempenho. Embora a antena de tipo grade seja adequada para várias aplicações, esta ainda tem várias desvantagens. Entre estas, sua forte dependência da polarização e do comprimento de onda, sua direção de radiação máxima inclinada, e seu desempenho ineficiente quando projetada com uma área efetiva próxima a um comprimento de onda operacional.

Nesta tese, apresentamos o projeto de antenas com desenhos não-intuitivos utilizando algoritmos de otimização do estado da arte, para aplicações em acoplamento da fibra para o chip, e também para seu uso em arranjos. Por um lado, produzimos conhecimento local na área de fabricação e caracterização de antenas de silício sobre isolante (SOI), desenvolvendo receitas de fabricação com alta repetibilidade em cada etapa do processo. Por outro lado, mostramos que as antenas otimizadas podem superar algumas limitações das antenas tipo grade. As simulações mostram que nosso projeto de antena para acoplamento atinge uma eficiência de acoplamento vertical de $-6.3\,\mathrm{dB}$ e uma largura de banda operacional de $3\,\mathrm{dB}$ de $60\,\mathrm{nm}$. Sendo esta a menor antena para acoplamento com esse nível de desempenho na literatura, ela ocupa apenas $15\,\%$ do espaço de uma antena convencional tipo grade para acoplamento, o que possibilita seu uso para acoplamento em fibras com múltiplos núcleos. Também mostramos experimentalmente pela primeira vez uma antena com radiação totalmente vertical para utilização em arranjos com um tamanho compacto, perto do comprimento de onda, com uma área de $1.78\,\mu\mathrm{m} \times 1.78\,\mu\mathrm{m}$, e uma largura de banda operacional maior do que $100\,\mathrm{nm}$. Finalmente, mostramos um arranjo de antenas passivo integrado de 8 elementos distribuídos seguindo o desenho aperiódico da espiral de Fermat apresentando um nível de lóbulo lateral (SLL) cerca de $1\,\mathrm{dB}$ menor que o equivalente periódico do mesmo tamanho num comprimento de onda de $1550\,\mathrm{nm}$. Além disso, também se usou um modulador espacial de luz (SLM) a um comprimento de onda visível para emular arranjos de antenas maiores, mostrando que a distribuição dos elementos seguindo a espiral Fermat é capaz de reduzir o SLL para arranjos de até 64 elementos espaçados até $581\,\lambda$.

Abstract

The field of photonic antennas has become an area of intensive study in recent years, with direct applications in light detection and ranging (LIDAR), microscopy, sensors, photovoltaics, holography, and inter- and intra-chip communications — among several others. Of the great variety of antennas reported in the literature, the photonic antennas compatible with the well-established complementary metal–oxide–semiconductor (CMOS) technology are promising candidates to solve the chip-level communication bottleneck, and also promise to make the LIDAR technology a viable commercial application for autonomous vehicles. Among the antennas proposed in the literature we find that the grating-type antenna is the most widely used due to its straightforward design and manufacture, and its performance. However, even if grating antennas are suitable for several applications, they still present several drawbacks. In particular, their radiation properties are strongly dependent on polarization and wavelength, their direction of maximum radiation does not occur at broadside direction, and they are power inefficient when designed with an effective area close to the operating wavelength.

In this thesis, we present the design of antennas with counterintuitive designs obtained by means of state-of-the-art optimization algorithms for applications in fiber coupling to the chip, and also for use as radiation element in large-scale arrays. We produced, on the one hand, local knowledge in the manufacturing and characterization of silicon-on-insulator (SOI) antennas, developing manufacturing recipes with high repeatability at each step of the process. On the other hand, we show that optimized antennas can overcome some limitations of grating-type antennas. Simulations show that our antenna designed for coupling achieves an efficiency in the vertical direction of $-6.3\,\mathrm{dB}$ and an operating $3\,\mathrm{dB}$ bandwidth of $60\,\mathrm{nm}$. This represents the smallest antenna designed for coupling at this performance level in the literature, it occupies only $15\,\%$ of the footprint of a conventional grating antenna, which in turn enables its use in multicore fibers. We also demonstrated experimentally for the first time an antenna with vertical radiation and a compact footprint for use in arrays. Its dimensions are close to the operation wavelength, and it has an area $1.78\,\mu\mathrm{m} \times 1.78\,\mu\mathrm{m}$ and an operational bandwidth exceeding $100\,\mathrm{nm}$. Finally, we show that a passive integrated 8-element array antenna distributed following the aperiodic design of the Fermat spiral shows a side lobe level (SLL) approximately $1\,\mathrm{dB}$ lower than a periodic array of the same size, both operating at a wavelength of $1550\,\mathrm{nm}$. In addition, we also use a spatial ligth modulator (SLM) at visible wavelength to emulate larger arrays, showing that the Fermat spiral successfully reduces the SLL in for arrays with up to 64-elements spaced by $581\,\lambda$.

List of Figures

List of Tables

List of abbreviations

AF array factor.

AFM atomic force microscopy.

BOBYQA bound optimization by quadratic approximation.

BOX buried oxide.

CAD computer-aided design.

CCD charge-coupled device.

CCP capacitively coupled plasma.

CCS Semiconductor Components Center.

CMOS complementary metal–oxide–semiconductor.

CO colimator.

COBYLA constrained optimization by linear approximations.

CTI Centro de Pesquisas Renato Archer.

DAC digital to analog converter.

DE differential evolution.

DI deionized.

FDTD finite-difference time domain.

FEM finite element method.

FWHM full-width at half maximum.

GDSII graphic data system II.

GEMAC Applied and Computational Electromagnetics Group.

HDMS hexamethyldisilazane.

HNBW first-null beamwidth.

HPBW half-power beamwidth.

ICP inductively coupled plasma.

IEEE Institute of Electrical and Electronics Engineers.

IP internet protocol.

LCO Optical Communications Laboratory.

LF lensed fiber.

LIDAR light detection and ranging.

LP linear polarizer.

MMA method of moving asymptotes.

NA numerical aperture.

NIR near-infrared.

OPA optical phased arrays.

OSA optical spectrum analyzer.

PC polarization controller.

PEC perfect electric conductor.

PICs Photonic integrated circuits.

PRAXIS principal axis.

PS piezo stage.

RADAR radio detection and ranging.

RF radio frequency.

RIE reactive ion etch.

SEM scanning electron microscope.

SLED superluminescent diode.

SLL side lobe level.

SLM spatial ligth modulator.

SNOPT sparse nonlinear optimizer.

SOI silicon-on-insulator.

SWIR shortwave-infrared.

TE transverse electric.

UNICAMP University of Campinas.

VNI Visual Networking Index.

Contents

Chapter 1

Introduction

Due to the dramatic expansion of the internet of things, and the big boost of mobile applications, optical communication systems are required to offer increased bandwidth and lower power consumption, both in distances at the data center level, and long distances. According to the Cisco Visual Networking Index (VNI), the global internet protocol (IP) annual traffic is expected to reach 3.3 ZB by 2021, which is almost three-fold the traffic registered in 2016, 1.2 ZB [1]. Regarding the energy consumption at the chip level, it is estimated that in 2010, the electricity consumption represented between 1.1 % and 1.5 % of the global consumption [2]. Equally, it is expected that the energy costs in a typical data-center will be double every five years [3].

In this context, silicon photonics has emerged as an attractive approach for component miniaturization, thereby making it possible the reduction of energy consumption, and the increased bandwidth. The miniaturization capacity of silicon photonics is consequence of the high refractive index contrast of the materials employed in the CMOS process, mainly silicon dioxide and silicon, whose refractive indices in the near-infrared (NIR) region are approximately 1.45 and 3.45, respectively. Given its compatibility with the CMOS technology patented in 1967 [4], silicon photonics can take advantage of all the mature manufacturing infrastructure. In addition, is has a possibility of integrating the optical devices directly with microelectronics to perform data processing.

1.1 Photonic antennas

Antennas operating at optical frequencies are becoming an essential part in many applications, such as: spectroscopy [5–7], communications [8–11], photovoltaic [12, 13], optical sensors [14, 15], holography [16], and LIDAR [17–19]. Furthermore, these antennas are expected to play a key role in communications at chip level, offering unprecedented bandwidth and energy efficiency. To fulfill these bandwidth and energy requirements, all-dielectric antennas were developed [16]. Their easier integration with the well-established SOI platform, in combination with a more efficient feeding through conventional waveguides,

and their lower wavelength dependence of their radiation pattern (compared to the metallic antennas), makes this type of antennas a promising candidate to solve the data transmission bottleneck at the chip level.

Guglielmo Marconi introduced the term *antenna* in the context of radio in 1895 while performing his first wireless transmission experiments in Salvan (Switzerland). Marconi, however, did not use the term antenna in his patents but until his speech of the Nobel Prize in 1909 [20]. The first document that uses the word antenna for an electromagnetic transmitter, is an article by André-Eugène Blondel entitled "Sur la théorie des antennes dans la télégraphie sans fil", published in 1898. Since then, the concept of *antenna* has evolved over the years, for example the Institute of Electrical and Electronics Engineers (IEEE) defines the antenna as that part of a transmitter system or receiver specifically designed to radiate or receive electromagnetic waves (IEEE Std. 145-1983) [21]. For Balanis [22], the antenna is a transition structure between a region where the electromagnetic wave is guided and free space. The representation of the guided wave is performed by voltages and currents (wires and transmission lines) or fields (waveguides), whereas in free space they are represented by fields [23]. The purpose of a transmission antenna is to radiate the supplied power with suitable features for a particular application. There are applications where a specific near-field radiation pattern is required, while in other applications the far-field pattern is of interest. For instance, for coupling light between a photonic antenna and an optical fiber a uniform near-field radiation pattern without secondary spots is desired, whereas in applications of inter-chip direct communication a dynamic far-field radiation patterns would be desirable [24, 25].

One of the main applications of a single photonic antenna operating in near-field is the communication between photonic chips through an optical fiber, as shown in Fig. 1.1(a). Despite the significant advances in silicon photonics, due to the dimensions mismatch of the nanophotonic waveguides and the standard telecommunications fibers makes the communication among them to remain a challenge that still requires a commercially viable solution. Just as a reference, the direct edge coupling between a cleaved fiber and a silicon waveguide suffers an unacceptable loss of more than 30 dB [26]. In Fig. 1.1(b) we observe the cross sections of a standard single-mode fiber with a core diameter of 8.2 µm and a silicon waveguide of a 220 nm×450 nm cross-section. Therefore, the coupling is carried out between structures with dimensions that differ by almost two orders of magnitude, leading to a large modal mismatch and a significant power loss. In the last years several methods have been proposed to perform coupling. They can be roughly divided in two groups: in-plane and out-of-plane solutions. In general, in-plane coupling shows greater efficiency and bandwidth, but it is extremely sensitive to misalignment, it can only be located at the edge of the chip, and it requires careful post-processing that includes cutting and polishing. On the other hand, in regards to out-of-plane coupling, its performance strongly depends on the state-of-polarization and the wavelength, it presents lower efficiency and a narrower

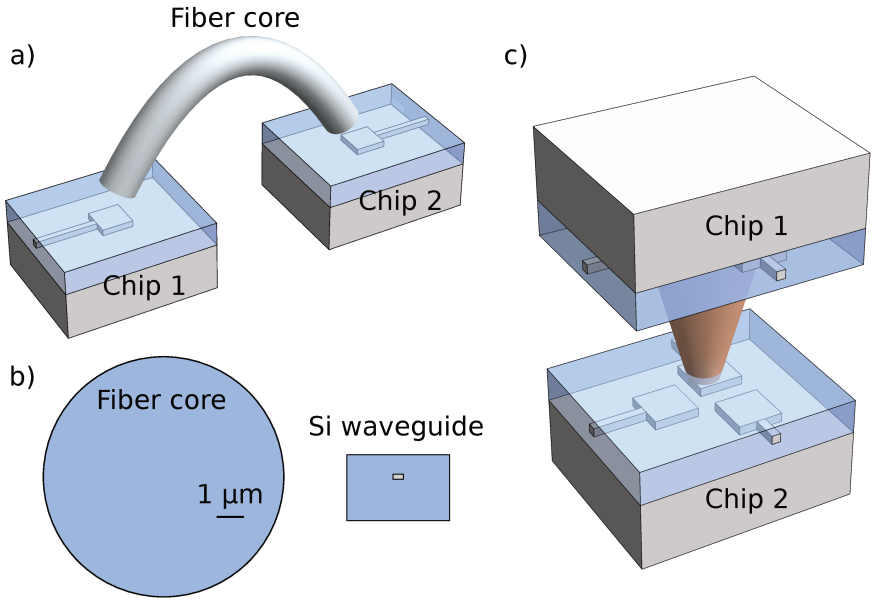

Figure 1.1: **Chip-level interconnections illustration**. (a) Fiber-to-chip optical interconnect. (b) Transverse section of silicon waveguide and a single mode fiber core, drawn to scale. (c) Chip-to-chip optical interconnect.

bandwidth than in-plane coupling. However, it is much more tolerant to miss-alignment, it does not require any post-processing and can be located anywhere chip.

As long as far-field applications is concerned, such as chip-to-chip communication shown in Fig. 1.1 (c), arrays of several antennas are an attractive solution mainly due to their improved radiation gain and superior directivity [22]. When working with several antennas, however, new challenges appear, since in the uniform array of antennas where the separation of elements is greater than half the operating wavelength (λ) and the size of the antenna exceeds λ, the radiation pattern presents undesired secondary radiation lobes with power equal to that of the main radiation lobe [22, 23]. These high-power secondary lobes are especially critical in antenna arrays that operate in the visible and infrared wavelengths, due to the constraints imposed by the fabrication processes. Last generation of CMOS-compatible integrated photonic platform still limits the spatial resolution of each antenna element, as well as its separation. This separation is even greater than several λ-s when the feeding network is implemented in the same chip layer.

1.2 Aim of the thesis

While the speed of data processing and the chip integration density evolve as the transistor size decreases, the ability to transfer data into the chip not doing so, making this an unresolved system bottleneck. In this document, we present the design, fabrication and characterization of photonic antennas for chip-level interconnection, both in near-field and far-field regime. With our devices we seek to occupy less chip area

than those presented previously in the literature. At the same time, we seek to maintain performance similar to its counterparts and even improve some critical characteristics to make possible its use on a large-scale integration. To design our SOI-compatible devices, we use last-generation optimization algorithms. The devices are then manufactured using electron beam lithography when they are maked in-home and optical lithography when they are fabricated at the commercial foundry.

For our devices the following characteristics are desired either for near-field and far-field applications:

- Compatibility with CMOS technology.
- Design on standard SOI platform.
- Single radiation lobe.
- Direction of maximum radiation perpendicular to the substrate (vertical).
- Feeding by conventional single-mode silicon waveguides.

In regards to the single antenna for near-field coupling applications, it is sought to obtain a device smaller than those reported to date, aiming its use also in multicore fibers. In addition, this design must be an out-of-plane coupler, and must also be fully etched to simplify the fabrication process. On the other hand, for far-field applications, more specifically in arrangements of photonic antennas, it is desired to implement the first a $2d$ aperiodic array of optimized radiating elements with a footprint close to the operation wavelength. Thus, enabling arrays with reduced secondary radiation lobes, which is essential to decrease crosstalk and interference.

1.3 Thesis organization

In Chapter 2, we begin by defining the metrics employed to evaluate the performance of the photonic antennas and, then, we present a brief description of their evolution in this last decade. Afterwards, in section 2.2 we list the applications of photonic antennas that, in our opinion are the most important, paying special attention to antennas used to fiber-to-chip coupling. In section 2.3 we present a brief theory of antenna arrays, alongside with a summary of previous works on CMOS-compatible arrays. Finally, we mention the challenges that are currently facing in this field.

In Chapter 3, the instrumentation and fabrication procedures developed in our laboratory are described. We first make a detailed description of each step of the antenna fabrication process and, then, we discuss the details of the characterization setups.

In Chapter 4, we describe the design process and the characterization of two single-element antennas. First, in section 4.1, the design process of an antenna element

for coupling applications is analyzed, describing the employed optimization methods and the challenges faced during this process. Next, we analyzed the performance of our device compared to the state-of-the-art solutions. Then, in the section 4.2, we present the design of an ultra-compact antenna that is suitable to be used as radiation element in array antenna. Finally, we compared the performance of the optimized antenna with the one widely used in large-scale $2d$ photonic arrays.

In Chapter 5, we experimentally demonstrate the SLL reduction in CMOS-compatible integrated photonic antennas. By aperiodically arranging the elements according to the Fermat spiral, we show that even in arrays of few widely spaced elements the SLL can be reduced. Finally, in Chapter 6 we draw the main conclusions and we present the future opportunities emerging from this work.

1.4 Publications

The work described in this thesis was conducted during four years of study of PhD in the facilities of the University of Campinas (UNICAMP). This time was divided between the processes of design, fabrication and characterization of novel integrated photonic devices. The design process was carried out in the Applied and Computational Electromagnetics Group (GEMAC) of the School of Electrical and Computer Engineering, later, the devices were fabricated at the Semiconductor Components Center (CCS)-Nano facilities while the third-party fabrication was performed at IMEC/Europractice. Finally, the characterization of the devices was carried out in collaboration with the Optical Communications Laboratory (LCO) of the Physics Institute "Gleb Wataghin".

Journal papers

1. **Pita, J. L.**, Aldaya, I., Santana, O. J., Dainese, P., and Gabrielli, L. H. Side-lobe level reduction in bio-inspired optical phased-array antennas. *Optics express*, 25(24), 30105-30114. (2017).

2. Aldaya, I., Gil-Molina, A., **Pita, J. L.**, Gabrielli, L. H., Fragnito, H. L., and Dainese, P. Nonlinear carrier dynamics in silicon nano-waveguides. *Optica*, 4(10), 1219-1227. (2017).

3. **Pita, J. L.**, Aldaya, I., Dainese, P., Hernandez-Figueroa, H. E., and Gabrielli, L. H. Design of a compact CMOS-compatible photonic antenna by topological optimization. *Optics express*, 26(3), 2435-2442. (2018).

4. Aldaya, I., Gil-Molina, A., **Pita, J. L.**, Gabrielli, L. H., Fragnito, H. L., and Dainese, P. Optical free-carrier generation in silicon nano-waveguides at 1550 nm. *Applied Physics Letters*, 112(25), 251104. (2018).

5. Lamilla, E., Faria, M., Aldaya, I., Jarschel, P. F., **Pita, J. L.**, and Dainese, P. "Characterization of surface-states in a hollow core photonic crystal fiber," *Optics express*, 26(25), 32554-32564. (2018).

Conference papers

6. **Pita, J. L.**, Dainese, P. C., Hernandez-Figueroa, H. E., and Gabrielli, L. H. (2016, Jun). Ultra-compact broadband dielectric antenna. In *CLEO: Science and Innovations (pp. SM3G-7)*. Optical Society of America.

7. Aldaya, I., Gil-Molina, A., **Pita, J. L.**, Fragnito, H. L., and Dainese, P. (2017, Jun). Lifetime dependence on carrier density in silicon nanowires. In *The European Conference on Lasers and Electro-Optics (p. CKP-4)*. Optical Society of America.

8. Gabrielli, L. H., de Oliveira, L. P., Malheiros-Silveira, G. N., **Pita, J. L.**, and Hernandez-Figueroa, H. E. (2017, Aug). Sparse array of dielectric resonator antennas for ultra-wide band applications. In *Microwave and Optoelectronics Conference (IMOC)*, 2017 SBMO/IEEE MTT-S International (pp. 1-4). IEEE.

9. Aldaya, I., Dainese, P., Gil-Molina, A., **Pita, J. L.**, and Fragnito, H. L. (2017, Aug). Characterization of nonlinear carrier dynamics in silicon strip nanowaveguides. In *Microwave and Optoelectronics Conference (IMOC)*, 2017 SBMO/IEEE MTT-S International (pp. 1-4). IEEE.

10. **Pita, J. L.**, Aldaya, I., Santana, O. J., de Araujo, L. E., Dainese, P., and Gabrielli, L. H. (2018, May). Side-lobe Level Reduction in Two-dimensional Optical Phased Array Antennas. In *CLEO: Science and Innovations (pp. JW2A-58)*. Optical Society of America.

11. Gil-Molina, A., Aldaya, I., **Pita, J. L.**, Gabrielli, L. H., Fragnito, H. L., and Dainese, P. (2018, May). Characterization of linear and nonlinear carrier generation in silicon nano-waveguides at 1550 nm. In *CLEO: Science and Innovations (pp. JTu2A-71)*. Optical Society of America.

12. Aldaya, I., Gil-Molina, A., **Pita, J. L.**, Gabrielli, L. H., Fragnito, H. L., and Dainese, P. (2018, May). Probing free-carrier recombination in silicon strip nano-waveguides. In *CLEO: QELS-Fundamental Science (pp. FF1E-8)*. Optical Society of America.

13. Lamilla, E., Aldaya, I., Faria, M. S., Jarschel, P. F., **Pita, J. L.**, and Dainese, P. (2018, Nov). Recovery of highly-dispersive modes using a wavelength-resolved modified S2 imaging method. In *Latin America Optics and Photonics Conference (pp. Th3B-3)*. Optical Society of America.

Chapter 2

Fundamentals of photonic antennas

In recent years the community working on optical antennas has accepted two main definitions of antennas, the most recent being the one described in the introduction and proposed by Balanis [22]. There is a second one, however. This second definition considers as antenna a device that efficiently concentrates free-space optical waves on a localized region, or vice versa [27]. Optical antennas, like radio frequency (RF) antennas, are divided into two types: transmitting antennas and receiving antennas. According to the definitions, an antenna that transforms the confined near-field or a guided electromagnetic wave into free-space optical radiation are classified as transmitting antenna, while, a receiving antenna converts the incident radiation from free space to a confined near-field or a guided electromagnetic waves. Even if optical antennas have been typically made of metallic materials, which support plasmonic resonances, in the last few years, completely dielectric antennas have emerged as a strong alternative. Furthermore, to improve the energy efficiency, flexibility, and radiation properties of a single optical antenna, a significant effort has been devoted to the development of antenna arrays similar to their RF counterparts [27–35]. Such approach allows a significant improvement in directivity, as well as enables the dynamic control of the radiation pattern by adapting both the amplitude and the phase of each antenna element [16, 24, 25].

2.1 Background

In order to understand the performance of an optical antenna, we will describe some parameters below, based on [21–23]

Radiation pattern: it refers to the mathematical function or the graphic representation of the properties of the antenna as a function of a coordinated space, generally spherical. The radiation pattern is usually calculated in the far field. Among the properties that can be represented by the radiation pattern, the most common ones are the radiated power density, the radiation intensity, the directivity, the phase, or the polarization. Generally, radiation patterns are presented normalized with respect to their

maximum value, and are usually expressed in decibels. The parts of the radiation pattern are called lobes, and these can be classified into: major, back, and side lobes (see Fig. 2.1).

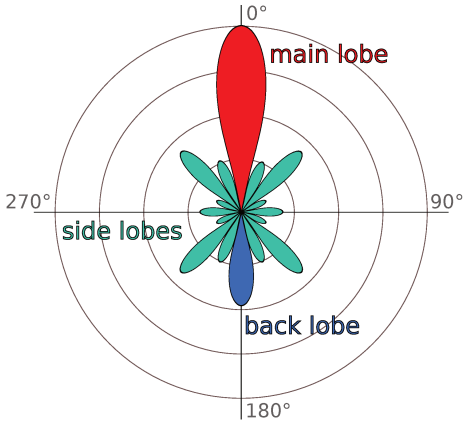

Figure 2.1: **Radiation pattern lobes.** The major part of the radiated field in the desired direction is the main lobe. The other parts of the pattern where the radiation is distributed side-wards are known as side lobes, and the lobe, which is exactly opposite to the direction of main lobe is known as back lobe.

Directivity: is the relationship between the radiation intensity in a given direction and the average radiation intensity in all directions. This can be written in mathematical form in the following way:

$$D = \frac{U}{U_0} = \frac{4\pi U}{P_{rad}}, \tag{2.1}$$

where U is the radiation intensity, U_0 is the radiation intensity of an isotopic source, and P_{rad} is the total radiated power. It is important to note that directivity is dimensionless magnitude.

Gain: is the ratio of the intensity in a given direction, and the radiation intensity of an isotopic antenna. This can be expressed as:

$$G = \frac{4\pi U}{P_{in}}. \tag{2.2}$$

where U is the radiation intensity, and P_{in} is the total input power.

Beamwidth: is a parameter related to the radiation diagram. There are two main types of beam width, half-power beamwidth (HPBW), and first-null beamwidth (HNBW). The HPBW refers to the angular range in which the radiated power density is equal to half the maximum power in the direction of maximum radiation, while the HNBW is the angular interval between the two zeros adjacent to the maximum.

Bandwidth: is the frequency range in which the parameters of the antenna meet certain characteristics. The bandwidth is generally determined by the upper and

lower frequencies at which the energy level at the antenna decreases by 1 dB or 3 dB. An important parameter that is deduced from the bandwidth is the central wavelength.

Efficiency: is the ratio between the radiated power and the power delivered to the antenna. Efficiency decreases mainly due to the reflections caused by the impedance mismatch between the feeding waveguide and the antenna, the conduction losses, and the dielectric losses. Another important efficiency is the so-called coupling efficiency, that is the ratio of the power that is being coupled in the desired guided mode to the power handed over the antenna used as a coupler. This efficiency can be expressed either as a percentage or decibels, in this document we will use dB. Apart from observing coupling efficiency, it also important to know the losses by reflection, the power losses due to light radiation in different directions than desired, and coupled power in unwanted modes.

Polarization: it corresponds to the polarization of the electromagnetic fields produced by an antenna, evaluated in the near-field or far-field. The polarization can be linear, circular, or elliptical. Linear polarization can take different orientations, while circular or elliptical polarizations can be right or left (dextrorotatory or levogy), depending on the direction of field rotation.

Effective area: this parameter quantifies the power capture capacity of the antenna when it acts in the receiver side. It is defined as the ratio of the received power and the power flux density of the incident wave.

Compactness: the area occupied by the antenna plays an important role in the density and overall chip cost, since a larger area leads to an decrease the integration.

Ease of manufacturing: a CMOS-compatible process is highly recommended, since this technology is mature enough and it accounts for multiple third-party factories. It is also important that the manufacturing process to be as simple as possible, giving preference to processes with a single lithography and corrosion step. A higher number of processing stages will increase both the complexity and cost. On the other hand, designing high-performance antennas with a simple manufacturing process and using CMOS-compatible materials can be a great challenge because the high contrast index of the materials used in the technology, which results in a high field confinement. Another important point to take into account is the unwanted requirement of some additional post-processing, such as cutting and polishing the chip.

Flexibility and operation tolerance: the antenna must have flexibility in terms of their position within the chip. It must also be tolerant and robust to misalignment in order to facilitate the characterization process and its packaging. Tolerance to measuring misalignment can be expressed in shifted micrometers to get a power loss of 1 dB. This misalignment usually occurs due to thermal variation that causes a change in the position or angle of the fiber.

In the beginning, optical nanometric-scale antennas were born inspired by the microscopy, so they were used as a device designed to efficiently concentrate radiation

from free propagation, and vice versa. Edward Hutchinson Synge was the first to propose the use of metallic nanoparticles to confine the optical field as early as 1928. Later on, in 1985, John Wessel demonstrated that using a single gold particle the diffraction limit can be overcome in the optical devices resolution up to 10 nm [36]. Nowadays, the design of metallic nanoantenas at RF frequencies is well established and it is sought to take advantage of all this knowledge to use it at optical frequencies. The design of metallic antennas at optical frequencies, however, poses new challenges because, in contrast to what happens at RF frequencies, the approximation of metals as perfect electric conductor (PEC) is not valid. The electric fields can penetrate into the metals, therefore, the ohmic losses are higher than in RF [37], and the response of the optical metallic nanoantennas is drastically affected. The first metallic nanoantenas were built of gold and presented an enormous difficulties in their feeding networks, resulting in a reduced efficiency [27, 38]. Another drawback of these nanoantennas is that due to their resonant nature, their radiation pattern depends significantly on the wavelength and, consequently, they operate with a limited bandwidth.

The main types of optical metallic antennas that have been experimentally demonstrated are the dipole antennas, bowtie antennas and Yagi-Uda antennas, whose scale designs are presented in Fig. 2.2. The dipole antennas are simple to fabricate compared to the other types of antennas, and they offer a high electric field confinement factor. This last advantage becomes an important feature when the gap size is reduced [39–41]. On the other hand, bowtie-type nanoantennas have a lower confinement factor because they have a larger metal area, which also causes higher dissipative losses [42–44]. Finally, Yagi-Uda nanoantennas present a high directivity but a narrow operation bandwidth, since they are tuned at the plasmonic resonance frequency. Its directivity, hence, decreases rapidly for frequencies not matching these resonances and, as a result, this type of antenna is not very useful for broadband practical applications [45–47].

Afterwards, due to the low loss of dielectric materials at optical frequencies, dielectric antennas were proposed as an alternative to their metal counterparts [27, 48]. In addition to lower loss, Evlyukhin *et al.* demonstrated that high permittivity dielectrics silicon nanoparticles can support both electric and magnetic resonance modes [49], which widens the range of their applications. As a result of the use of dielectric materials, free-space communication based on antennas are now considered a prominent alternative to

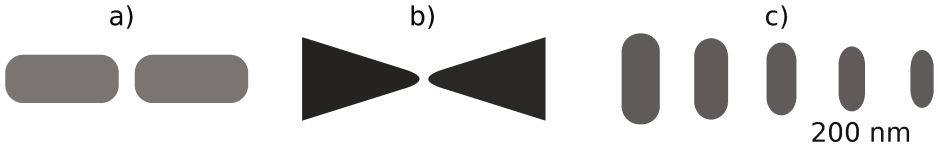

Figure 2.2: **Illustration of the main types of metallic antennas.** (a) Dipole antenna. (b) Bowtie antenna. (c) Yagi-Uda antenna.

fiber-to-chip interconnections even when broadband communication is required. Therefore, new broadband photonic antenna types have been designed, which can be directly fed using integrated waveguides. These antennas have the advantage of being manufactured using standard CMOS processing techniques. In addition, they can also be incorporated into the electronic circuit of a photonic interconnect platform. In this work we have special interest in optical antennas with this type of characteristics.

Other materials, such as carbon nanotubes, have also been used for the construction of antennas. Although a nanoantenna of carbon nanotubes usually has an extremely short size (considerably shorter than the wavelength) it presents a high resistance that causes high losses of conduction and, therefore, significantly decreases its efficiency [50].

2.2 Main applications of photonic antennas

The research field of the optical antennas is a relatively young field but it has experienced a vertiginous progress. In this section, we briefly review the progress of optical antennas, show how they are applied today, and how they could play a significant role in the future. We know that the literature of optical antennas counts with a significant number of works and, therefore, we just give a simplified idea of the applications that in our opinion are the most relevant, as well as some examples of their experimental demonstration. However, we will present in more detail the works related to chip-level coupling, which is one of the problems addressed in this thesis.

2.2.1 Microscopy and spectroscopy

The use of optical metallic nanoantennas leads almost naturally to imaging applications. In this context, an optical antenna are employed as a near-field optical probe that interacts locally with the surface of the sample to take an image [51, 52]. The image, therefore, will not be a direct representation of the properties of the sample, but of the antenna-sample [51]. However, it is possible to acquire in many cases a dominant behavior of one of the parts. An example of this approach is the use of nanoantennas made of a single or multiple gold spheres to be used as near-field probes in an optical fiber, which were used to obtain individual images of proteins with a spatial diffraction resolution of approximately 50 nm [52].

Spectroscopy is another area where nanoantenas are a key element. In this application antennas provide both an excitation and an improved emission of the sample under investigation. A metal nanoantenna that interacts with an incoming radiation generally leads to a high degree of field confinement, which have been used in several experiments as high-intensity excitation source, for example, in to induce fluorescence or Raman scattering [53, 54]. In this respect, the Raman-induced radiation has been

measured with metal bowtie antennas covered with a layer of adsorbing molecules [53]. These antennas also improve the photolithography process by reaching a resolution lower than 30 nm [54].

2.2.2 Photovoltaics

The main method employed in photovoltaics is the generation of free carriers in a semiconductor through light absorption [38]. The spatial separation of these photogenerated carriers creates a current in an external circuit [38, 55]. Then, to obtain the maximum efficiency in the process, the improvement of the absorption in the solar cells is crucial. In this context, an efficient coupling through optical antennas must be achieved, meaning a wide collection angle and a broad spectral response.

In 2007 Kirkengen *et al.* managed to improve the efficiency of solar cells made by using a thin film of silicon with silver nanoantennas [56]. Silicon, however, is an indirect bandgap material, making it a bad candidate in photovoltaic applications. More recently, in 2018, silver nanoantennas were used to enhance the efficiency of organic solar cell [57], improving such the fill factor, as well as the power conversion efficiency.

2.2.3 Sensors

Optical sensors based on metallic nanoantenas have been widely adopted in the chemical and biological areas due to the high precision and fast response. Generally the metallic sensor performs quantitative estimations through measurement of refractive index [55]. Because the local refractive index is related to the nanoantenna resonances, it is possible to attribute any index change directly to a change in the resonance frequency [58]. Since metal nanoantennas show resonances that strongly depend on dielectric properties, they are very good candidates for detecting very low concentrations. Moreover, because of their narrow resonances with high quality factors they present a high sensitivity. [55, 58].

In recent years, research has been intensified in the field of bio-sensors employing nanoantenas, applying them to the detection of DNA, bacteria, different types of cancer, viruses and bio-molecules, among others. For example, Mesch *et al.* demonstrated a gold nanoantenas coated with a thin layer of boronic acid functionalized hydrogel are used to measure extremely low concentrations of glucose [59].

2.2.4 LIDAR

Given the short wavelength of optical waves, LIDAR can offer a much higher range resolution than radio detection and ranging (RADAR) systems operating at microwave frequencies. Therefore, LIDAR has direct applications in last-generation technologies, such as autonomous vehicles and robotics [60]. For LIDAR systems to become a commercial

reality, however, they have to be low-cost, compact, and based in well-established fabrication platforms [61]. In this context, silicon photonics plays an important role in the implementation of optical phased arrays (OPA). OPAs were first demonstrated in silicon photonics in 2009 by the group of Professor Roel Baets of the University of Ghent [31]. Since then, there has been a great variety of innovations in the field of CMOS-compatible OPA. In particular, in [16], a large-scale passive $2d$ OPA with complex radiation patterns is demonstrated , whereas in [24], the monolithic integration of an OPA with active phase control is presented. The field of OPAs is now focusing on the system level and seems to be a viable solution for a built-in LIDAR system.

2.2.5 Coupling

Photonic integrated circuits (PICs) has attracted an increasing attention in the last years. The collaborative effort of many groups all over the world has resulted in improved fabrication quality and the development of novel devices. Even more, it is envisaged that given the broad bandwidth that PICs offer, they will resolve the challenge of chip-level high speed interconnections, achieving unprecedented bandwidth and power efficiency [62]. The transmission medium that naturally emerges as candidate to support these broadband inter-connections is fiber optic. However, given the dimension mismatch between the fundamental mode of standard telecommunications fibers and the fundamental mode of the silicon waveguides, the coupling between these two media posses a significant challenge.

Several antenna solutions have been proposed and implemented to solve this coupling problem. Fig. 2.3(a) and (b) presents the two main adopted approaches: in-plane coupling (edge) and out-of-plane coupling (surface), respectively. Fig. 2.3(c) shows an example where these two coupling approaches are implemented on the same chip, the in-plane coupling with a lensed fiber is located in the left part of the figure whereas the out-of plane coupling with a cleaved fiber is located in the right part of the image. In Fig. 2.3(d) a part of the experimental setup can be observed, where the positioning stages are used to fix the lensed fibers in order to locate them close enough to the edge of the chip. In addition, it is possible to see at the top of the image part of an objective lens that forms the optical system employed to obtain the image in Fig. 2.3(c). It is worth noting that this auxiliary optical system is of vital importance because, otherwise, alignment would be unattainable.

In-plane coupling

In-plane coupling, also known as edge coupling or end-fire coupling, is an approach that converts a waveguide mode with a cross section of several hundred nanometers to a micrometric mode of a fiber (or vice versa) within a plane parallel to the substrate.

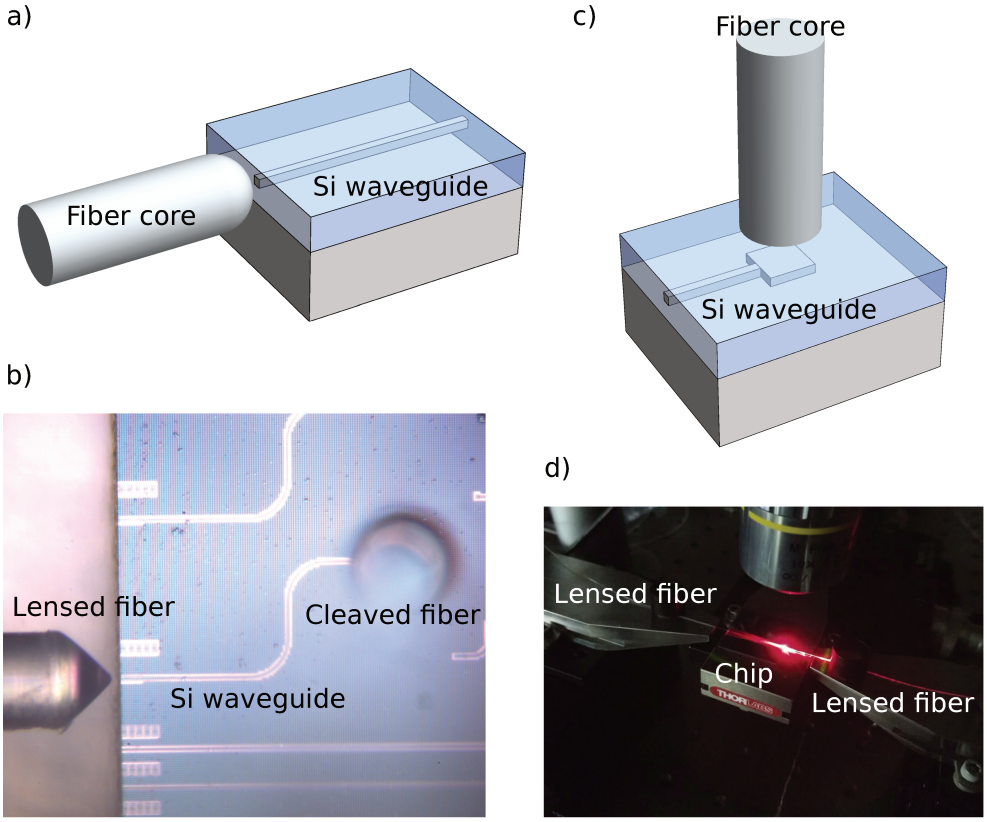

Figure 2.3: **Most commonly implemented fiber-to-chip coupling solutions.** (a) In-plane coupling (edge). (b) Out-of-plane coupling (surface). (c) Image of the two coupling approaches implemented on the same chip. (d) Part of the experimental setup where a two positioning stages is used to coupling light in the chip.

This modal conversion can be performed non-adiabatically (usually performed on the lensed fiber), adiabatically (generally done in an inverted taper on the chip), or also with a combination of them [26].

Initially, an apparently trivial solution was proposed. This solution consisted in the construction of a $3d$ taper on the chip to perform the coupling directly with a conventional cleaved fiber. With this method a peak coupling efficiency of about $-0.5\,\mathrm{dB}$ was achieved in $1550\,\mathrm{nm}$ [63]. In addition, several $3d$ tapers have been demonstrated in recent years with different materials and manufacturing techniques achieving a high efficiency (about $-1.9\,\mathrm{dB}$) [64–67]. Their construction was however considered unviable due to its difficulty for large-scale production because of their complex fabrication process and their multimode nature. Soon after, the famous inverted taper was developed as a high efficiency, and broad bandwidth singlemode solution. This inverted taper supported both polarizations and was easy to manufacture [68–74]. There were also solutions that merge $3d$ polymer tapers with inverted tapers built of silicon, as demonstrated in [75]. This combination shows relative ease of manufacturing and high performance.

Finally, a widely accepted solution in the literature and often employed in

laboratories, is the combination of a lensed fiber with an inverted taper, as shown in Fig. 2.3(c). This combination results in a coupling efficiency approximately −0.5 dB and bandwidth greater than 100 nm. To obtain such high performance, however, it is necessary that the lensed fiber to have a numerical aperture (NA) similar to that of the inverted taper. It is also necessary that the lens have an anti-reflective coating [76]. It is worth noting that due to the limitation that exists in the minimal focal diameter that can be achieved with the lensed fiber, it is not possible to achieve a high efficiency by directly coupling into the waveguide [77]. A great disadvantage of this combination is that we need to perform a post-processing the fabrication. The chip should be diced and polished in order to the end of the taper to coincide with the facet of the chip, as seen in Fig. 2.4(a). This post-processing increases the cost and the probability of damaging any device of the chip. In Fig. 2.4(b) we can observe an SEM image of an inverted taper without its post-processing. A breakthrough to avoid cutting and polishing of the chip was proposed in [73], where they perform an extra corrosion step. Unlike in the conventional corrosion process, which is performed on the entire sample, in this approach corrosion is done only at the edge of the chip. This corrosion at the chip edge forms a gap between the face of the chip and the inverted taper, as shown in Fig. 2.4(c). Unfortunately, this gap reduces the coupling efficiency approximately by 0.7 dB [73], although the large bandwidth is maintained.

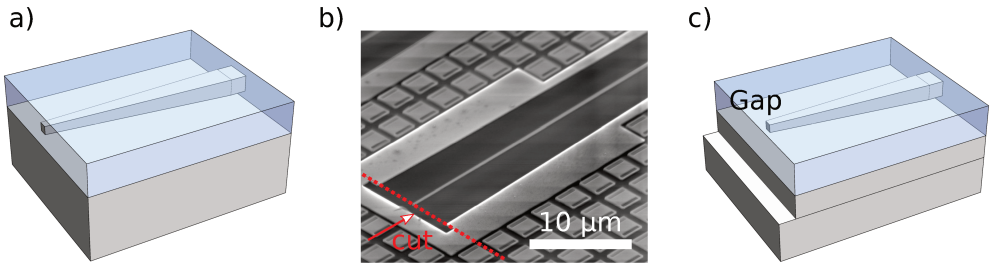

Figure 2.4: **Inverted taper (antennas) couplers.** (a) Illustration of an inverted taper with polished chip edge. (b) SEM image of an unpolished inverted taper. (c) Illustration of an inverted taper with ecthed chip edge.

Although the inverted taper is widely used, it still has a large size (its length exceeds hundreds of nanometers). In addition, the alignment stability poses a big challenge in absence of proper temperature and position controls. Chrostowski *et al.* reported that a loss of a 1 dB is introduced with a misalignment as small as 0.6 µm [76]. Several groups have proposed a mitigation to these problems by building a lens on the chip. Acoleyen and Baets proposed the use of two flat lenses on a conventional platform SOI [78]. Even if the authors do not present a measurement of coupling with a fiber, they report a significant reduction of the occupied area, since the lenses have a length ranging from 10 µm to 20 µm. On the other hand, Gabrielli *et al.* proposed a Luneburg lens which is placed between the

chip facet and the inverted taper [79]. This lens reduces the coupling loss by 6 dB when the misalignment is 4 µm, when compared with the directly coupling in an inverted taper.

In summary, in-plane couplers have a high coupling efficiency, a large bandwidth, and a low sensitivity to polarization. However, these are not compact since their length exceeds hundreds of nanometers. Concerning the manufacturing process, they are compatible with CMOS technology and easy to implement on SOI platform. Finally, we cannot forget that this type of couplers has little flexibility since it has to be located at the edge of the chip and suffers from small tolerance to misalignment, as well as requiring high precision cutting and polishing. In Appendix A a homemade recipe is detailed, which was employed to carry out the polishing process in a repetitive and successful way.

Out-of-plane coupling

The other main group of coupling devices is the out-of-plane (or surface) couplers. The main advantage of these couplers is that they do not require to be placed in any particular chip position, allowing easier testing with a conventional fiber at (usually) 10° incidence angle [26, 76]. Out-of-plane coupling does not require chip polishing at the facet and it is in general much less sensitive to misalignment, allowing to test the devices in automated setups before wafer dicing and post-processing to evaluate the fabrication quality at intermediate stages [26, 76]. Nonetheless, out-of-plane couplers face some challenges that in-plane couplers do not: mismatch of modal profiles and, a drastic change in the propagation direction of light [26]. In order to achieve maximum coupling efficiency, the waveguide and fiber modes should be matched in both real and k-spaces. In the real space, the matching between modal profiles can be measured by an overlap integral [80]. In the k-space, the propagation vectors must be similar both in magnitude and direction, which is equivalent to an impedance matching [80]. If the matching is not perfect, transmission efficiency reduces due to the increased scattering and back-reflected power. It is worth noting that mode coupling is bidirectional in the linear regime [76].

The most common structure used as a surface coupler is the diffraction grating. The grating coupler is designed such that the light scattered by the grating constructively interferes in a vertically radiated wave that is as much as possible matched with the fundamental mode of the fiber (in Appendix B a complete design guide can be found). Various grating designs have been implemented in recent years, mainly in silicon [81, 82], silicon nitride [83–85], and polymers [86, 87]. Typical silicon grating couplers have an efficiency between −3.5 dB to −5.5 dB and a 3 dB bandwidth around 60 nm in the near infrared [88, 89]. The narrow bandwidth is the main disadvantage of diffraction gratings when compared to in-plane couplers. Nevertheless, they present a strong advantage regarding their lateral misalignment tolerance, which is greater than 1 µm for 1 dB loss [81].

One of the main reasons for the low coupling efficiency in gratings couplers is the generation of a wave radiated towards the substrate, which similarity to the upward

radiated wave is also a solution to the Bragg equation. In order to improve coupling efficiency, the downward radiated wave must be suppressed or redirected. Redirection can be achieved by reflection in metallic mirrors [90] or distributed Bragg reflectors [91], which increases the coupling efficiency to −1.6 dB. The downside of these solutions is their complex fabrication process, making them not compatible with the CMOS technology. Alternatively, the grating profile can be optimized in order to suppress the wave directed to the substrate. An efficiency of −1.5 dB has been reported by allowing the grating teeth to rise above the waveguide core thickness [92, 93], which also increases the complexity of fabrication. Other methods to increase the efficiency include the use of apodized gratings [94–96] that achieve a coupling efficiency of about −1.2 dB, and sub-wavelength gratings [97] with a coupling efficiency of −3.8 dB.

The focused grating coupler has been widely accepted and used, since it is a compact design and presents a high performance. These couplers can be divided into two main approaches: the first one, is a shallow etched [Fig. 2.5(a)], and the second one, is fully etched, as shown in Fig. 2.5(b). The fully etched grating requires fewer steps in the manufacturing process, but in turn requires a more elaborate design, because it presents the same upward and downward power emission. A major contribution to the design of the fully etched gratings was reported in [98], where a sub-wavelength structure just like shown in Fig. 2.5(b) was demonstrated. This grating presents a kind of double periodicity that achieve a coupling efficiency of −4.1 dB, and a bandwidth of 3 dB of 50 nm. A highlight in this grating is its low reflection of only −16 dB, since in fully etched gratings the reflections are usually very high.

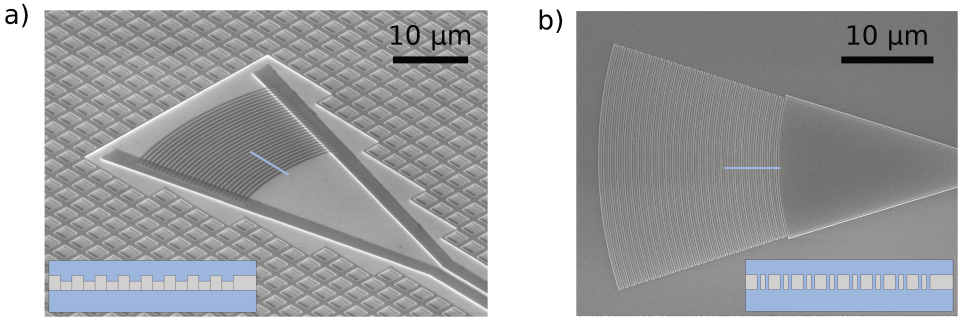

Figure 2.5: **SOI compact focusing grating (antennas) couplers.** (a) SEM image of a shallow-etched grating. (b) SEM image of a fully-etched grating.

When we design a grating coupler, either shallow or fully etched, we face three main types of losses. The losses in the substrate that occur when the downward radiated power is reflected and do not result in constructive interference with the radiated power upwards. Another power loss contribution is due to the mismatch between the radiated mode and the fundamental mode of the fiber. And finally, the loss due to reflections to the feeding waveguide. Table 2.1 shows an example of the performance of typical focused

gratings [76].

Table 2.1: Performance of a standard focused grating coupler [76].

	Shallow-etched	Fully-etched
Lost in the substrate	30 %	50 %
Mode mismatch	10 %	10 %
Back-reflections	0.1 %	30 %

As can be observed, the losses in the substrate are much greater for the fully-etched grating, which can be explained by the vertical symmetry. It is also possible to observe high reflection loss due because the refractive index changes drastically in the first grating period. In regards to the modal mismatch loss, similar values are obtained for the two approaches. With the emergence of the gratings built on an inverted taper, the length of the previous linear lattices was reduced to around 40 µm. In [99], a further size reduction is achieved, passing from a typical 40 µm grating coupler to approximately 25 µm. This is achieved with a short 15 µm taper defined by a quadratic sinusoidal function followed by a linear grating of length as short as 10 µm. In addition to reducing the size of the inverted grating they manage to maintain the efficiency and the 3 dB bandwidth at -5 dB and 58 nm, respectively.

Although the gratings are the most used and implemented couplers, there are also some alternative surface couplers. Among these we have an optical probe, which refers to a single mode fiber with a gold grid. As it approaches an integrated waveguide, the light can be coupled to the waveguide without integrated coupling structures. A coupling efficiency of -8.2 dB is achieved in a waveguide of 220 nm $\times$ 3 µm [100]. The fiber probe has the great advantage that they could couple light in any chip waveguide. An other couplers which also have this advantage are evanescent fiber couplers. These couplers are built by heating and pulling a fiber to reduce its core until evanescent tail of the mode propagates outside the fiber. This approach is used enough to directly test high quality cavities. For instance, Grillet *et al.* achieved a coupling efficiency of -0.1 dB in a highly nonlinear chalcogenide glass two dimensional photonic crystal waveguide [101].

In summary, although they have lower coupling efficiency and limited bandwidth, out-of-plane couplers have several advantages over in-plane couplers. The former have a high sensitivity to polarization because it is difficult to design a device that is capable to couple the both polarizations to the same waveguide efficiently. However, grating couplers are more compact than in-plane couplers. In terms of manufacturing, they are compatible with the process CMOS and easy to implement on SOI platform. Other points to highlight are their greater tolerance to the misalignment compared to in-plane couplers and their ability to allow tests at wafer scale. Finally, we emphasize that out-of-plane couplers have a high flexibility since they can be located anywhere on the chip.

2.2.6 Coupling challenges

In the previous subsection we presented an overview of the two main approaches for coupling an optical fiber to a photonic chip. In table 2.2 we show the advantages and disadvantages of these families of couplers when implemented in SOI platform and designed to operate at a central wavelength of 1.55 µm. These couplers are the inverted taper in combination with a fiber with a lens (in-plane coupling) and a focused grating (out-of-plane coupling).

Table 2.2: Most relevant properties of the SOI fiber-to-chip coupling techniques.

	In-plane coupling (lensed fiber + inverted taper)	Out-plane coupling Focused SOI grating
Coupling efficiency	>-1 dB	-5.5 dB to -3.5 dB
3 dB-bandwidth	broadband >100 nm	50 nm to 60 nm
Sensibility to polarization	weak	strong, can be solved with a 2d grating
Compactness	taper length: 80 µm - 120 µm	footprint area: >250 µm^2
Fabrication feasibility	easy but requires cutting and polishing	easy
Flexibility	only in the chip facet	suitable for multiple I/O in arbitrary position
Tolerance to 1 dB misalignement	± 0.3 µm	± 1 µm

As shown in the table 2.2, in-plane couplers have a high coupling efficiency and a large bandwidth compared to out-of-plane couplers. However, surface coupling has a significant advantage over edge coupling, that is, the potential of wafer scale testing. Therefore, grating couplers are the most promising solution to allow simple and efficient coupling. Despite the efficiency achievable by diffraction gratings and their intrinsic advantages, these devices also present important issues that hinder their widespread adoption as a solution for nanophotonic packaging. First, gratings are very sensitive to wavelength, which can be seen in their poor operation bandwidth. Second, they are also strongly polarization-dependent [26]. Finally, there is the fact that gratings have a footprint area of hundreds of micrometers square, which limits the density of data flow from and to the chip and significantly adds to the fabrication costs, as shown in [102],

where 90 % of the photonic chip area is consumed by the couplers alone. Additionally, smaller surface couplers would be the ideal candidates for coupling between multicore fibers and nanophotonic chips.

Multicore fibers are one of the most promising technologies for ultra-high data rate communication links at data center level. For instance, Sumitomo Electric Industries and the Japan's National Institute of Information and Communications Technology (NICT) achieved a new world record fiber-capacity of 2.15 Pb/s employing wavelength multiplexing in a fiber with 22 cores [103]. Nonetheless, the cores of most reported multicore fibers are usually closer than the minimal distance required between conventional grating couplers. Therefore, coupling antennas with reduced footprint would will be needed to couple each core to an individual single mode waveguide for further processing.

2.3 Optical phased array antennas

Although for many applications the size of the antenna does not represent a critical factor, in chips having multiple devices, the antenna footprint can limit the final density of the device and, thus, can significantly increase the manufacturing cost [102]. Another scenario where the size of the antenna is crucial is in OPA's. Since the performance and flexibility of antenna arrays improve as the number of elements increases, it is extremely important to use radiation elements with the smallest possible size, preferably smaller than half the operating wavelength. Then, a small-size dielectric antenna with broadside radiation pattern is quite desirable, as we discussed in the following sections.

2.3.1 Background

An array is defined as a set of equal antennas that radiate or receive radiation simultaneously. The radiation pattern of an array is the result of the interference of the radiated fields by each of the antennas, while in reception, the signal is a linear combination of the signals that each antenna captures. By reciprocity, if the weights and phase shifts of the linear combination in reception are equal to those in transmission, the radiation patterns in transmission and reception are equal [23]. Let's consider an optical array antenna of only two elements located along the x direction, at positions $x_1 = d/2$ and $x_2 = -d/2$ (similar to Young's interference experiment). According to the superposition principle of electromagnetic waves, the unitary scalar electric field in a far field point in the θ direction can be expressed as the superposition of the waves of the two optical antennas, as follows:

$$E(\theta) = e^{-ik_1 \cdot r_1} + e^{-ik_2 \cdot r_2}, \tag{2.3}$$

where k_1 and k_2 are the wave vectors from the antennas to the far field point, and r_1 and r_2

are the corresponding spatial vectors, as shown in Fig. 2.6. In the far field approximation, where $d \ll L$, the following assumption can be made: $k1 \approx k2 \approx k$, where k represents the wave vector from the origin up to the far field point. By phase variations we have:

$$\begin{aligned} r_1 &= r - (d/2)\sin\theta = r - x_1 \sin\theta, \\ r_2 &= r - (d/2)\sin\theta = r - x_2 \sin\theta. \end{aligned} \tag{2.4}$$

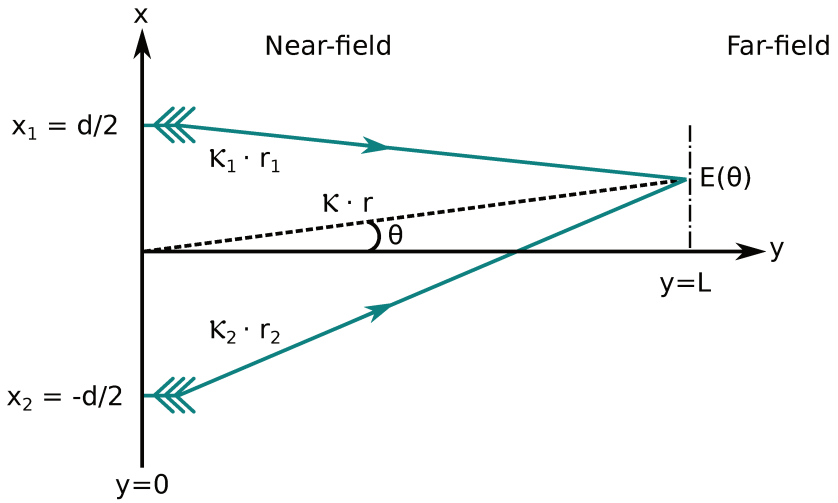

Figure 2.6: **Two-element optical phased array.** Young's interference experiment.

Therefore, substituting 2.4 in Eq. 2.3, we get:

$$\begin{aligned} E(\theta) &= e^{-ik\cdot(r - x_1 \sin\theta)} + e^{-ik\cdot(r - x_2 \sin\theta)} \\ &= e^{-ik\cdot r}(e^{ikx_1 \sin\theta} + e^{ikx_2 \sin\theta}). \end{aligned} \tag{2.5}$$

Neglecting the fast phase oscillation $e^{-ik\cdot r}$, we obtain:

$$E(\theta) = \sum_{n=1}^{2} e^{i2\pi x_n \sin\theta/\lambda}, \tag{2.6}$$

where λ is the optical wavelength. More generally, when the antenna array consists of N elements located periodically along the direction x, at positions $x_n (1 \leq n \leq N)$, and each antenna element radiates with an amplitude $|w_n|$ and phase φ_n, the Eq. 2.6 can be written as:

$$E(\theta) = \sum_{n=1}^{N} |w_n| e^{i\varphi_n} \cdot e^{i2\pi x_n \sin\theta/\lambda}, \tag{2.7}$$

where $|w_n|e^{i\phi_n}$ describes the radiated field of the nth antenna element. The Eq. 2.7 is a

general analytic description of an array of N elements. Extending the far field expression of the Eq. 2.7 to the $2d$ case, we get the following expression:

$$E(\theta,\phi) = \sum_{n=1}^{N} w_n \cdot e^{i2\pi/\lambda \sin\theta(x_n \cos\phi + y_n \sin\phi)}, \tag{2.8}$$

where (x_n, y_n) is the position of the antenna element in near field Cartesian coordinates, (θ, ϕ) is the far field position in spherical coordinates, w_n defines the amplitude and phase of emission of the antenna. When each element is considered as an ideal punctual source, the far field of the antenna array is conventionally known as the Array Factor, and is given by:

$$AF(\theta,\phi) = |AF|(\theta,\phi)e^{i\varphi(\theta,\phi)} = \sum_{n=1}^{N} w_n \cdot e^{i2\pi/\lambda \sin\theta(x_n \cos\phi + y_n \sin\phi)} = \mathcal{F}(w_n), \tag{2.9}$$

where $\mathcal{F}(w_n)$ denotes the relation between the discrete Fourier transform of the near field emission w_n and the far field pattern $AF(\theta, \phi)$.

Due to the implementation simplicity and package compactness, arrays are often designed with uniform element separation [104]. However, these arrays can have significant secondary lobes due to the large separation between the elements with respect to the operating wavelength. These secondary lobes are generally an undesired characteristic since they reduce the maximum power transmitted in the main lobe and can cause interference and safety failures. A common metric to evaluate this characteristic is the SLL, which is calculated as the ratio between the power of the strongest secondary lobe and the power of the main lobe. Generally in the literature, the SLL has been used to characterize the field radiation pattern of an array, or only of the array factor (AF). During this thesis work, we adopt the SLL of the AF because, in this way, the obtained results will be independent of the antenna element radiation pattern. In single-element antennas, as well as in array antennas where the separation of elements is less than half the operating wavelength (λ), the secondary lobe usually has a lower power than the main one. However, in arrays where the element separation exceeds $\lambda/2$, a periodic distribution of elements produces a AF that presents secondary lobes with the same power level as the main one, leading to a 0 dB SLL.

As an example, in Figs. 2.7(b) and (e) the AF is shown for a uniform array of 8×8 at a wavelength of 1550 nm, an element separation of $\lambda/2$ and 4λ [see Figs. 2.7(a) and (d)], respectively. In both Fig. 2.7(b) and (e) the AF profiles are taken at $\phi = 0°$. As can be seen in the AF profile for an array with element separation of $\lambda/2$, the secondary lobes have a level lower than the main lobe. Being that for this separation we have a SLL of -12.8 dB. On the other hand, when the same array has a separation of 4λ, it has secondary lobes with the same level of the main lobe and, consequently, we have a SLL of 0 dB. It should be noted that this separation between elements is critical, especially in the

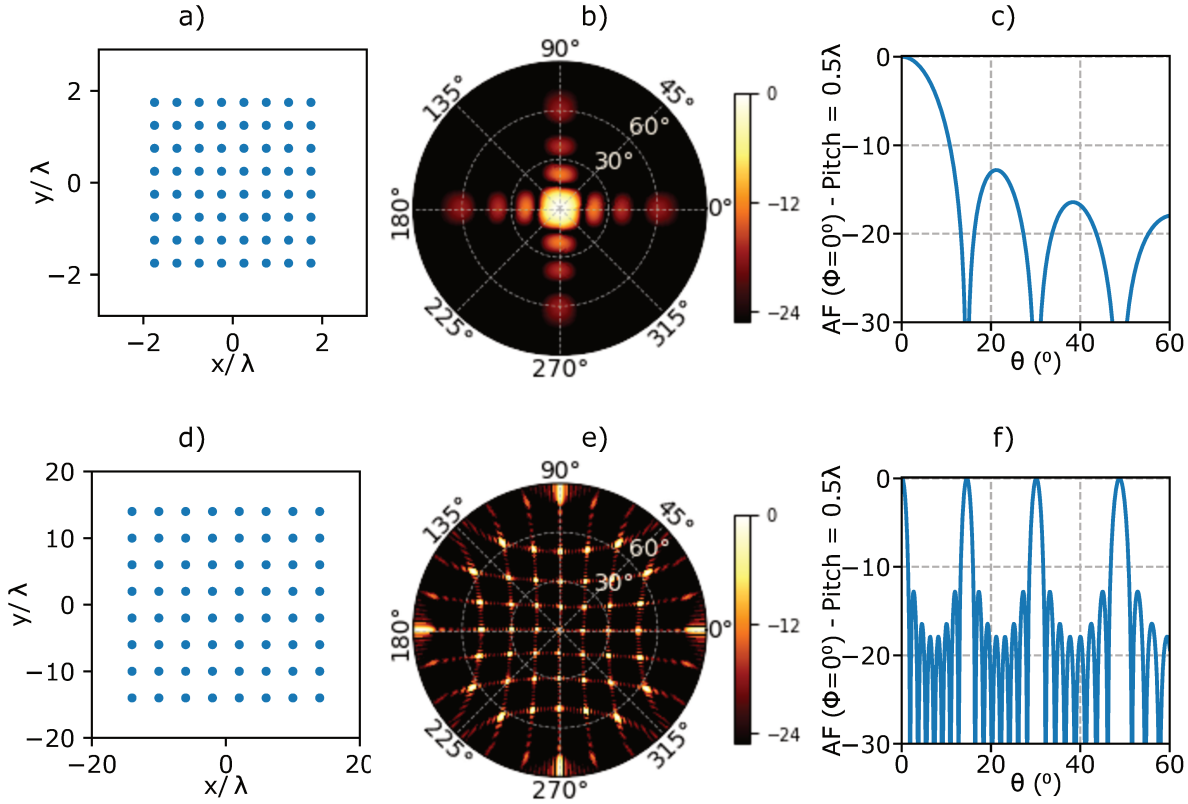

Figure 2.7: **Array factor diagram of periodic distributions for different antenna pitch values.** (a) and (d) Arrays composed of 64-elements arranged in a square grid with separation of $\lambda/2$ and 4λ, respectively. (b) and (e) Full array factor diagram for a 64-elements arranged in a square grid with pitch of $\lambda/2$ and 4λ, respectively. (c) and (f) Detailed view of the normalized array factor near the main lobe for $\phi = 0$.

infrared and visible wavelengths, because the limited footprint of each antenna element, as well as the separation at various wavelengths.

2.3.2 Literature Review

Optical nanoantenas smaller than the operation wavelength have been extensively studied as we saw previously, however, as we mentioned, these are built with metals to take advantage of the strong metal-light interaction. Although they are compact in size, they are not compatible with the standard CMOS manufacturing process and, therefore, they present serious limitations for integrating large-scale phase arrays. One candidate solution is the use of grating antennas, which has been proposed by several groups [81, 95]. However, even if suitable for optical coupling, the large footprint of gratings renders them unfit for OPAs. Despite this, these gratings were used in [25] to demonstrate an integrated projection system using an OPA of 4×4 elements. A remarkable breakthrough in footprint reduction was made in [16], where a grating antenna with a size as small as 3 µm × 2.8 µm was demonstrated, allowing the implementation of a 64 × 64 OPA. However, these gratings

are designed to present the direction of the maximum radiation in an angle greater than 20°. Non-vertical radiation increases the packaging complexity and cost dramatically in applications such as fiber-to chip coupling [105]. Unfortunately, if the grating is designed to radiate vertically, the antenna efficiency drops sensibly since a great amount of intensity is reflected back toward the feeding waveguide (see appendix B).

In 2015, Abediasl *et al.* demonstrated the first monolithic transceiver using an OPA with independent amplitude and phase control [24]. Here the phase and amplitude of each antenna was controlled using an electronic circuit integrated with the photonic components in the same substrate. They built a uniform array of 8×8 grating antennas, each element was made of polysilicon and crystalline silicon with 3.55 µm×1 µm footprint area, and a direction of maximum radiation close to 20°. This OPA was used to couple light into a fiber, obtaining a total fiber-to-fiber loss of 23.6 dB. Such a high loss can be attributed to grating lobes caused by the large distance (5 µm) between their radiation elements. Another important work on sparse 2*d* OPA was presented by Fatemi *et al.* in [106], where an array of 128 grating antennas with an element spacing of 5.6 µm was demonstrated. They achieved a SLL of −12 dB in a 16° steering range. Nevertheless, as in aforementioned work, the fabricated OPA does not present the direction of maximum radiation direction vertically oriented, but if close to 16°.

Due to the size limitation of the antenna and the complex feeding network composed by conventional silicon waveguides, most of the OPA to date were built in one dimension (1*d*). Chung *et al.* implemented a monolithic OPA of 1024 elements operating at 1550 nm, with fully array electronics control, and fabricated on commercial 180 nm SOI CMOS technology [107]. The antenna elements were spaced by 2 µm, which allowed them to detect an object smaller than 5 cm at a distance of 100 m. For this purpose they used a polysilicon grating antenna with a area of 3.55 µm×1 µm, and with the maximum radiation oriented toward 20°. In [108], Hutchison *et al.* demonstrated a CMOS non-uniform large-scale arrays in which that the main radiation lobe can be steered by 80°. They also achieved the smallest divergence to date of the beam, i.e. ϕ of 0.11°. To achieve such a small beam divergence, they employed waveguide-grating antenna elements with large size (some millimeters). This year, Miller *et al.* demonstrated the highest OPA 1*d* (512 elements) with individual phase control for each element and very low power consumption (<1.8 W) [17]. They showed 2*d* beam steering operation over 70×14° while feeding with an integrated InP/Si laser. Since the arrange is 1*d*, the steering in the second dimension is achieved via lateral gratings antennas of 1 mm length, through wavelength tuning of the integrated laser. This year it was also demonstrated an electrically-steered OPA of 15° with a monolithically integrated rare-earth doped laser source emitting at 1599 nm [109]. In order to achieve this, they employed 49 antennas using 500 µm-long gratings separated by 2 µm.

The majority of OPAs built on SOI platform, in addition to suffering from the

spacing limitations between elements due to the antennas size, they present a limitation due to evanescent coupling between the feeding waveguides. Phare *et al.* demonstrated the first $1d$ OPA of 64 elements spaced by less than half wavelength ($\lambda/2$) [110]. For this strip silicon waveguides were employed as antenna elements. These waveguides were designed to have different phase velocity to avoid evanescent coupling between them, which was achieved using different waveguide widths. Because of the narrow element separation, the radiation pattern has a SLL as low as $-11.4\,\mathrm{dB}$ in a field of view of 180°.

2.3.3 Challenges

As we have seen, there are serious limitations when fabricating $2d$ arrays due to the antenna element size, which is generally of the order of two wavelengths. The size of antenna element is even larger in $1d$ arrays where the antenna elements are grating built on waveguides (they can have sizes up to several millimeters). Another limitation that is inherent to the feeding network is the separation between elements, which at least has to be greater than $1\,\mu\mathrm{m}$ to avoid evanescent coupling. The phase control network is an additional constrain in arrays where the active control of the elements is required, since the size of the active photonic elements can further limit the separation between the elements. As we already know, these large antenna sizes and inter-element separation leads to unwanted grating lobes, resulting in high SLL values.

Almost all the developed OPAs using a feeding network based on cascaded $3\,\mathrm{dB}$ splitters that divide to power equally, thus feeding each antenna with the same amplitude. This splitting architecture occupies an even larger area that the antenna array, since a significant number of splitters are required for large-scale arrays, which compromises the integration density on the chip. In addition, since these dividers are cascaded, small deviations in design and fabrication can cause significant degradation on the array performance. For these reasons, the OPA reported up to date are limited to $1d$ configuration, or $2d$ arrays with relatively low number of elements. The feeding challenge become harder when the OPA has an aperiodic element distribution.

Although OPAs manufactured using commercial CMOS manufacturing processes have evolved rapidly in recent years, they still pose a fundamental challenge that impoverishes their performance. This is the fact that there is not yet a photonic broadband antenna with efficient broadside radiation that can be fed directly by a conventional waveguide, while keeping their footprint below a wavelength. Consequently, the implementation of a grating lobes free large-scale $2d$ array is something practically unfeasible.

Chapter 3

Developed fabrication process and characterization setups

As indicated in the previous chapter, most of the antennas for last-generation commercial applications are CMOS compatible. In order to analyze CMOS compatible antennas, we had to develop both the fabrication process and the characterization setup in our laboratories. In this chapter, we describe the development of these process in detail, additionally, the Appendix C precise but simple recipes for each stage of the process can be found. We begin by describing the developed fabrication process, focusing on the main challenges to achieve reliable and repeatable devices. An important point to mention is that external manufacturing was also used to obtain devices thought this work. This fabrication, however, generally takes longer than a year, and is subject to strict design rules that significantly limit the structures that can be built. On the other hand, using in-house fabrication, the required time can be drastically reduced, in addition to offer more flexibility in the designs. It is also important to mention that the developed fabrication processes were implemented at CCS-Nano facilities and at LAMULT laboratory of the "Gleb Wataghin" Physics Institute. The fabrication and design of the device were carried out in parallel, since it was necessary to gain experience in the process to know the limitations of our design. It takes two and a half years in which there were several surprises in the clean room, in the last year we spent more than 200 hours between electronic lithography, electron microscopy and plasma corrosion among others. Fortunately, the tax paid for using the clean room of CCS-Nano of 5000 R a year is very low compared to the clean rooms of countries like United States. The optical characterization of the fabricated samples, including coupling and near-field and far-field measurements, was performed at the LCO using experimental setups projected and improved during the time of the doctorate.

3.1 In-house fabrication process of photonic antennas

The wafers used to fabricate our devices were acquired at SOITEC [111]. Each wafer has a 6 in diameter and a approximate thickness of 700 µm, where the silicon layer has a thickness of 250 nm, and the BOX layer has a thickness of 3 µm [see Fig. 3.1(a)].

The first step in our fabrication process was diced of 1.3 cm × 1.3 cm the wafer of 6 in. For this, we apply the photoresist AZ-4620 on the wafer and spin off at 3000 rpm during 45 s to get a thickness of 2.2 µm. Next, we do a long prebake of 180 s on the hotplate at 120 °C, this with the aim of protecting the silicon layer during the dicing stage. Then, we perform the dicing in the Centro de Pesquisas Renato Archer (CTI) facilities, which is carried out in the Disco DAD-321 saw. To achieve a cut without losing pieces, it is necessary to mount the wafer in an UV adhesive film on a metal frame, as seen in Fig. 3.1(a). Then, the frame is placed with the wafer stuck on a plate where a diamond saw rotating between 15 000 rpm and 30 000 rpm cuts the wafer following a predefined matrix. While the saw cuts the wafer, deionized (DI) water is added as a cooling agent along the wafer. This water helps in controlling the temperature, and also, prevents the dust and the blade saw particles from contaminating the wafer. The final result of the cut can be seen in Fig. 3.1(b). Here we can see that even with the use of the UV adhesive film some pieces of the wafer are lost.

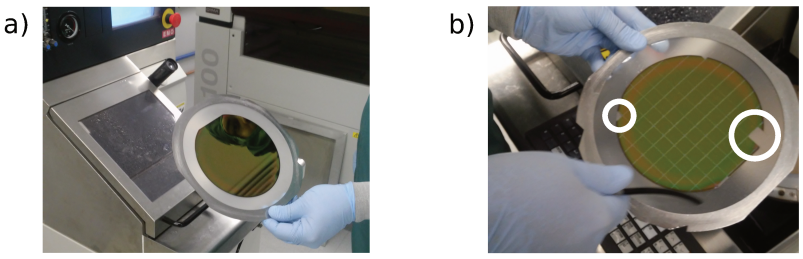

Figure 3.1: **SOI wafer of 6 in used in the fabrication process.** (a) Wafer on the UV adhesive film ready for dicing. (b) Wafer after the dicing process. Within the white circles you can see the missing pieces.

After the dicing process, each piece of chip goes through the steps outlined in Fig. 3.2(b-d). First, each piece is covered with an electro-resist (e-resist) that is modeled to form the desired device design through an electronic lithography process. Then, these patterns are transferred to the upper silicon layer by plasma etching. Finally, we performed a plasma-assisted deposition of silica to protect our devices from dust and the hostile environment of the laboratory. In the rest of this section, we describe some details of our fabrication process, as well as the consolidated recipes of each stage of the process.

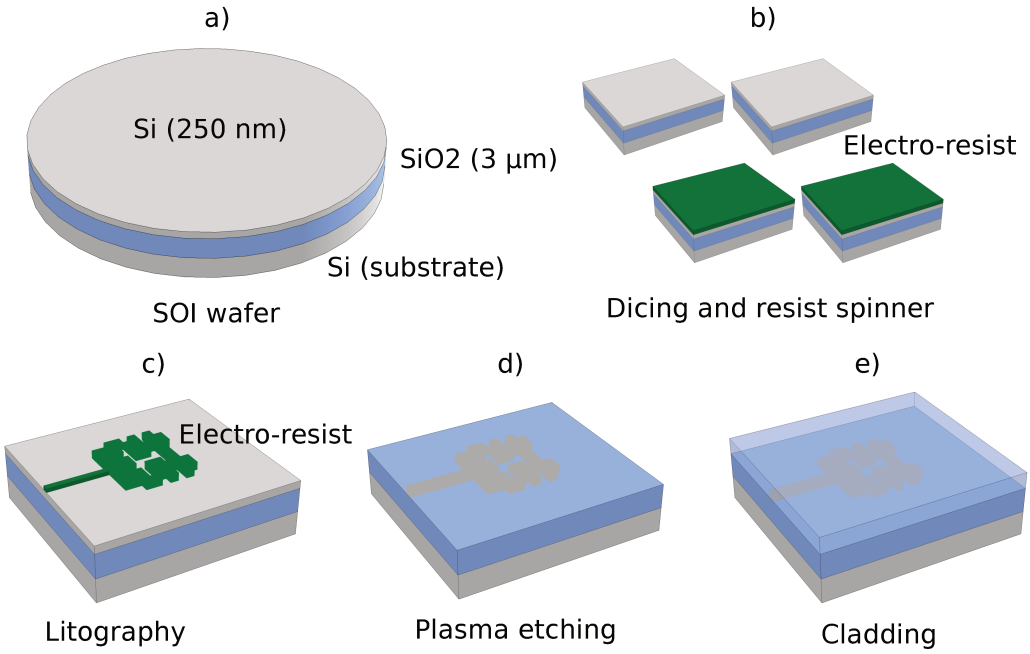

Figure 3.2: **Summary of the fabrication process of the photonic antennas.** (a) The antennas are fabricated on commercially available 6 in SOI wafers, with a silicon design layer of 250 nm and a BOX layer of silicon dioxide of 3 µm. (b) Chips diced of 1.3 cm×1.3 cm coated with a e-resist for electron beam irradiation. (c) Layout mask transferred to the e-resist that remains in the upper part of silicon. (d) The e-resist pattern is transferred to the silicon layer by plasma chemical etching. (e) Finally, a coating of silicon dioxide is deposited to protect the devices from any damage.

3.1.1 Surface preparation and spinner

Before the lithography process the surface preparation of the sample is necessary, since the presence of organic residues or impurities prevents the e-resist from adhering to the silicon layer. The cleanliness that we elaborate in our samples is the standard RCA cleaning of CCS-Nano, which consists of the following steps:

1. Submerge the sample in the exothermic solution $H_2SO_4 + H_2O_2$, 4:1 (usually known as "piranha") for 10 min, which removes most of the organic residues from the sample surface.

2. Submerge the sample in cold solution $HF + H_2O$, 1:10 during 30 s. The aim of this step is to remove native silicon oxide.

3. Submerge the sample in a solution of $NH_4OH + H_2O_2 + H_2O$, 1:1:5 at 80 °C and keep the sample for 10 min. This removes the remaining organic lipids and some metallic impurities.

4. Finally, immerse the sample in the solution $HCl + H_2O_2 + H_2O$, 1:1:5 at a temperature of 80 °C for 10 min. This with the objective of removing some metals that were not

removed in the previous step.

Since we will use the e-resist Ma-N 2403 ("MAN") and we need to guarantee a good adherence, some additional steps are required. This e-resist was chosen because it presents excellent thermal stability, high resistance to wet and dry etching, and is easy to remove. Before using it in the sample, however, we need to perform the following three steps to have repeatability:

1. Perform a plasma barrel of oxygen at the LPD-IFGW. For this we set the reactor parameters at: 100 mTorr of pressure, 40 W of RF power, 50 sccm of O_2, for 10 min. Without this step even using adhesion promoters the MAN does not fix correctly to the surface.

2. Dehydrate the sample, for which the sample is baked to 120 °C for 13 min on a hotplate.

3. Cover the surface with the hexamethyldisilazane (HDMS) adhesion promoter to obtain repeatable results. For this, the solution of HDMS is applied to the sample and spin at 3000 rpm for 30 s. Then the sample is left to settle for 90 s, after which the sample is ready for the e-resist application.

Once the sample is ready for the application of the e-resist, we apply few drops of MAN on the chip before spinning it at 3000 rpm during 30 s. With this rotation speed and this time an average film thickness of 327 nm is obtained, as shown in Fig. 3.3. Then, to remove the solvent from the MAN, a soft baking process is performed at 90 °C during 90 s on a hotplate. The sample has now a MAN film and is ready to be used in the electron beam lithography. Since MAN is a negative-tone e-resist, the areas exposed by the electron beam become less soluble than the unexposed ones, that is, the pattern written by the electron beam corresponds to that of the desired device.

3.1.2 Lithography

For manufacturing optical devices, there are mainly two types of lithography: photolithography and electron beam lithography (e-beam lithography). In both types of lithography it is required that the wafer to be covered with a sensitive film (resist), which will be sensitized to transfer the desired layout. In photolithography, a mask usually made of chromium on a quartz plate is used, in which the desired pattern is projected. Through this mask, the wafer is exposed with an intense ultraviolet light. On the other hand, for electron beam lithography, there is no need to build a separate mask. In this approach, a collimated electron beam is used to directly transfer the desired layout to the resist in the wafer.

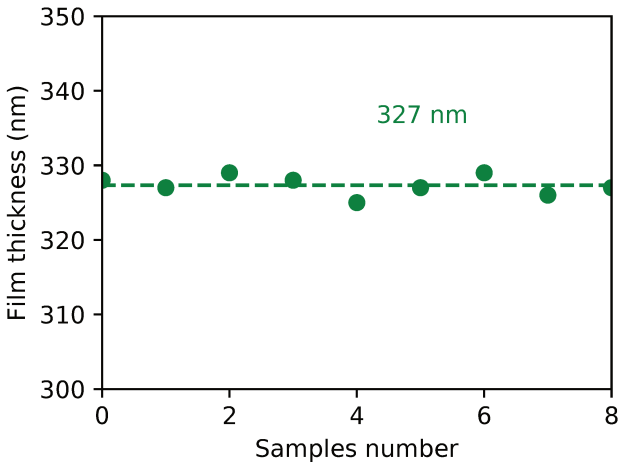

Figure 3.3: **Thickness of the MAN film obtained by AFM in 9 different samples.** For the film deposition the same recipe was used, however, as the process is implemented in groups of 3 samples, some environmental conditions (temperature and humidity) change from sample to sample.

Photolithography presents the limitation of the minimum experimental resolution of 500 nm due to the wavelength of the exposure light, in addition, to have limited flexibility derived from the additional mask required. On the other hand, e-beam lithography allows greater flexibility in the design of the layout because this is done by means of computer-aided design (CAD), since it is direct writing. In addition, it offers a higher resolution, so we managed to make minor details in the design, which would not be possible with photolithography. The resolution depends on the specific resist used to transfer the pattern, but e-beam lithography details with sizes smaller than 50 nm can be achieved without major challenges. As for writing times, e-beam lithography can be longer than in photolithography, although these depend on the area, the layout, the exposure dose and the employed resist. It is important to mention, however, a prolonged writing time is detrimental because it can lead to changes in the equipment parameters during the process, affecting the quality of the final design, as well as increasing its cost. To fulfill the objectives of this work, we decided to use e-beam lithography mainly because of the antennas required resolution and to take advantage of direct writing.

To design the lithography pattern of our structures, we use the open source python module gdspy [112] to write the layout in the format GDSII. This is a standard in the microelectronics industry and is a format recognized by the employed e-beam lithography equipment (Raith E-line Plus 150). This equipment consists mainly of an electronic scanning microscope integrated with hardware to make electron beam exposures. This tool has a travel range of 100 mm, a column voltage that varies from 300 V to 30 kV and a laser stage with a move accuracy of 2 nm. The system has seven apertures on the system: 7, 10, 15, 20, 30, 60, and 120 µm. Wider apertures results in a greater current, and therefore to a worse depth of focus, so we decided to work with the opening of 7 µm.

The depth of focus can be understood as the range of focus errors that a process can tolerate and still give acceptable lithographic results. Another critical parameter for a successful process is the electron beam exposure, which is normally specified in units of a surface density. In order to achieve a good balance between the waveguide roughness and the fidelity to our optimized devices several tests were carried out, giving as a result an optimal dose of 125 µC/cm^2. It is worth noting that after determining our fixed dose, we use the equipment software to perform the dose correction with predefined parameters for this particular resist and wafer to avoid the proximity effect as much as possible.

Another parameter that plays an important role in the final performance of the device is the writing field, since this field represents the limits and the area that the tool can write before moving the location of the beam. To ensure the highest possible quality in our writing, we use a writing field of 100 µm × 100 µm, making sure that the antenna is in a single field. Therefore, stitching errors can only be present in the waveguides. The stitching errors usually occur at the limits of the writing field when, due to the prolonged exposure time, the beam deflection causes a misalignment of the pattern in these areas.

As we mentioned earlier, the writing time of electron beam lithography is high, mainly due to the fact the limited writing speed. In practice, our equipment supports a writing speed of 10 m/s. According to experimental tests carried out by other groups that have been using the equipment for a long time, above this limit, some exposed regions may receive a lower dose than expected or, even, not receive any dose. The writing speed can be modeled as follows:

$$beam\,speed = \frac{step\,size}{dwell\,time}, \tag{3.1}$$

where, the minimum step size is determined by the ratio between the size of the writing field (100 µm) and the addressable resolution of the digital to analog converter (DAC) (16 bits), resulting a step size of 1.53 nm. Therefore, for our work we will use a step size of 2 nm, because it is the limit of the equipment. On the other hand, the dwell time represent the time that the electron beam must remain stable over a certain point, so that each region receives the desired dose. The dwell time, hence, can be defined as:

$$dwell\,time = \frac{area\,dose \times line\,spacing \times step\,size}{beam\,current}. \tag{3.2}$$

For an aperture of 7 µm and an acceleration voltage of 20 KeV, we have a beam current of about 10 pA. On the other hand, both the line spacing and the line size are set to 2 nm, resulting in a dwell time of approximately 50 ns. Therefore, our write speed is approximately 4 m/s, which guarantees a good writing quality.

In regards to the approach adopted for writing the layout, our tool allows us two ways of modeling areas, that is area mode and curved elements. Since in our layout there is a minimum amount of curved elements, we choose the area mode. In this mode,

we have the possibility of writing in two ways: the first form is the line mode, where the whole pattern is written as a series of lines, all starting from the same side. This method requires that the beam to be blanked at the end of each line, after which it is moved to the beginning of the next line. It is important that this approach requires an additional time to stabilize before resuming writing. The second form is the meander mode in which it is not necessary for the beam to be bleached when it reaches the end of each line. Instead, the beam will move directly to the subsequent line and continue writing in the opposite direction. This method allows to save both time, either the stability time between lines and the dwelling time. However, although the meander mode reduces the writing time by approximately 150 %, the writing accuracy generally decreases. Since the MAN is of negative tone, the writing time of our mask is not very high and, therefore, we opted for the line mode since because of its superior writing precision.

The lithography process is finished by developing the resist, so only the areas of MAN that were irradiated by the electron beam remain. The solution that was used to accomplish the development was AZ-300 MIF (tetramethyl ammonium hydroxide at a concentration of 2.5 %). The sample is submerged in this the solution for 95 s, after, it is immersed in DI water for 3.5 min. Finally, a soft drying with nitrogen flow is carried out. The MAN mask obtained after the lithography process can be seen in Fig. 3.4(b), whereas its respective layout is shown in Fig. 3.4(a).

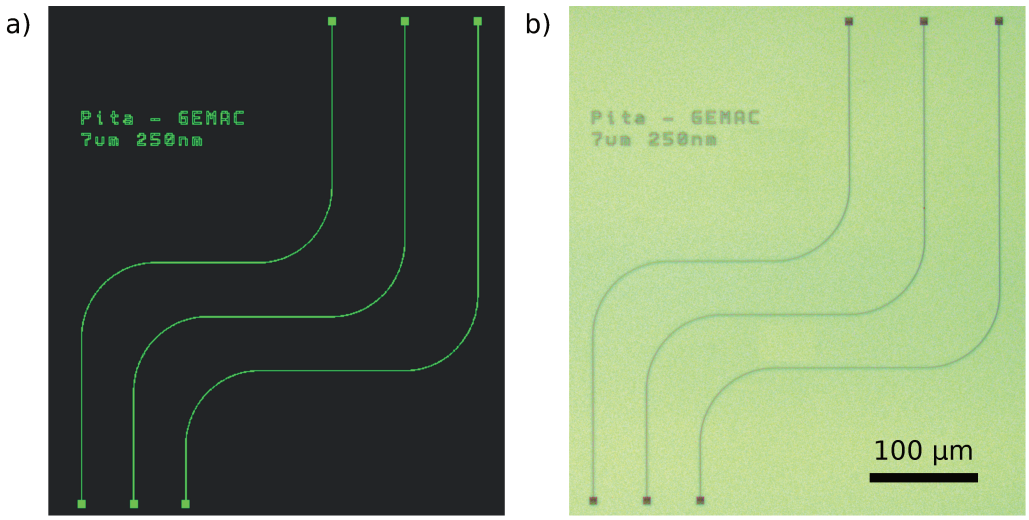

Figure 3.4: **Pattern used in the fabrication process consisting of 6 optimized antennas.** Each pair of antennas is connected by a waveguide, being that the three waveguides are of different lengths. (a) Layout for e-beam lithography projected in gdspy in the format GDSII. (b) Result MAN mask after the lithography process.

3.1.3 Silicon etching

To transfer the pattern of MAN obtained from the lithography process to the silicon layer, plasma etching was used. According to the English dictionary of Oxford, a plasma is defined as: "An ionized gas consisting of positive ions and free electrons in proportions resulting in more or less no overall electric charge, typically at low pressures (as in the upper atmosphere and in fluorescent lamps) or at very high temperatures (as in stars and nuclear fusion reactors)". Plasmas can be classified into two main groups: fully ionized plasmas, where ions and electrons are close to thermal equilibrium (hot plasmas), and weakly ionized plasmas that operate in non-equilibrium (cold plasmas). The latter is preferred in the semiconductor industry [113].

Plasma etching is composed of two steps: first, the generation of ions and its control to direct it towards the target sample. Second, the physical corrosion, that is, how ions can mechanically or chemically eliminate the atoms of the substrate. In the semiconductor industry there are several modes of excitation of plasma, being capacitively coupled plasma (CCP) and inductively coupled plasma (ICP) the most used. CCP uses two electrodes to provide power by applying a voltage (commonly RF) between the anode and cathode plates. In ICP sources, in contrast, energy is supplied by inductively produced electric currents (time-varying magnetic fields), generally generated through a large copper coil with 4 or 5 spirals that surrounds the plasma chamber.

We chose to use the technique reactive ion etch (RIE), since this dry anisotropic etching technique allows us to define our devices very well. Here, we will not make a detailed description of the physics of ICP-RIE with respect to plasma characteristics. Instead, based on the extensive literature [114–116], we will explore how some etching characteristics and control parameters of the Oxford Plasma-100 affect the final design. This equipment has a CCP energy source (known as forward power), which has as its main role the conduction of the ions towards the surface of the substrate, and an additional ICP source. This dual plasma feed offers greater flexibility to alter plasma characteristics, such as ion density and polarization voltage [113]. The following general guidelines taken from [115], served as the starting point for our etching recipe:

- The increase in forward power generally increases the bias voltage. This further increases the milling aspect of both the substrate and the mask and, therefore, the substrate cannot be etched for a long time.

- The increase in the power of ICP directly increases the vertical magnetic field through the plasma. Since the ion density in the plasma increases, more reactive ions will be sent to the substrate, which will increase the chemical aspect of the etching.

- The decrease in pressure allows the plasma to spread, reducing the dark space which in turn increases the electric field that drives the ions. Therefore, a lower pressure

can reduce the undercut in the side walls.

Although it is possible to control the etching profile through the source power and the pressure, the main etching control mechanism is the chemistry engineering of the used gas. There are multiple passivated etching chemistries for silicon. In this work, SF_6 was used as the etching gas, and octafluorocyclobutane (C_4F_8) was used as a passivation gas. This passivated etching is called pseudo-Bosch, and is a mixed mode passivation method, because the passivation and etching gasses are different [117]. Before placing the sample in the chamber for etching, two plasma processes are always performed to prepare the camera. The first step is to realize an oxygen plasma, with 15 mTorr of plasma pressure, 15 W of forward power, 1200 W of ICP power, and a 40 sccm of O_2 for 10 min to clean the carbon residues within the chamber. The second step is a conditioning that consists in making the plasma of the etching with the same parameters of the recipe that will be used in the sample. This is done with the camera empty for 5 minutes. The objective of this process is to achieve the greatest possible stability during the etching process, since this allows us to anticipate most of the transitory effects caused by the reactions between the plasma and the wall of the chamber. Finally, the parameters used for our plasma etching were: a SF_6 flow of 15 sccm, a C_4F_8 flow of 26 sccm, a pressure of 15 mTorr, a forward power of 15 W, and an ICP power of 15 W. An important point to note is that due to the dependence of the angle of the profile on the flow relation of SF_6 and the total gas flow ($r_{sf_6} = \frac{SF_6}{SF_6+C_4F_8}$), the latter was set to 36.6 % to get a profile of 90° [116].

To find the MAN selectivity and the silicon corrosion rate, several samples were processed using previous process, after which the thickness of the the MAN and silicon films were mapped using atomic force microscopy (AFM). For MAN, we obtained a corrosion rate of 47 nm/min, whereas for silicon a corrosion rate of 112 nm/min (see Fig. 3.5), which results in a selectivity of 1:2.4. This means that for our samples that have a silicon layer of 250 nm the corrosion time is approximately 2.2 min.

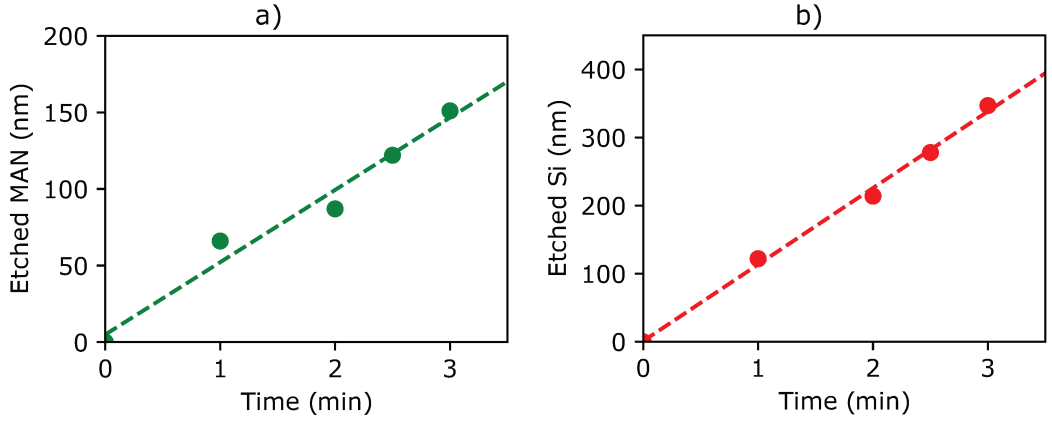

Figure 3.5: **Etched thickness of the films versus the time to exposure to plasma pseudo-bosh etching.** (a) MAN e-resit film. (b) Silicon film.

3.2 Characterization of photonic antennas

In this section we present the setups employed for characterization of the fabricated photonic antennas. First, we will describe the setup to characterize the antenna designed for fiber-to-chip coupling and, then, we will describe the setups used for near-field and far-field radiation characterization.

3.2.1 Coupling characterization

In Fig. 3.6(a), we can see the system used for coupling characterization, which consists of a motorized microscope, two piezoelectric stages, and an optical system to couple light into the chip. The optical systems, chip and piezoelectric stages are located inside an acrylic box, to protect the setup from abrupt temperature variations and dirt. The microscope is used to perform the coarse alignment of the fibers, thus preventing the fibers to touch the chip, which could damage some device. The controls of both the microscope motors and piezoelectric stages are left outside the box. This scheme allows a fine alignment without requiring to open the protecting box.

In Fig. 3.6(b), we show the setup to measure the efficiency of surface coupling efficiency of two antennas connected by a waveguide. To measure the coupling efficiency in a wavelength range between 1470 nm and 1570 nm, we use a superluminescent diode (SLED). The output of the SLED is first passed through a LP, after which a PC is used to optimize the polarization at the output of the cleaved standard fiber in order to match the quasi- transverse electric (TE) mode of the input antenna. The light radiated by the output antenna is captured by a second cleaved fiber which is directly monitored on an optical spectrum analyzer (OSA), which has been configured to compensate for the base line of the SLED. In Fig. 3.6(c) we can see an image of the chip. It can be noted that the fibers are in a vertical position, as we saw earlier, because our antennas has its maximum coupling efficiency at 0°. On the other hand, in Fig. 3.6(d), a variation of the setup is observed in which the input coupling is done via an inverted taper and a LF.

3.2.2 Near-field and far-field characterization

Fig. 3.7(a) shows an image of the configuration used to characterize the fabricated array antennas alongside with the block diagrams for the near-field [Fig. 3.7(b)] and far-field measurements [Fig. 3.7(c)]. Both measurements are proportional to the optical intensity but, while the first is related to the intensity of the irradiated field on the surface of the elements (radiation sources), the latter corresponds to the field radiated in the Fraunhofer region. The term "near-field" is used here as is conventional in this area, since the measurements reveal only the image the radiating elements, the reactive components of the near-field cannot be captured in this configuration. A tunable laser

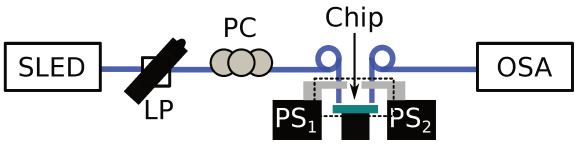
SLED
LP
PC
Chip
OSA
PS1
PS2

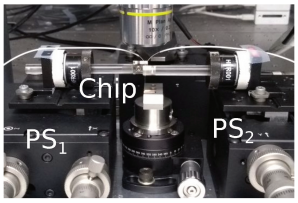
Chip
PS1
PS2

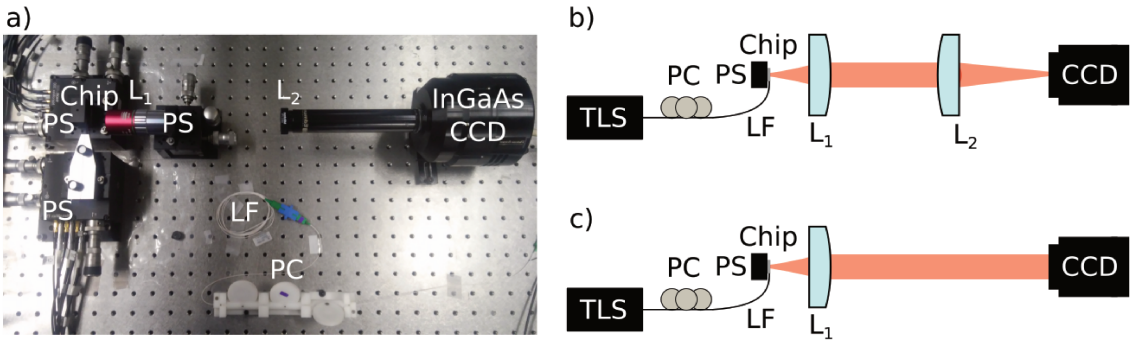

Figure 3.7: **Setup for near-field and far-field measurement of fabricated SOI-based antennas.** (a) Photograph of the setup. (b) Block diagram for near-field measurement. (c) Block diagram for far-field measurement. PC: Polarization controller, LF: lensed fiber, PS: piezo stage, L_1: objective lens, and L_2: infra-red lens, and CCD: InGaAs camera. "Reprinted from [11]."

Chapter 4

Optical single element antennas

An exigent antenna design combining improved radiation features and small footprint can be addressed through computer-aided optimization that results in non-intuitive devices with superior performance. In the last few years, the number of device designs using optimization has experienced a sensitive increase. In this context, topological optimization has emerged as a high potential tool. The topological optimization methods can be divided into two major approaches: the more classical approach generally called search optimization, and the methods based on inverse optimization. The main difference between search optimization and inverse optimization is that in the former the designs are systematically modified and the resulting structures are evaluated. On the other hand, the inverse method evaluates how any variation contributes to improve the desired objective function. The great advantage of the search method is that by evaluating the majority of possible configurations, the possibility of reaching the global optimum increases. However, this is achieved at the cost of long simulation time. There are several algorithms that seek to reduce optimization time, such as genetic algorithms. These algorithms do not need to evaluate all the possible configurations but they combine initial structures by emulating the evolution process, thus avoiding going through the path of unfeasible solutions.

In recent years, the interest in topology optimization in silicon photonics has increasing, as demonstrated by the following two high-impact publications using this approach: Piggott *et al.* demonstrated a wavelength demultiplexer [119]. To design this device, the authors adopted the first objective method, in which optimization is carried out in two steps, the first one not necessarily needing to comply with the Maxwell equations. A disadvantage of first objective method is that simulations are limited to a single wavelength. In order to obtain a broadband design, however, designs optimized for different wavelengths can be merged. On the other hand, Shen *et al.* implement a polarization divider, in which they use a modified version of the nonlinear direct-binary-search (DBS) algorithm [120].

In addition to the photonic devices mentioned above, topological optimization has been used in: photonic crystals [121], demultiplexers [122], modal converters [123], free-space metamaterial polarizers [124], and integrated metamaterial diodes [120], among

others. In the literature, there is not yet a direct comparison between the search method and the inverse methods and, therefore, it cannot be assessed which method is more suitable for topological optimization. According to recent publications, all methods have shown that they can be effective in projection of functional devices with small footprints. In a letter addressed to the editors of Nature Photonics [125], however, the three groups with more prominent contributions in the literature on the subject briefly discuss on the inverse topological optimization applied to the miniaturization of photonic devices. In addition the metrics to compare their performance with conventional devices were suggested.

Due to the large number of available state of the art topological optimization algorithms, we conducted several tests to evaluate which algorithms would be the most feasible to use for our designs. Among the algorithms that were evaluated are the free-of-gradient algorithms of the Free/ Open-source Library for Nonlinear Optimization NLopt of the MIT: constrained optimization by linear approximations (COBYLA), bound optimization by quadratic approximation (BOBYQA), NEWUOA + bound constraints, principal axis (PRAXIS), Nelder-Mead Simplex, Sbplx (based on Subplex). We also use the optimization algorithm based on the gradient available in Comsol: sparse nonlinear optimizer (SNOPT), method of moving asymptotes (MMA), and Levenberg-Marquardt. Finally, the differential evolution (DE) algorithm available in the GEMAC and encoded by Leandro Couto was evaluated. We decided to use the local optimization algorithm based on the gradient SNOPT, and also the DE algorithm. Although the SNOPT presents the best results in the preliminary tests, we choose two algorithms because the DE algorithm gives us the possibility of finding a global maximum and also offers us the possibility of having a binary distribution of the index of refraction that the former does not allow.

4.1 Compact antenna for fiber-to-chip coupling

As we presented in the section antenna applications, the most compact antenna for out-of-plane coupling is the focused grating. A focused grating is a periodic structure generally with a period of the order of the operation wavelength. When the grating is designed for single polarization, it has a $1d$ periodicity, whereas when it is designed for two polarizations, it has a $2d$ periodicity. Although these structures are widely known in the literature as grating couplers, some other authors, such as Eli Yablonovitch, who proposed for the first time the concept of photonic crystal, assure that these couplers are in essence a particular application of the photonic crystals [126]. The name photonic crystal originates from the fact that these structures have a photonic bandgap, that is, a range of wavelengths in which light cannot propagate through the structure. In this section we will describe the design of new non-periodic structures to perform coupling, which we will refer to as antennas, adopting the definition proposed by Balanis [22].

4.1.1 Design using Sparse Nonlinear OPTimizer algorithm

It is well-known that inverse topological optimization is an iterative process, as we can see in Fig. 4.1. The optimization process has several steps: the first step is to perform a finite-element or finite-difference analysis in a defined structure with some initial variables (in our case, an initial distribution of the refractive index) to find the performance metrics of the device and the value of the objective function. Then, a gradient based sensitivity analysis is computed generally using the adjoint method to limit the redistribution of the material to the areas of importance and to guide the device towards convergence [127]. Next, the variables are updated within the set of defined constraints. These steps are iterated until the objective function converges. At the end of the process, the variables are binarized to guarantee that there are no areas with intermediate refractive index values.

To perform our first optimization we used the optimization module of COMSOL Multiphysics. This module is very flexible, since any input variable of the physical model can be used as an optimization variable, and any output variable can be used as an objective function. The algorithm we chose for our optimization is based on the SNOPT algorithm, which was developed by Philip Gill from the University of California at San Diego and Walter Murray and Michael A. Saunders from Stanford University. The main advantages of this algorithm is that the objective function can acquire any form and the fact the great flexibility in the use of restrictions. This algorithm uses a gradient-based technique to find optimal designs and, when the underlying partial differential equation is stationary or time-dependent, analytical sensitivities with respect to the variable control of the objective function can be used. SNOPT is suitable for general non-linear programs

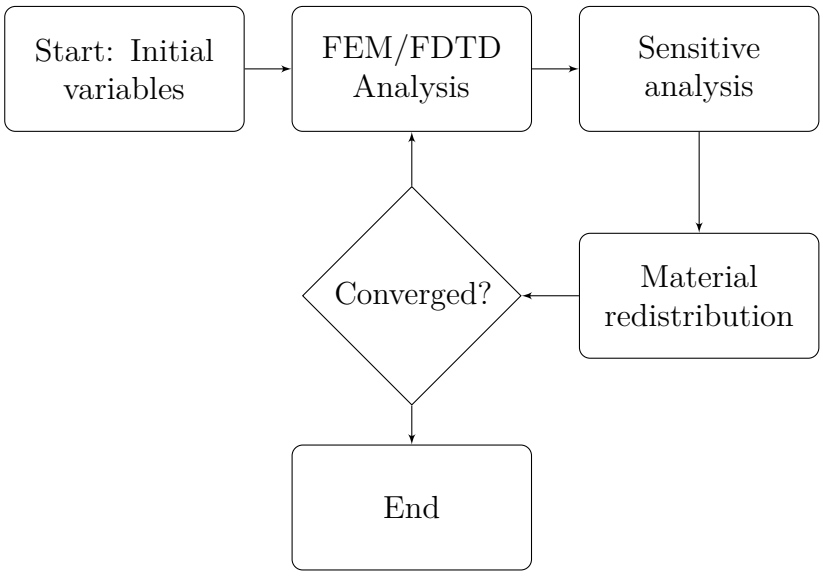

Figure 4.1: **Illustrative flux diagram of inverse topological optimization.** We chose for this optimization the SNOPT algorithm.

of the form [128, 129]:

$$\begin{aligned} &\underset{x}{\text{minimize}} && f_0(x) \\ &\text{subject to} && l \leq \begin{pmatrix} x \\ c(x) \\ A_L x \end{pmatrix} \leq u, \end{aligned}$$

where l and u are constant lower and upper bounds, $f_0(x)$ is a smooth scalar objective function, $A_L x$ is a sparse matrix, and $c(x)$ is a vector of smooth nonlinear constraint functions. We assume that the nonlinear functions are smooth and that their first derivatives are available.

"SNOPT uses a sequential quadratic programming (SQP) algorithm. The constraints of each QP subproblem are linearizations of the constraints in the original problem by introducing a set or slack variables $s = (s_1, s_2, ..., s_m)^T$, and the objective function of the subproblem is a quadratic approximation to the Lagrangian function" [128, 129]. The problem can then be written in the equivalent form:

$$\begin{aligned} &\underset{x}{\text{minimize}} && f_0(x) \\ &\text{subject to} && \begin{pmatrix} c(x) \\ A_l x \end{pmatrix} - s = 0, \quad l \leq \begin{pmatrix} x \\ s \end{pmatrix} \leq u. \end{aligned}$$

"The general constraints become the equalities $c(x) - s_N = 0$ and $A_L x - s_L = 0$, where s_L and s_N are the linear and nonlinear slacks. The basic structure of the SQP algorithm involves major and minor iterations. A major iteration results in a new solution candidate. For each major iteration, the optimization solver solves a quadratic-programming subproblem using a minor iterations" [130].

The objective function, or the merit figure of the device, was defined as the coupling efficiency between the field radiated by the antenna and field distribution of a standard singlemode fiber for a wavelength of 1550 nm. To calculate the figure of merit, we use the following equation (see the deduction in Appendix D):

$$\eta_n = \frac{1}{4 P_n P_{in}} \left| \int_s (e \times h_n^*) \cdot ds \right|^2. \tag{4.1}$$

where e is the radiated field, h_n is the field profile (guided mode) that we want the antenna coupler to generate, P_{in} is the input power, and P_n is the power of the desired field.

To find an antenna topology for ideal coupling we initially use as a region of optimization a box with a height of 220 nm, and a square base. This region is mapped using a uniform square mesh of the with resolution 100 nm × 100 nm. To ensure manufacturing simplicity, the mesh mapped in the silicon optimization region can only represent two heights within each voxel: 0 nm or 220 nm, resulting in a fully etched device. Since the

optimization algorithm is based on gradient, it is necessary to introduce a continuous design variable (in our case, $-2 \leq p_{ij} \leq 2$). This variable defines the refractive index of the optimization region according to:

$$n_{ij} = n_{\text{clad}} + (n_{\text{core}} - n_{\text{clad}})u(p_{ij}), \tag{4.2}$$

where, n_{clad} and n_{core} are the refractive indices of the cladding and the core materials (silicon dioxide and silicon), respectively, and $u.$ is a smooth step function with 2 continuous derivatives [$x < -0.05 \Leftrightarrow u(x) = 0$ and $x > 0.05 \Leftrightarrow u(x) = 1$]. As shown in the full computational domain [Fig. 4.2(a)], to feed the antenna we use the quasi-TE mode. Due to the high computational cost of the $3d$ finite element analysis we exploit the symmetry property of the problem to simulate only half of the domain, which allowed us to reduce the number of optimization variables and computation time. This computation was performed using a machine with an Intel core i7-6800k processor with 6 cores and a RAM memory of 128 GB. However, due to the insufficient RAM, the simulation was done without the substrate, as can be appreciated in Fig. 4.2(b).

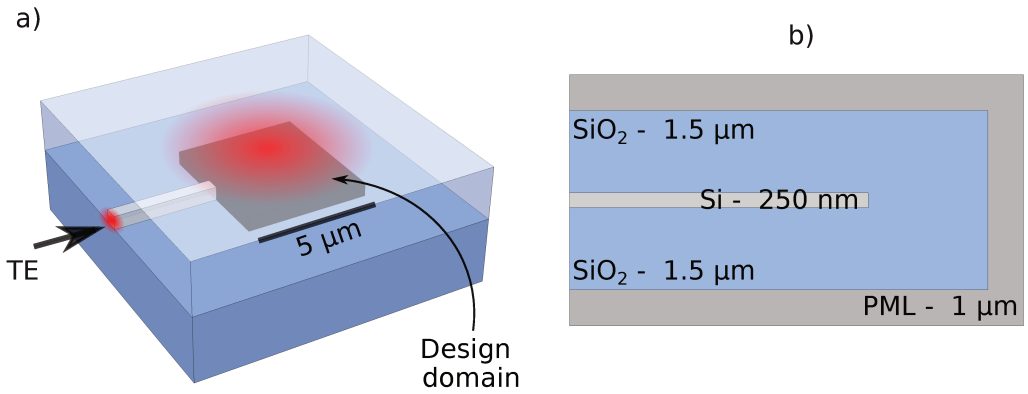

Figure 4.2: **Computational domain of simulation.** (a) Three-dimensional vision of the design. Note that simulation was carried out in half of the domain, taking advantage of the problem symmetry. (b) Lateral vision.

One of the most important optimization parameter is the size of the region to optimize, which must not exceed by much the modal diameter of a standard singlemode fiber. Another point to keep in mind is that the grating antenna coupler is composed of two stages: the first stage increases the mode diameter, whereas the second changes the direction of the light by almost 90°. Therefore, we can expect that the greater the size of the coupler the more efficiently these two tasks are performed. On the other hand, it is known that the greater the optimization region, the greater the computational effort. The resolution of the optimization (mapping) mesh is another relevant parameter. A fine optimization mesh tends to lead to structures with better performance, however, when it is too tight, it can lead to devices with a high manufacturing difficulty since

portions material of size below the fabrication resolution are generated. During our optimization process the following mapping mesh resolutions were tested: 20 nm × 20 nm, 50 nm × 50 nm, 70 nm × 70 nm, and 100 nm × 100 nm. Among them, the latter was chosen because it presented a more reliable design when considering our manufacturing process. An important point to highlight is that, in addition to the mapping mesh, the final structure of the device is influenced by the simulation mesh, that is the mesh employed by finite element method (FEM).

Fig. 4.3 shows the resulting objective function for two different regions of optimization: 5 µm × 5 µm and 7 µm × 7 µm, as well as the obtained designs. Both results were obtained after 70 iterations that required approximately 240 h on a computer with a processing speed of 1.25 TFlops. An important point to note is that the optimization with a region of 7 µm side converges to a coupling efficiency of −5.7 dB, which is higher than that of 5 µm side, −9.2 dB. That is, the efficiency is increased by 3.5 dB when the side of the optimization region is enlarged by 2 µm. Unfortunately, using a smooth function with 2 continuous derivatives (using a continuous distribution of the material), leads us to the existence of 'gray' areas, that is, areas that are not neither Si nor SiO_2. To overcome for this issue, the designs are binarized using a threshold of 0.5.

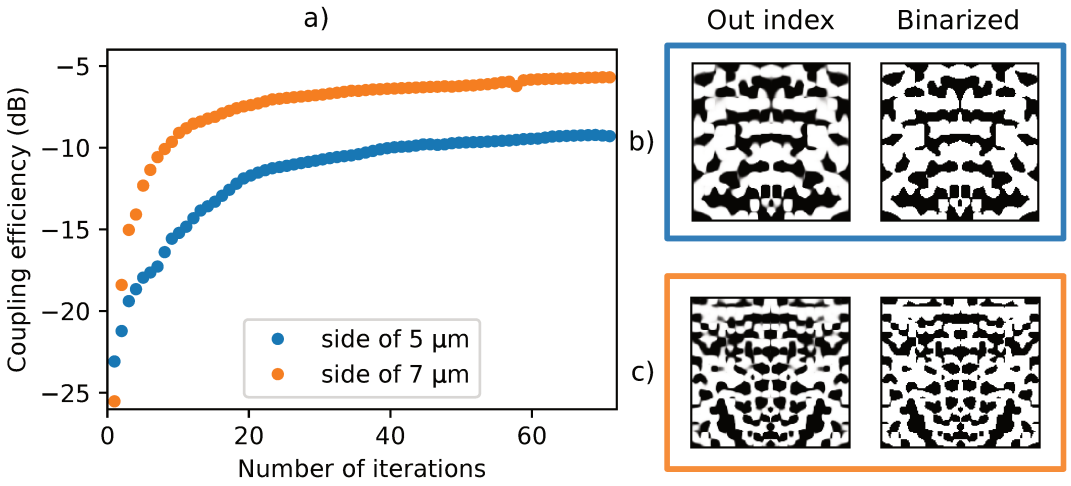

Figure 4.3: **Results of the inverse topological optimization process.** (a) Graph of objective function in terms of the iteration count for two different optimization regions, 5 µm × 5 µm and 7 µm × 7 µm. (b) Distribution of the refractive index after 70 iterations and (c) its binarization.

Once the binarization was accomplished, the performance of the best antenna design was tested through 3d finite-difference time domain (FDTD) simulations carried out in Lumerical. This software permits the efficient calculation of the objective function in a wide range of wavelength. As we previously mentioned, due to computational limitations, the optimization was done without considering the substrate. In FDTD simulations, we analyze the effect of the substrate by sweeping the size of the BOX and keeping the thickness

of the cladding at 1.5 µm, which result in a more realistic simulation scenario. We can see that a maximum coupling efficiency of −6.3 dB with a 3 dB bandwidth of approximately 60 nm is achieved for a BOX of 2.75 µm (antenna of 7 µm side).

The thickness of the BOX is, however, a fabrication constraint of our current process. In our case this thickness is 3 µm, whose performance was analyzed, obtaining a peak coupling efficiency of −9.3 dB and a bandwidth of approximately 60 nm. Although the coupling efficiency of the optimized antenna candidate for fabrication is 3 dB lower than the optimum, it should be noted that its bandwidth 1 dB is 40 nm, which means that it is 10 nm broader than that of a conventional grating coupler.

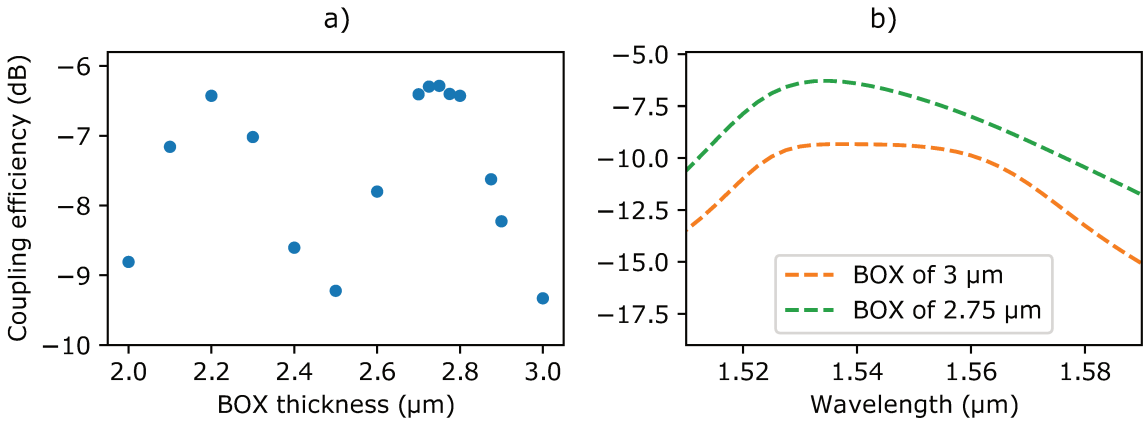

Figure 4.4: **Performance of the optimized antenna of area** 7 µm × 7 µm**.** (a) Coupling efficiency as a function of the BOX thickness. (b) Coupling efficiency versus wavelength for BOX thicknesses of 2.75 µm and 3 µm.

4.1.2 Design using Differential Evolution algorithm

In order to overcome the computational limitations of the inverse topology optimization using the SNOPT algorithm, we are investigating an alternative approach based on DE algorithm [131]. This search optimization is a more classic method whose objective is to change the designs systematically and then evaluate the resulting structures. One of the advantages of this method is that it allows us to map most of the possible configurations, therefore, it is more likely to reach a global optimum than with inverse optimization. The search algorithm also offers us the possibility of performing an optimization in several wavelengths, thus optimizing the coupling efficiency of the antenna in an operation bandwidth, and not only in a wavelength as it is generally the case when inverse optimization method is used.

The DE algorithm employed for our search topological optimization was proposed by Storn and Price in 1995 [131] to perform global optimizations over continuous search spaces. Although it requires few control variables and does not use derivatives, it is a simple and apparently very reliable method.

DE assumes that the problem variables to be optimized are coded as a vector of real numbers. The length of these vectors is equal to the number of problem variables, and the population is composed of NP vectors. We define a vector x_i^g, where i is the index of the individual in the population ($i = 1, 2, .., NP$), and g is the corresponding generation. Each vector is in turn composed of the variables of the problem $x_{i,m}^g$, where m is the index of the variable in the individual ($m = 1, ...n$). It is usually considered that the domain of the variables of the problem is restricted between a minimum value x_m^{min} and a maximum value and x_m^{max} [131, 132].

In Fig. 4.5 the iterative process of the DE topological optimization is represented. The process is initialized with a first population (first generation) that is randomly generated using a Gaussian distribution (which considers the minimum and maximum values of each variable). Next, a mutation process is implemented in which NP vectors are generated (mutant vectors) by combining three individuals chosen randomly, called target vectors, x_a, x_b, x_c. The mutant vectors (v_i^g) are obtained in the following way:

$$v_i^g = x_c + F \cdot (x_a - x_b), \tag{4.3}$$

where a, b, and c are different from each other, and F is a parameter that controls the mutation rate, whose value is within the range $[0, 2]$.

Recombination occurs once the mutant vectors are obtained (v_i^g). The recombination is done in a random way, comparing the mutant vectors with the original vectors (x_i^g) and obtaining the test vectors (trial vectors), u_i^g as follows:

$$u_i^g = \begin{cases} v_i^: & if\, rand(0,1) \leq CR \\ \\ x_i^g, & otherwise, \end{cases}, \tag{4.4}$$

CR is a parameter that controls the recombination rate. It is noteworthy that the comparison is made variable by variable, so the test vector will be a mixture of the mutant vectors and the original vectors. Finally, the selection is made simply by comparing the results of test vectors and those of the original ones, so that the vectors of the next generation will be the ones with the best objective performance function value.

The choice of the DE parameters, *i.e.* the size of population (NP), the scale factor (F), and the combination rate (CR), have a great impact on the optimization performance. To avoid the requirement for manual searching of these parameters we use an self-adaptive DE implementation based on Neighborhood Search (SaNSDE) [133]. SaNSDE self-adapts all its control parameters according to the statistical experience of gained during evolution, instead of other heuristic update rules. In this way, self-adaptation helps to adjust the scale factor parameter, and the combination rate. The population size, however, is a parameter fixed *a priori*.

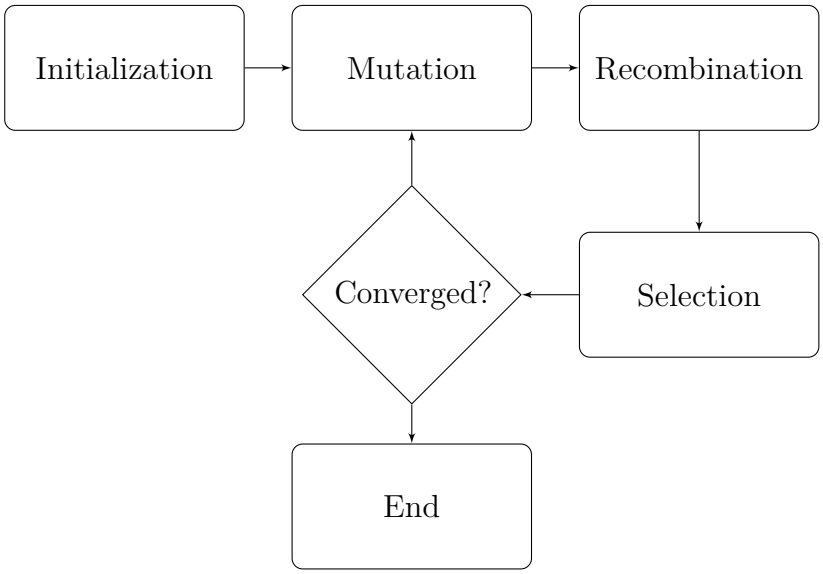

Figure 4.5: **Illustrative flowchart of search topological optimization.** We chose for this optimization the DE algorithm proposed by Storn and Price in 1995.

As we previously mentioned, topology search optimization algorithms need to evaluate a larger number of candidate structures than inverse optimization algorithms. Therefore the former leads to excessively long simulation times when dealing with three-dimensional structures. To avoid such long simulation times and the presence of gray areas in the distribution of the refractive index, we use the function expansion method to synthesize the distribution of the index in the design region [134]. Among the different bases, we adopted the Chebyshov polynomials so the refractive index can be expressed as follows:

$$n_{ij} = n_{\text{clad}} + (n_{\text{core}} - n_{\text{clad}})u(\xi_{ij}), \tag{4.5}$$

where n_{clad} and n_{core} are the refractive indices of silicon oxide and silicon, respectively. $u\cdot$ acquires the value of 0 or 1 depending on the value of ξ_{ij}. Therefore, the distribution of the refractive index of the design region is determined by the function ξ_{ij}, which can be expressed as the superposition of a set of analytic functions. Here ξ_{ij} is built using the Chebyshov polynomials of the first type as follows:

$$\xi_{ij} = \sum_{m,n} c_{mn} * T_m(i) * T_n(j), \tag{4.6}$$

$c_{m,n}$ being the Chebyshov coefficients that are, now, the variables to optimize. Consequently, we have a total of $m \times n$ optimization variables, which is further reduced to $m/2 \times n$ due to the symmetric nature of our problem.

Following the flow diagram of the DE optimization process presented in 4.5, we started by choosing the best distribution of the first generation individuals. For this, we tested a normally distributed population with different values of standard deviation (σ),

i.e. 100, 300, 650, and 3000 and different number of variables, i.e. 50 and 120. By doing so, we generate 250 random matrices of polynomials for each normal distribution that are then mapped using the Eq. 4.6 to build the first generation candidate antennas. In the evaluation process, we obtain the coupling efficiency of each individual at three different wavelengths 1530 nm, 1550 nm, and 1570 nm, by means $3d$ FDTD simulations carried out in python-meep. The stop condition in this case was 10 iterations (generations) for the case of 50 variables, and 15 iterations for the case of 120 iterations, this stop criterion was selected to minimize the simulation time. For these simulations we changed the previously used machine by the cluster composed of 3 computational nodes, each one equipped with two Intel processors of 8 cores-16 threads, and with 128 GB of RAM memory. This configuration allows the parallel evaluation of 9 individuals. Each of these evaluation takes approximately 50 min. In this way we get each iteration to take a time of approximately 1 day.

The results of the evaluation process of the different normal distributions for an optimization region of 7 µm side can be seen in Fig. 4.6. For the normal distribution with 50 variables and $\sigma = 100$, shown in Fig. 4.6 (a), reveals some convergence after the 10^{th} iteration, whereas for 120 variables and $\sigma = 3000$, shown in 4.6(b) this convergence is not observed. For the normal distribution with 120 variables for the standard deviation of $\sigma = 100$ a clear convergence is observe after the 7^{th} iteration, as it can be seen in Fig. 4.6(c). Therefore, after analyzing these results, we decided to initialize all our populations in the future with a Gaussian distribution of $\sigma = 3000$, as this configuration results in best preliminary performance.

We have made our first design with the technique DE in an optimization region of 7 µm side, on a SOI platform with a 250 nm silicon layer and a 3 µm BOX. For this, an initial population of 250 individuals distributed normally with $\sigma = 3000$ and 150 variables was used. The objective function was the coupling efficiency at three different wavelengths, 1530 nm, 1550 nm, and 1570 nm. Note that the crossover and mutation parameters were updated in an adaptive way with the SaNSDE using the coupling at 1550 nm as a reference. In addition, we limited the value of the variables in each individual to $[-10^8, 10^8]$.

Fig. 4.7(a) shows the results of the average coupling efficiency of each iteration for the three different wavelengths. In this graph we can see that population still does not seem to converge. On the other hand, in Fig. 4.7(b), we present the coupling efficiency of the best individual after each iteration, it is possible to appreciate in this graph that from the iteration 10 the best individual has a little variation. The best individual achieves a peak coupling efficiency of −14.8 dB, −14.3 dB, and −14.1 dB at 1530 nm, 1550 nm, and 1570 nm, respectively. Finally, the inset of the Fig. 4.7(b) shows the refractive index distribution of the optimum individual, that is the best individual after 21 iterations, when the optimization process stopped due to the low improvement in the individuals of the last iterations.

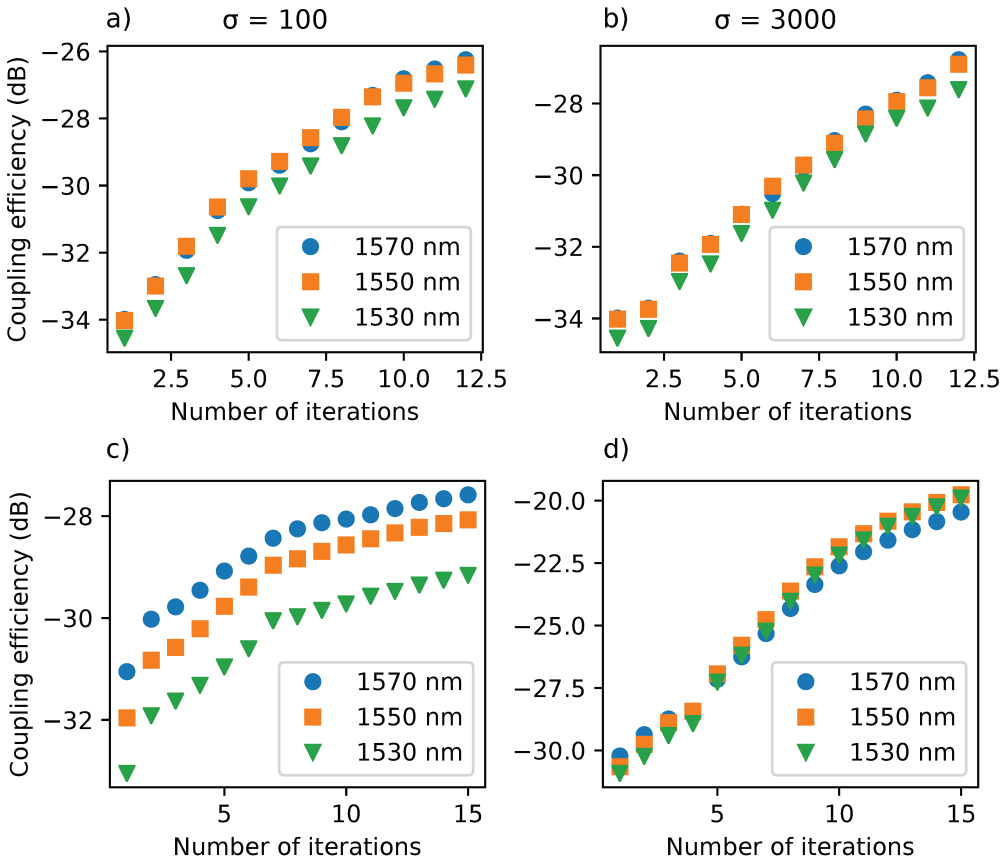

Figure 4.6: **Results of the coupling efficiency after 10 iterations of the search optimization with different Gaussian initialization distributions.** (a) $\sigma = 100$ (50 variables), (b) $\sigma = 3000$ (50 variables), (c) $\sigma = 100$ (120 variables), and (d) $\sigma = 3000$ (120 variables).

In order to avoid the low variability, the initial population was increased by 50 individuals. We also increased the size of the optimization region for a side box with a base area of 10 µm side, as well as the number of variables up to 162. This increase in size was based on the previously discussed preliminary results of the inverse optimization. These results reveal that the larger the optimization region is, the better the performance is. In addition, it it worth noting that the size increase is possible since, for our problem, the memory requirements using $3d$ FDTD are much lower than in $3d$ FEM. Fig. 4.8(a) shows the results of the average coupling efficiency after each iteration for the three different wavelengths. In this graph we can see that the population is already reaching convergence. On the other hand, in Fig. 4.8(b), we present the coupling efficiency of the best individual after each iteration. It is possible to appreciate that after the 15^{th} iteration the best individual's coupling efficiency present little variation. The best individual achieves a peak coupling efficiency of −20.2 dB, −19.4 dB, −18.8 dB at 1530 nm, 1550 nm, and 1570 nm, respectively. Finally, Fig. 4.8(c) shows the distribution of the refractive index of the best individual after the last iteration, that is, the outcome of the optimization. Inspection of the

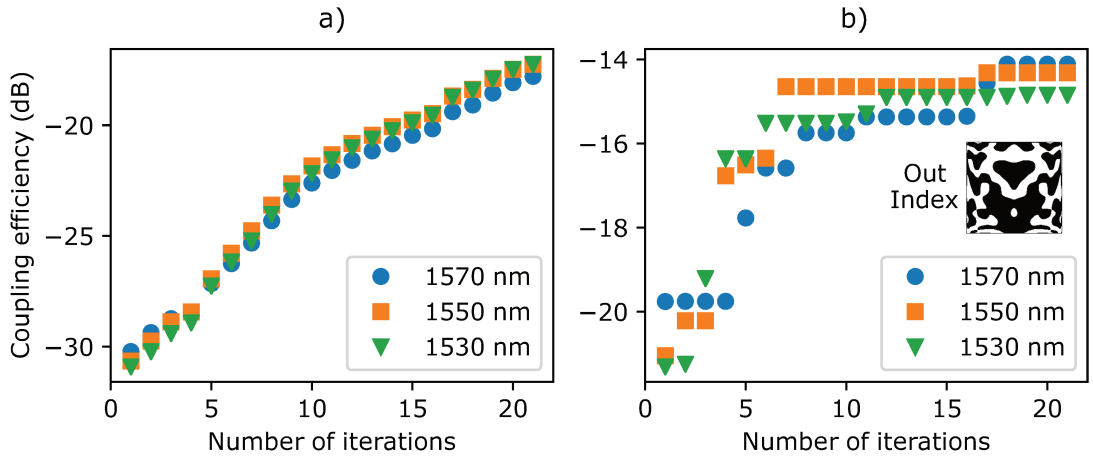

Figure 4.7: **Result of the coupling efficiency of the search topological optimization for a region with a 7 µm side.** (a) Average coupling efficiency of each iteration for the three different wavelengths. (b) Coupling efficiency of the best individual of each iteration for the three wavelengths. Finally, the inset shows the refractive index distribution of the best individual.

last population shows a reasonable variability, having at least 5 individuals with different refractive index distributions but with similar performance. Therefore, we will continue the iterative process until convergence is achieved and, then, use the best individuals for initial population of a second optimization stage considering a larger number of variables.

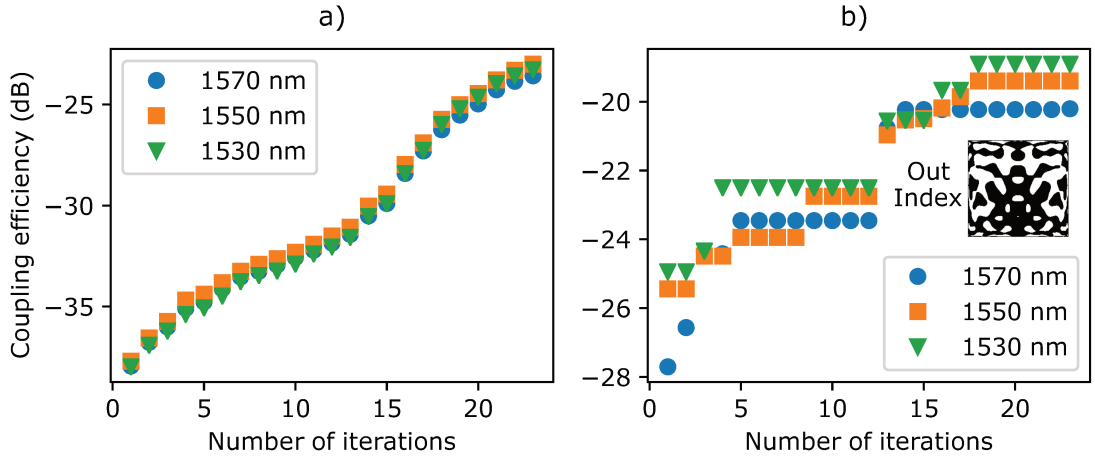

Figure 4.8: **Result of the coupling efficiency of the search topological optimization for a region with a 10 µm side.** (a) Average coupling efficiency of each iteration for the three different wavelengths. (b) Coupling efficiency of the best individual of each iteration for the three wavelengths. Finally, the inset shows the refractive index distribution of the best individual.

4.1.3 Characterization

In this section we will present the characterization of the in-house fabricated antenna in terms of coupling efficiency and the bandwidth of the polarization quasi-TE. In Fig. 4.9(a), the SEM image of the best optimized antenna is shown after the corrosion process. It should be noted that the SEM image of the optimized antenna reveals a high degree of similarity with the design presented in Fig. 4.4(c).

The measured peak coupling efficiency was −12.58 dB at a wavelength of 1543 nm, with a 1 dB bandwidth of 35 nm. The obtained results, however, are far from what was presented in the previous simulations. This can be attributed to the fact that measurements were carried out in a cladding-polymer chip because the deposition process of silica was temporarily unavailable. The polymer used as a coating is PMMA 950k, which has a refractive index of 1.49 and a thickness of approximately 1.2 µm. A direct comparison between the measured and the simulated resulted reveals that the peak coupling efficiency differs by 3.2 dB and the bandwidth by approximately 5 nm. These discrepancies can be ascribed to some manufacturing imperfections and the used polymer cladding.

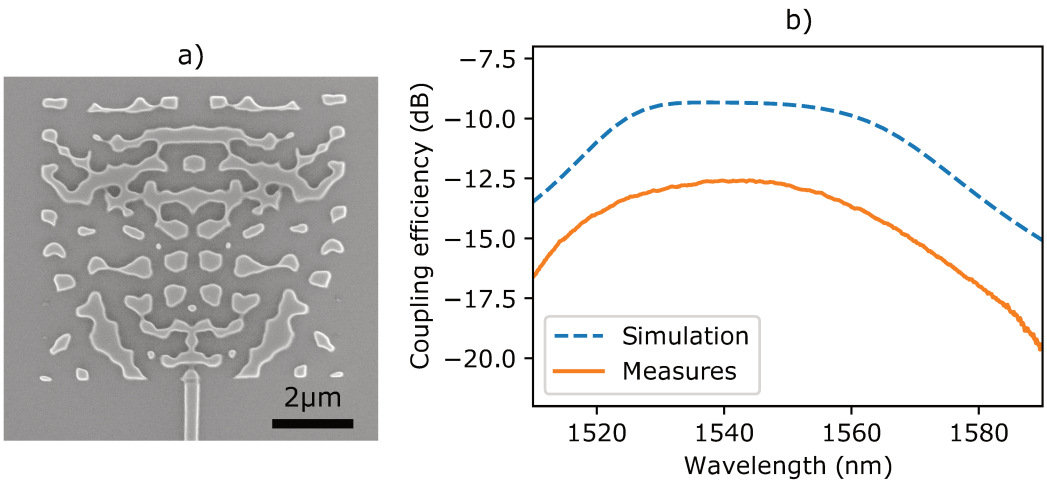

Figure 4.9: **Compact SOI antenna for fiber-to-chip coupling.** (a) SEM image of the optimized antenna fabricated at home. (b) Simulated efficiency of the antenna with silica cladding, and measurement of coupling efficiency of the optimized antenna with polymer cladding.

4.1.4 Conclusions

In this section, we presented the design, manufacture, and characterization of an antenna for coupling between a standard optical fiber and a CMOS compatible chip. The simulation results reveal that our best design has a fully vertical coupling efficiency of −6.3 dB and a 3 dB operation band of approximately 60 nm. This design, obtained using the SNOPT algorithm, has a unprecedented footprint of 49 µm^2, which

represents an approximate reduction of the 85 % with respect to conventional grating couplers [26, 76]. This reduced size enables the application of this antenna in coupling to multicore waveguides and even to few-mode fibers. However, due to the limitations of our home manufacturing process, this design cannot be fabricated. The design suitable for manufacturing has a lower performance, a peak coupling efficiency of −9.3 dB and an approximate 1 dB of 40 nm. On the other hand, experimental characterization reveals that the fabricated antenna has a coupling efficiency of −12.58 dB at 1543 nm, whereas, in terms of bandwidth, it remains close to that found in simulation. These significant discrepancies between the simulation results and the experimental results can be attributed to the lack of the silica cladding and, in a lesser degree, to fabrication imperfections.

In regards to the two different analyzed topological optimization approaches, which has not previously compared in a rigorous way, the results presented in this chapter suggest that the inverse method converges faster than the searching method but, it is more likely that the latter to reach a global goal. Another drawback of searching optimization is the required computational resources to evaluate the individuals at each iteration, however, this issue can be overcome by evaluating the different individuals in a parallel way.

4.2 Ultra-compact antennas for optical phased arrays

As we have already seen, an antenna with broadside radiation is highly desired. Then, it is expected that more complex structures than the grating-type antennas are required to reduce the backward reflection while maintaining a broadside radiation pattern. In this context, as we saw in this chapter topological optimization has become a potential tool. Topological optimization has been used in the optimization of metallic antennas in both RF and in the microwave band (1-10 GHz) [135], as well as at optical frequencies (500 THz) [136], but, as far as we know, it has not been used for the design of all-dielectric photonic antennas. In this section, the design of a dielectric antenna on the SOI platform is presented through a topological optimization. This antenna has a compact footprint of 1.78 µm × 1.78 µm and a bandwidth exceeding 100 nm. Far-field measurements reveal that the optimized design results in an almost vertical emission at wavelengths ranging from 1470 nm to 1550 nm, highlighting it as an excellent candidate for antenna arrays.

4.2.1 Design and simulation

The design of the antenna was carried out in COMSOL Multiphysics through the SNOPT algorithm, which starts from a non-optimized design (grating antenna) and looks for an optimized design minimizing a quadratic Lagrangian model [128]. To find an optimized antenna topology, we consider a box with a 220 nm height and a base of 1.78 µm × 1.78 µm as the optimization region. The base of the region was divided into

112×112 square cells with 16 nm side. Due to the commercial manufacturing process, the silicon layer can have four heights within each cell: 0 nm, 70 nm, 150 nm, or 220 nm. The optimization variables, then, are scalar quantities defined in each of those cells that are indirectly related to the thickness of the silicon layer in that cell. To be precise, the optimized scalar value $0 \leq p_{ij} \leq 4$ for the ij-th cell defines the refractive index of the 3 layers on the cell according to:

$$n_{ij} = n_{\text{clad}} + (n_{\text{core}} - n_{\text{clad}})u(p_{ij} - k) \tag{4.7}$$

where k can acquire the value of 1, 2, or 3 for the lowest (0-70 nm), medium (70-150 nm), and higher (150- 220 nm) layers, respectively. n_{clad} and n_{core} are the refractive indices of the cladding and the core materials (silicon dioxide and silicon) and $u.$ is a smooth step function with 2 continuous derivatives [$x < -0.05 \Leftrightarrow u(x) = 0$ and $x > 0.05 \Leftrightarrow u(x) = 1$]. The objective function, or device figure of merit, was defined as the sum of the far-field intensities in five different directions, which are shown in Fig. 4.10(a), for a constant input power in the simulation. These directions correspond to an angle 20° from the axis perpendicular to the substrate.

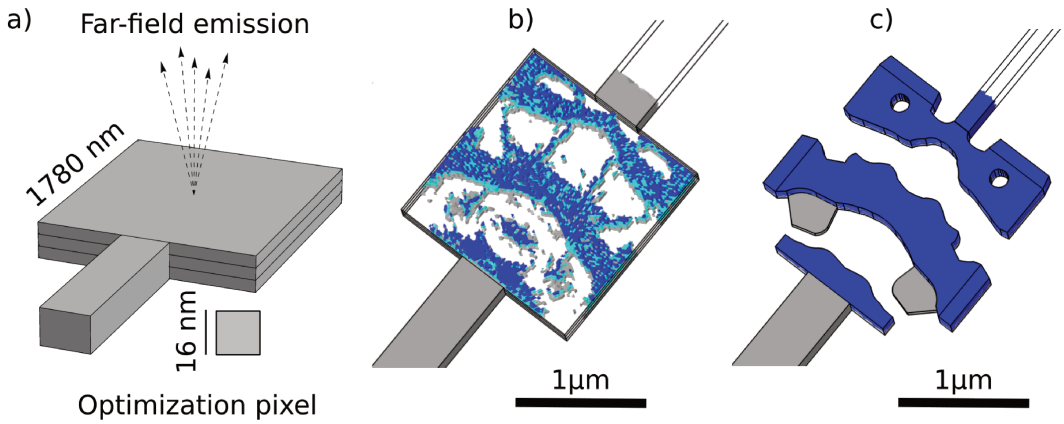

Figure 4.10: **Design of the small footprint optimized antenna.** (a) Optimization region indicating the pixel size, the four possible silicon layer heights, the dimension of the feeding waveguide, and the far-field radiation directions that are used in computing the figure of merit of the antenna. (b) Optimized design after 78 iterations. (c) Smoothed design suitable for fabrication. "Reprinted from [137]."

The time to simulate each iteration and the total optimization time were decreased by taking advantage of the symmetry of the problem (like the sec. 4.1.1), which allowed the reduction of the optimization variables and the simulation to only half of the domain. The result of the optimization algorithm after 78 iterations (which require 39 hours on a computer with a 128 GB RAM and a processing speed of 1.25 TFlops) is shown in Fig. 4.10(b). In this stage, the optimized structure presents a significant number of isolated small regions of silicon and sharp angles that do not comply with manufacturing

restrictions. To overcome this problem, the structure was spatially filtered resulting in the smoothed design shown in Fig. 4.10(c). According to simulations, this filtering does not significantly affect the radiation pattern of the device designed. It is noteworthy that, the different heights of the base break the vertical symmetry of the structure, favoring the radiation in the upward direction.

Before manufacturing, the performance of the antenna was tested using $3d$ FDTD simulations performed in Lumerical, which allows an efficient calculation of the objective function over a wide range of wavelength. It is important to note that components outside the numerical aperture of the lens used in the experiment are not presented in the simulations. Fig. 4.11(a) shows the upward efficiency (η_u) and downward efficiency (η_d), as well as the reflection (R) and transmission (T) coefficients, which reveal a wide 1 dB bandwidth of broader than 100 nm. According to these simulation results, the maximum emission efficiency reaches 80 % at 1466 nm, the 50 % being the power of input radiated upwards and the remaining 30 % downward. At 1550 nm, the ascending and descending emission efficiencies fall to 38 % and 28 %, respectively, resulting in a total radiation efficiency of 66 %. It is worth noting that the asymmetry between the powers emitted upwards and downwards is maintained throughout the bandwidth, decreasing only at longer wavelengths. With respect to reflection and transmission, the former reaches a minimum of 13 % at 1480 nm, while the latter does not exceed 9.6 % in the analyzed wavelength range.

The radiation properties of the designed antenna are illustrated at two wavelengths, 1470 nm and 1550 nm. Fig. 4.12 shows the near-field intensity and the far-field

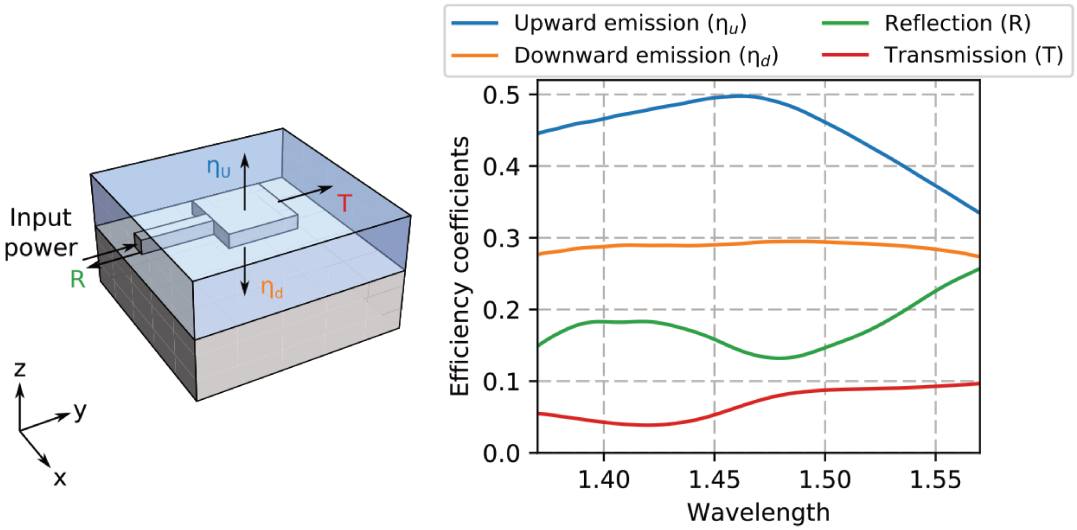

Figure 4.11: **Simulation emission efficiency of the small footprint antenna at wavelengths from 1375 nm to 1570 nm**. (a) Transmission and reflection coefficients, as well as emission efficiencies in the upward and downward directions. "Reprinted from [137]."

radiation patterns of the optimized antenna, respectively. As can be seen, the near-field radiation pattern has a single main spot. This spot is easily identified in Fig. 4.12(b), where the profiles of the near-field are represented in the directions indicated in Fig. 4.12(a). Comparing the profiles at the two wavelengths we can see a minimum change in the near-field pattern between the two wavelengths, which agrees with the wide bandwidth shown in Fig. 4.11. The far-field radiation patterns presented in Figs. 4.12(c) and (e), and obtained through a near-field to far-field transformation using the Fourier transform, differ only slightly into the two wavelengths. A change of approximately 4° in the direction of the main radiation lobe in a range of 80 nm can be seen. This attribute is desirable since it leads to an alignment independent of the wavelength between the transmitter and the receiver.

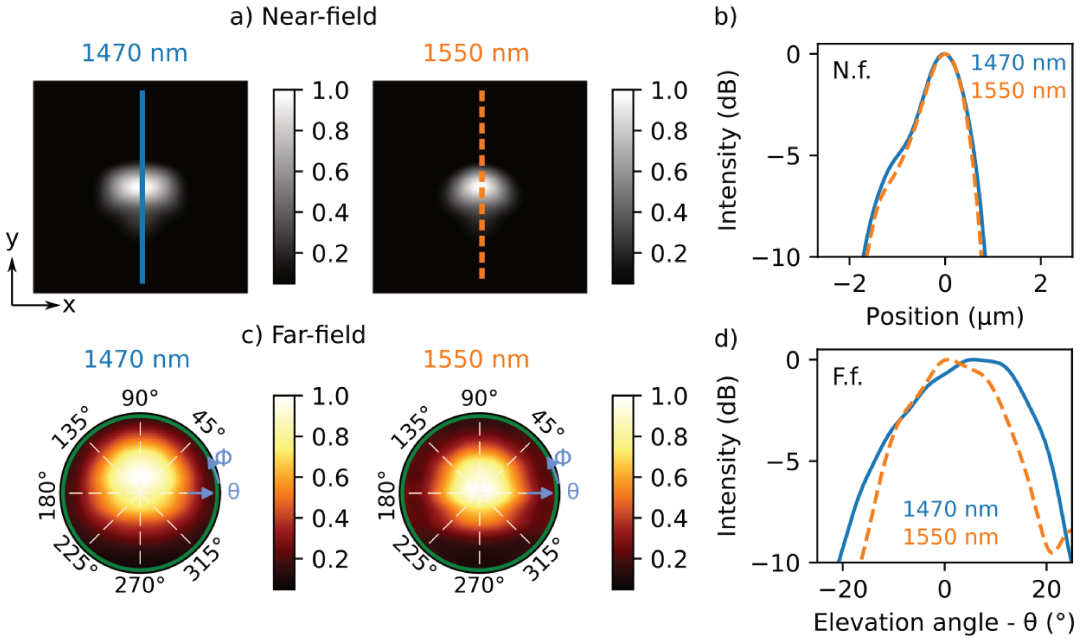

Figure 4.12: **Simulation near-field and far-field of the small footprint optimized antenna.** (a) Near-field intensity profiles at 1470 nm and 1550 nm. (b) Cuts of the near-fields in the directions indicated in (a). (c) Far-field radiation patterns at 1470 nm and 1550 nm. (d) Cuts of the far-fields (c) along the 90° azimuthal angle. N.f. indicates near-field, while F.f represents far-field. "Reprinted from [137]."

For reasons of performance comparison, a grating antenna similar to that reported by Sun *et al.* in [16] was also designed. This grating antenna was designed for a central operation wavelength of 1550 nm and has a footprint area of 3 µm × 2.8 µm. The antenna consists of 5 grating etchings, and has a grating period of 720 nm. The first grating etching is at a 70 nm height, which corresponds to a 32 % of the thickness of the silicon layer (220 nm). This first etching causes a vertical asymmetry in the grating and thus, induces that the upward emission power to be greater than that emission downward. As can be seen in Fig. 4.13(a) and (b), the near-field profile has a main spot and a lower power secondary spot. Comparing the profiles at the two wavelengths, we can see a change in the

near-field pattern, the main spot at the shorter wavelength is wider, while the secondary spot for the long wavelength grows approximately by 1.3 dB. In the far-field radiation patterns seen in Figs. 4.13(c) and (d), we can observe the appearance of a secondary lobe, but the most important point to note is that the direction of the direction of maximum radiation is close to −20°. This is an undesirable feature because, as we mentioned earlier, it poses serious alignment challenges, especially in data transmission applications.

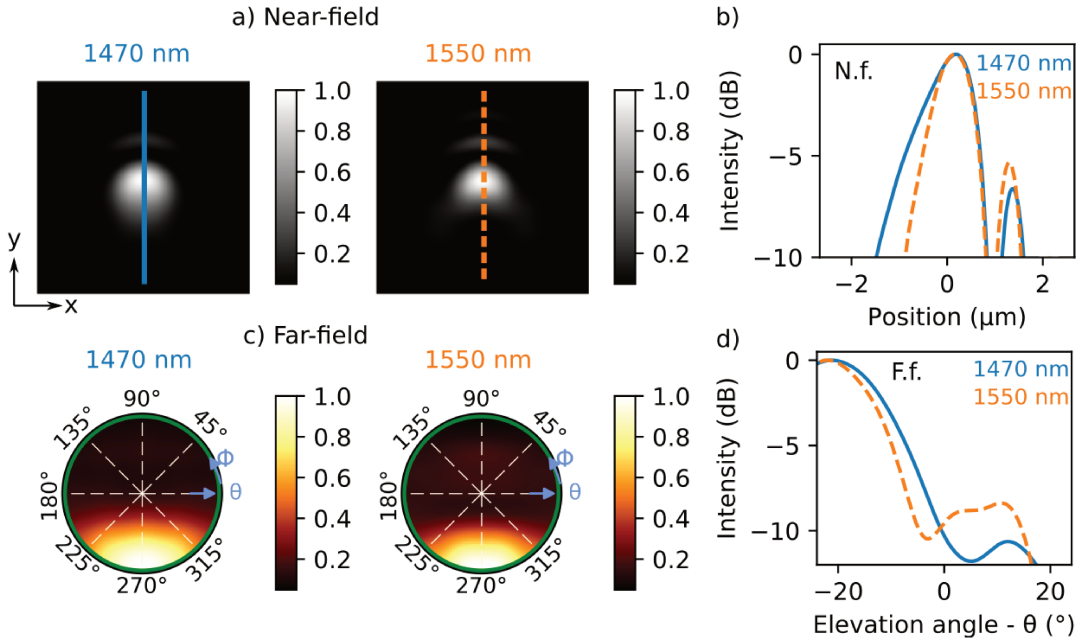

Figure 4.13: **Simulation near-field and far-field of the grating antenna.** (a) Near-field intensity profiles at 1470 nm and 1550 nm. (b) Cuts of the near-fields in the directions indicated in (a). (c) Far-field radiation patterns at 1470 nm and 1550 nm. (d) Cuts of the far-fields (c) along the 90° azimuthal angle. N.f. indicates near-field, while F.f represents far-field.

4.2.2 Characterization

Both the optimized and the grating antennas were manufactured at IMEC/Europractice using optical lithography on a SOI platform with 2 µm of buried silicon dioxide and a silica cladding of approximately 1.5 µm thick. This manufacturing process involved several limitations that were taken into account during the design process of the optimized antenna. In Fig. 4.14(a) and (b), SEM images of the optimized and grating antennas are shown, respectively. It should be noted that the optimized antenna presents a high degree of similarity with the design presented in Fig. 4.10(c). It is also worth noting that the optimized device has a footprint of 1.78 µm × 1.78 µm, that is, 60 % less than that of the grating antenna.

It is important to clarify that in this text we use the terminology commonly adopted in the characterization of optical antennas, where the near-field and far-field

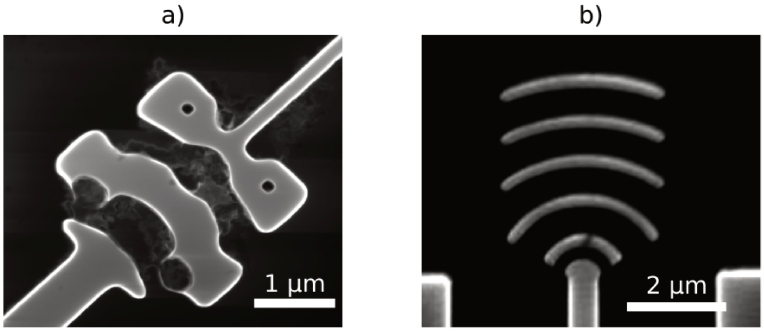

Figure 4.14: **SEM images of the fabricated antennas.** (a) Small footprint optimized antenna. "Reprinted from [137]." (b) Grating antenna.

measurements represent the images of real space and space-k, respectively. The near-field profile and far-field radiation patterns of the optimized antenna are shown in Figs. 4.15(a) and (c), respectively, while their respective cuts profiles made in the directions of maximum intensity are presented in Figs. 4.15(b) and (d). As far as the near-field measurements are concerned, they present similar radiation patterns to those of obtained through the simulation. In both cases, a single radiation lobe is observed. Comparing the simulated and measured near-field profiles, a reasonable correspondence is observed. The measured far-field radiation patterns shown in Fig. 4.15(c) are also similar to those obtained by simulation. However, they present an interference pattern that can be attributed to reflections in the optical system or on the silicon substrate [16]. This effect persists in Fig. 4.12(d). Nevertheless, the experimental results confirm two of the most important characteristics of the optimized antenna: on the one hand, the direction of the maximum radiation is almost orthogonal to the plane of the substrate (less than 4°) and , on the other hand, the far-field radiation pattern maintains its shape in a wavelength range of 80 nm. To reduce the effects of pixelation and noise on distant field radiation measurements, the camera images were processed using a Savitzky-Golay filter of 2^{nd} order.

The radiation patterns of the grating antenna are observed in Figs. 4.16(a) and (c), while the respective cuts profiles in the directions of maximum radiation are presented in Figs. 4.16 (b) and (d). With respect to the near-field images, a secondary spot can be seen both in the simulation and in the measurement for both wavelengths. This secondary spot is best seen in the profiles taken, where it is seen that this increases along with the wavelength. On the other hand, there is also a great concordance between the measured far-field radiation patterns shown in Fig. 4.16 (c) and those obtained by simulation. It is also possible to observe that the interference pattern observed in the remote field measurements of the optimized antenna persists. However, the experimental results confirm the two main characteristics of these grating antennas: on the one hand, that the direction of the maximum radiation is approximately 20° and, on the other hand, that the far-field radiation diagram presents a lobe of secondary radiation that increases

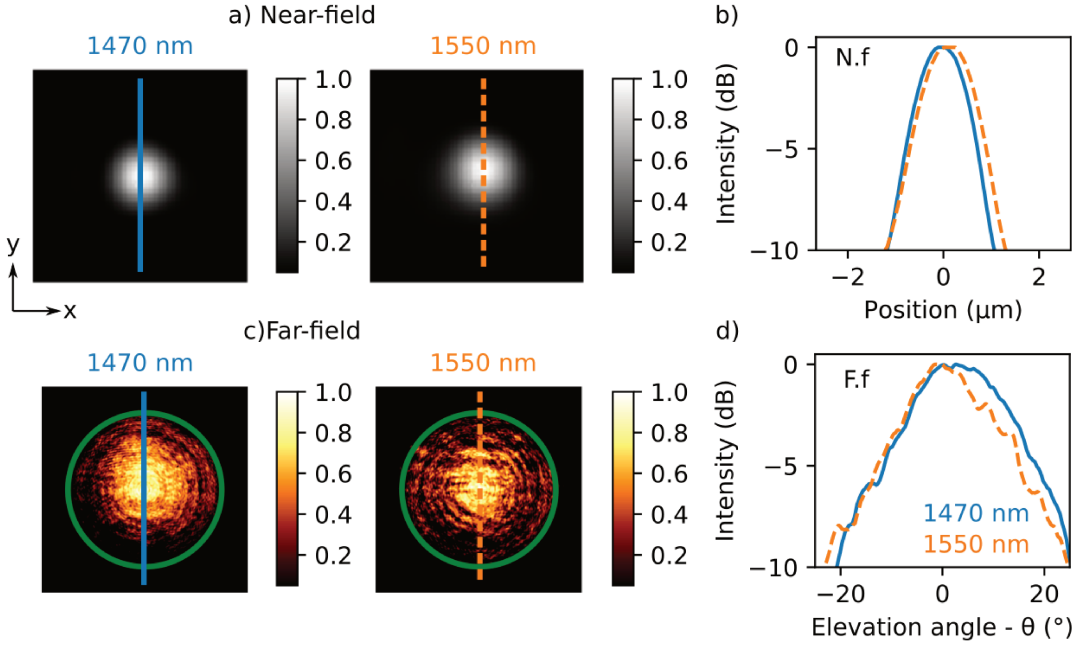

Figure 4.15: **Near-field and far-field measurements of the small footprint optimized antenna.** (a) Near-field intensity profiles at 1470 nm and 1550 nm. (b) Cuts of the near-fields in the directions indicated in (a). (c) Far-field radiation patterns at 1470 nm and 1550 nm. (d) Cuts of the far-fields (c) along the 90° azimuthal angle. N.f. indicates near-field, while F.f represents far-field. "Reprinted from [137]."

its level when increasing the wavelength.

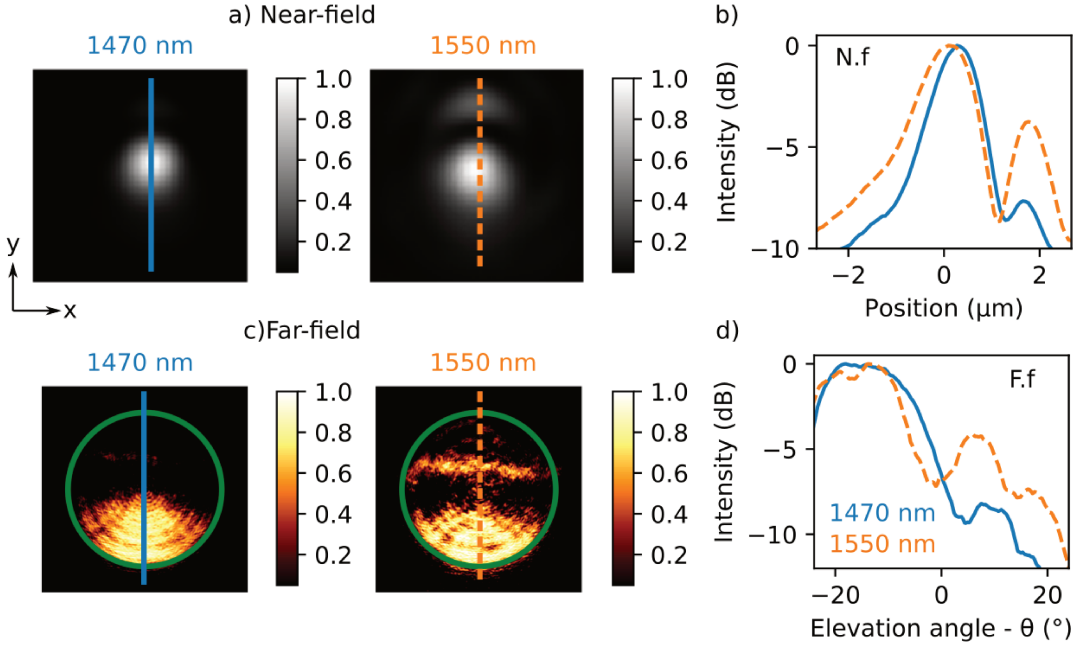

Figure 4.16: **Near-field and far-field measurements of the grating antenna.** (a) Near-field intensity profiles at 1470 nm and 1550 nm. (b) Cuts of the near-fields in the directions indicated in (a). (c) Far-field radiation patterns at 1470 nm and 1550 nm. (d) Cuts of the far-fields (c) along the 90° azimuthal angle. N.f. indicates near-field, while F.f represents far-field.

Finally, we evaluated the behavior of the optimized antenna as a chip-to-fiber coupler using two LF. The coupling efficiency obtained is presented in Fig. 4.17, revealing a bandwidth of 3 dB broader than 150 nm, which significantly outperforms the bandwidth of 60 nm that conventional out-of-plane couplers present [26].

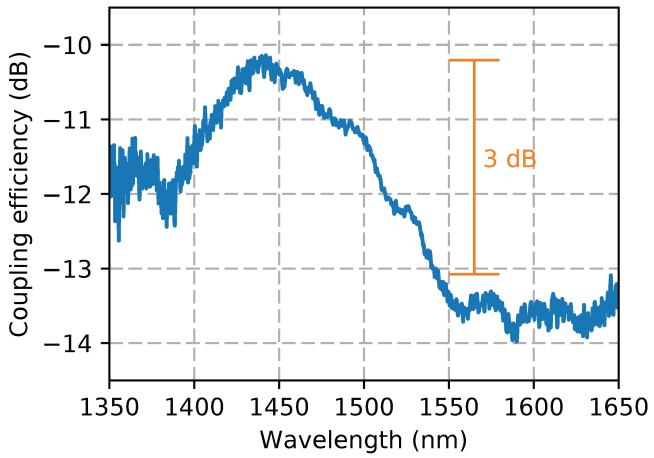

Figure 4.17: **Small optimized antenna for fiber-to-chip coupling.** Measured coupling efficiency at wavelengths from 1350 nm to 1650 nm. "Reprinted from [137]."

4.2.3 Conclusions

In this section we reported on the design, fabrication, and characterization of an ultra-compact nanophotonic antenna compatible with SOI with a broadside radiation pattern. A footprint as small as 1.78 µm×1.78 µm is achieved by topological optimization in four different silicon layers. For wavelengths ranging from 1470 nm to 1550 nm, the numerical simulations show a near-field profile practically independent of the wavelength, giving rise to a far-field radiation pattern with a deviation of only 4° from the side.

The experimental characterization reveals that the fabricated antenna maintains the main desired characteristics obtained through simulation, i.e. broadside radiation and a wide range of operating wavelengths. The reduced size of the optimized antenna, alongside with its radiation properties and the coupling bandwidth, makes this design an ideal candidate for the implementation of OPAs employed in applications such as communications within a multi-layered chip, lightweight coupling to multi-core fibers and few-mode fibers.

Chapter 5

Optical Phased Array Antennas

As we saw above, in antenna arrays where the separation between elements exceeds $\lambda/2$, a periodic distribution of elements presents an AF with several secondary lobes having the same power power level as the main one, i.e. SLL of 0 dB. This problem is specially critical in antenna arrays that operate at infrared and visible wavelengths. Even if spatial resolution has been improved in the latest generation manufacturing processes, the lack of an efficient small antenna still limits the minimum footprint of each antenna element, as well as its separation. This separation grows even more, up to several λ's, when the feeding network is implemented in the same layer of the antenna elements.

Due to the limitations described above, the reduction of the SLL in optical arrays is more challenging than in array antennas operating at RF frequencies. Several approaches have been proposed to address this problem. For example, applying a windowing amplitude (apodization) has shown a a SLL reduction in arrays where the separation between elements is less than $\lambda/2$. However, in sparse arrays, this approach does not reduce the power of the secondary lobes, keeping the SLL of the array [138]. To reduce the SLL of sparse antennas, the position of the elements must be controlled. This has been done in RF array antennas in several ways: genetic algorithms have been used in [139–141], while in [142, 143], particle swarm optimization has been used. The optimization of aperiodic tilling has also been reported in [144, 145]. These approaches, in addition to requiring long optimization processes, generally work only for large arrays of antennas and with inter-element separations not exceeding $5\,\lambda$. Such a scenario, although it is typical in sparse RF antennas, may not necessarily be suitable for the design of antenna arrays at optical frequencies.

A more promising approach has been adopted in [146–148] using a bio-inspired solution. The distribution of the antenna elements is performed according to the Fermat spiral, which is a particular case of an Archimedean spiral that appears naturally in the plant morphogenesis. Moreover, this spiral has an efficient packaging property [149]. This array has been adopted in RF and in satellite communication applications where arrays had a small elements separation. Recently, Niaz and his co-authors demonstrated the

use of Fermat's spiral in a reflectarray at 16 GHz but with only 0.6λ of spacing between elements [150].

In this chapter, we will experimentally demonstrate that arranging the antenna elements according to the Fermat spiral significantly reduces the SLL even in arrays with few widely spaced elements, which are specially important in applications at optical frequencies and in integrated photonics. In near-infrared frequencies and, using the SOI platform, we show that an array of 8-element antennas following the proposed design reduces the SLL by around 1 dB with respect to a periodic array of same size. In addition, we also use a SLM operating at visible wavelength (633 nm) to emulate larger arrays, demonstrating that the Fermat spiral works as expected for arrays with up to 64 elements spaced $581\,\lambda$, a result well beyond what is generally considered a sparse arrays. These results reveal a reduction of the SLL of 5.9 dB in an array of 25 elements and 6.9 dB in an array of 64 elements, following the theoretical predictions.

5.1 Side-lobe level reduction in two-dimensional optical phased array antennas

For the design of an array of antennas with low SLL operating at λ=1.55 µm, we use the Fermat spiral definition presented in [146–148] and implemented in [150]. According to the aforementioned works, the position of the n-th element of the array ($n = 1, 2, 3, \ldots, N$) in polar coordinates is given by:

$$\rho_n = \frac{d}{K}\sqrt{n} \tag{5.1}$$

$$\phi_n = n\pi\left(3 - \sqrt{5}\right) \tag{5.2}$$

where ρ_n is the distance from the n-th element to the origin, ϕ_n is the azimuthal angle, and $K = \sqrt{5 - 4\cos\phi_3}$ is a normalization factor that guarantees that d is the minimum element separation distance from center to center. One point to keep in mind is that the element corresponding to the position $n = 0$ was discarded because it is located very close to its neighbors. Another point to note is that, due to the irrational golden angle $\pi\left(3 - \sqrt{5}\right)$, each element is in a different direction from the center of the spiral, as desired.

The packaging efficiency of the arrays with elements distributed following Fermat's spiral is lower than in the periodically arranged arrays. For example, for an arrays of 4-elements, the effective area increases by 63 %, while for arrays of 64-elements, the increment of the area is only 25 % [148]. However, as we see in the Fig. 5.1, the arrays that follow the Fermat spiral reduces the SLL efficiently at a wavelength of 1550 nm. We chose two aperiodic arrays with 64-elements and with a minimum separation distance

between elements of 0.5 λ and 4 λ, respectively, to perform a fair comparison with the square arrays presented in Fig. 2.7. By direct inspection, we noticed that the SLL of the aperiodic arrays is smaller. Whereas for the array with a minimum separation of 0.5 λ the reduction of SLL is 3.9 dB, for arrays with inter-element separation of 4 λ, the SLL reduction rises up to 10.9 dB. It is also possible to notice from Figs. 5.1(b) and (e) that as the separation between the elements increases, the beam width of the main lobe decreases. Another disadvantage of this arrangement, when compared with the uniform array, is that the background noise level increases as can be seen in Fig. 5.1(e).

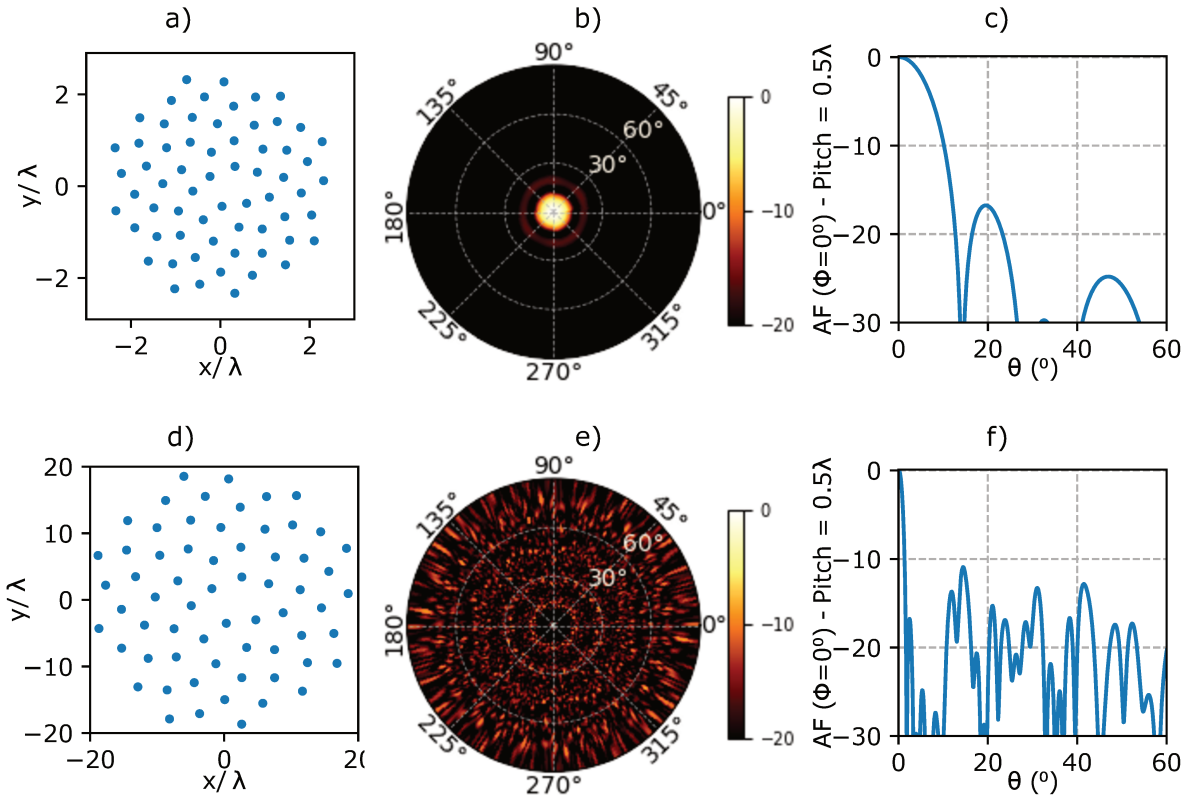

Figure 5.1: **Array factor diagram of aperiodic distributions for different antenna pitch values.** (a) and (d) Arrays composed of 64-elements arranged following the Fermat spiral with separation of $\lambda/2$ and 4λ, respectively. (b) and (e) Full array factor diagram for a 64-elements Fermat arrays with pitch of $\lambda/2$ and 4λ, respectively. (c) and (f) Detailed view of the normalized array factor near the main lobe for $\phi = 0$.

To evaluate the SLL reduction of the array with elements arranged according to Fermat's spiral, we extended this analysis for different separation distances and different sizes of arrays. The results are presented in Fig. 5.1 for up to 1024-elements and up to a minimum distance of 64 λ. We can clearly see that SLL decreases as the number of elements of the array increases to 1024-elements, where we have a maximum SLL reduction of around 18.6 dB. We can also see that as the number of array elements is increased, the SLL becomes almost independent of the minimum inter-element separation. We note that for 1024-elements there is a difference of SLL of only 1 dB when the separation increases

from 1 λ to 64 λ. Finally, we can point out that, that Fermat arrays present a reduced SLL not only for short minimum separations (0.5 λ), but also for arrays with long minimum separation distances. Fig. 5.2 can also be interpreted as an array with constant element spacing that operates over a large range of frequencies. Therefore, it can be said that this way of distributing the elements maintains a low SLL even in a wide range of frequencies.

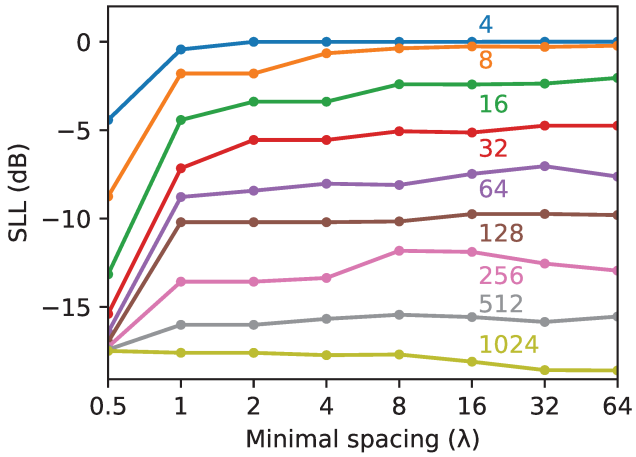

Figure 5.2: **SLL of Fermat's spiral array for different number of elements and antenna separation.** The results range from 4 to 1024-elements and from a minimum distance of 0.5 λ to 64 λ.

5.1.1 Nanophotonic phased arrays

The designed antenna arrays were fabricated at IMEC/Europractice on SOI platform with a silicon layer of 220 nm, with three different levels of corrosion. The array elements were an optimized design similar to that presented in the previous section and published in [137, 151]. An important feature of this antenna design is the direction of the maximum radiation, which is orthogonal to the substrate plane. This characteristic is critical in our measurements because it allows us to capture the main lobe of the element within the numerical aperture of the lens, thus allowing a better estimation of the AF. The figure 5.3 shows a SEM image of the manufactured antenna array with a uniform element distribution and with elements distributed according to the Fermat spiral. The critical limit for the element separation arises from the feeding network shown in Fig. 5.3(c), since a separation of 1 µm is required between the waveguides to avoid light coupling, as well as a minimum bending radius of 5 µm to avoid high losses.

Due to the complexity and size of the feeding network, our analysis was limited to arrays with 8 antenna elements. However, this number could be increased significantly by further separating the antennas or using a multilayer feeding network. For comparison purposes, two different arrays were fabricated: a uniform array of 4 × 2 elements with a 9 µm separation, and an aperiodic array of 8 elements where the elements are organized

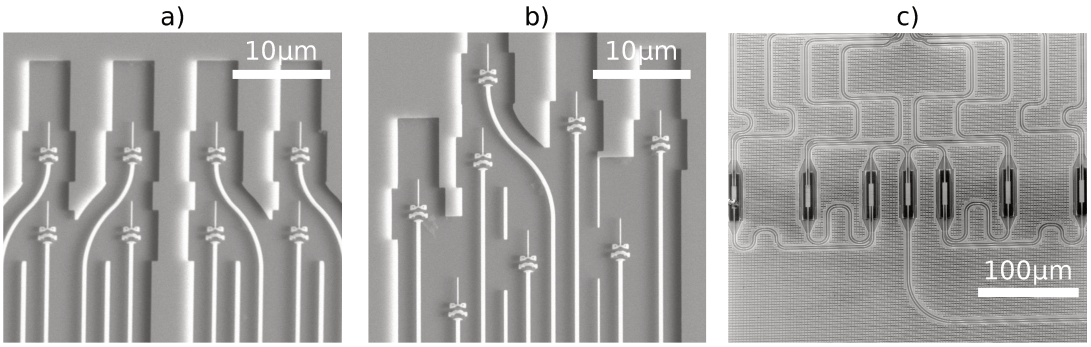

Figure 5.3: **SEM images of the fabricated SOI-based arrays and their feeding network.** (a) Uniformly distributed array antenna. (b) Non-uniformly distributed array antenna. (c) Distribution network. "Reprinted from [11]."

according to the Fermat spiral with a minimum distance of $d = 9\,\mu\text{m} = 5.8\lambda$. It is important to mention that in both arrays special care was taken to ensure that all the elements were fed with the same power and signal phase. The power was divided equally among the 8 elements through a three-stage cascade of 3 dB power dividers, which was characterized at IMEC, showing an almost ideal ratio of 1:1 (power imbalance of 0.01 dB). The feeding network was designed to supply the same amplitude and phase in all antenna elements. For that purpose, waveguides with the same length and number of curves and equal radii of curvature were used, so that no adjustment mechanism of phase or amplitude is necessary.

Next, the SLL of the two fabricated array antennas was analyzed: the uniformly distributed array presented in Fig. 5.3(a) and the one with the configuration of Fermat spiral, which is presented in Fig. 5.3(b). The position of the antenna elements can be clearly identified in the near-field measurement of the uniform array [Fig. 5.4(a.i)] and the spiral array [Fig. 5.4(a.ii)], which shows that there is no radiation coming from the feeding network and that all the elements of the antenna radiate with approximately the same intensity, as expected. Figs. 5.4(b.i) and (b.ii) show the far-field theoretical patterns for both configurations. The presence of secondary lobes of high intensity in the radiation pattern of the uniformly distributed array is clear. For the aperiodic array, on the contrary, the main lobe dominates, while the secondary lobes are redistributed due to the aperiodic positioning of the elements.

The experimental measurements presented in Fig. 5.4(c.i) and (c.ii) for the uniform and spiral arrays, show a significant reduction of the SLL of the aperiodic array with respect to the uniform. The secondary lobes in the radiation pattern of the uniform array can be easily identified, since it has intensity valleys between them. On the other hand, in the aperiodic arrangement we can see a single main lobe in the direction orthogonal to the substrate. The level of the secondary lobe, however, can be seen most clearly when we observe the profile of the normalized intensity along a certain azimuthal angle. In our

case, a fair comparison forces us to choose the angles in which the secondary lobe is more intense, which are identified in Fig. 5.4(c) as superimposed white lines. The resulting intensity profiles for the aperiodic and uniform arrays are presented in Fig. 5.4(d) and (e), respectively. Since we have adopted the definition of SLL as the relation between the secondary and main lobes of the AF, we must first calculate AF by calculating the difference (in dB) between the normalized pattern of a single element and the normalized pattern of the arrangement. Consequently, we also plot the radiation pattern of a single element at the same azimuthal angle as a reference and calculate the SLL as the difference between them. After performing this calculation, the results reveal that, as expected, that the SLL of the uniform array is close to 0 dB, whereas for the aperiodic array it is around 0.9 dB. That is, we show a reduction of the SLL of almost 1 dB in the arrangement of antennas of 8 elements in the SOI platform with a minimum element separation of $5.8\,\lambda$ (9 µm).

5.1.2 Sparse arrays in visible range

To evaluate the performance of the Fermat distribution in the SLL reduction with a greater number of antenna elements, the emulation of several configurations of array antennas in the visible range was performed using a SLM, as shows in Fig. 5.5(a). As with the integrated arrays, far-field measurements were made using a $6f$ optical system. The configuration of each array is not fixed, being that it can be modified by defining it in the mask that is written on the SLM located in the Fourier plane of the target L_5. For this flexible configuration, a continuous wave He-Ne laser operating at 633 nm is used, which first couples to a singlemode fiber to improve the purity of its fundamental mode. Subsequently, a 1 mm CO, a LP and a half-wave plate ($\lambda/2$) are used to adjust the polarization of the beam and maximize the reflectance efficiency of the SLM. To illuminate a larger area of the SLM, a lens system consisting of L_3 and L_4 with focal lengths of 50 mm and 100 mm expands the beam, which results in a beam with a full-width at half maximum (FWHM) diameter of 3.5 mm. A Holoeye PLUTO - VIS phase-only SLM is then used in reflection mode to direct the beam to the mirror (M) and the lens L_5 located at its focal length of 300 mm) that focuses the beam on a silicon CCD camera.

This setup allows the configuration of different arrays by defining the desired phase mask in the SLM. In our case, the phase mask is generated by multiplying a blazed grating, Fig. 5.5(b), with a binary matrix representing the elements of the array, Fig. 5.5(c). The use of a grating as an aperture antenna allows us to capture the radiation pattern in the direction of its first diffraction order, thus decreasing the level of background signal and noise. At this point, it is important to say that the secondary lobes that appear in the far-field are not the result of the different blazed grid orders, but are a consequence of the configuration of the array, which is directly related to its AF . To perform the

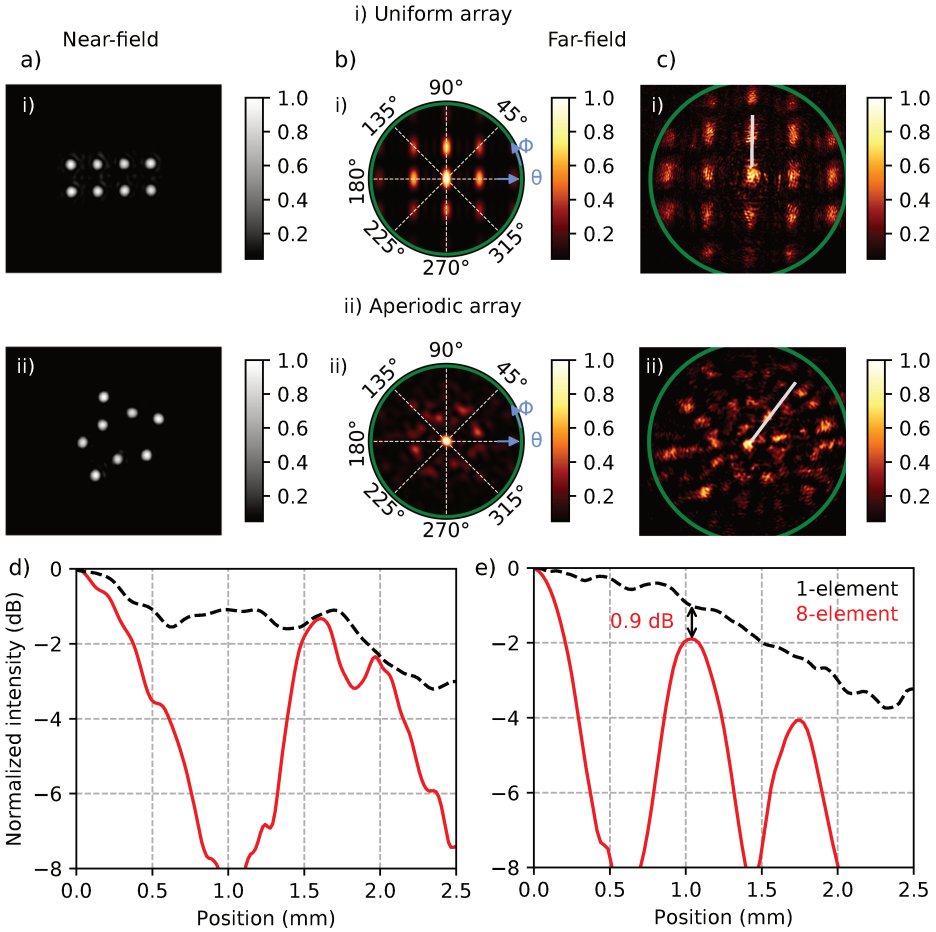

Figure 5.4: **Characterization of the fabricated photonic arrays.** (i) Uniformly distributed array and (ii) Fermat's spiral array. (a) Near-field measurements. (b) Simulated far-field radiation pattern. (c) Measured far-field radiation pattern (the green circumference represents the numerical aperture of the objective, around 24°), (d) Far-field radiation intensity for a single element and the uniformly distributed array in the azimuthal angle where the secondary lobe is more intense, and (e) same as (d) but for the spiral array. "Reprinted from [11]."

measurements of the SLL, the period of the blazed grid was set to $\Lambda = 102.5\,\mu m$, in order to maximize the reflection efficiency of the first refraction order up to 83 %. The binary matrices representing the different configurations of the arrays were formed by square openings with sides of 262.6 µm (415λ), as shown in Fig. 5.5(c) for a periodic array and an aperiodic of 64-elements. The center-to-center separation between elements in the periodic array is 367.7 µm (581λ), whereas for the Fermat spiral this value is used as the minimum separation d.

The phase masks and the far-field radiation patterns captured from the uniform arrays are shown in Figs. 5.6(a) and (b), respectively. Sub-figures (i) and (ii) correspond to arrays with 25 and 64 elements. The color lines in Fig. 5.6(b) represent the directions where the SLL is maximum. Fig. 5.6(c) shows the normalized intensities along these directions for the two arrays, as well as the radiation pattern of a single element in the

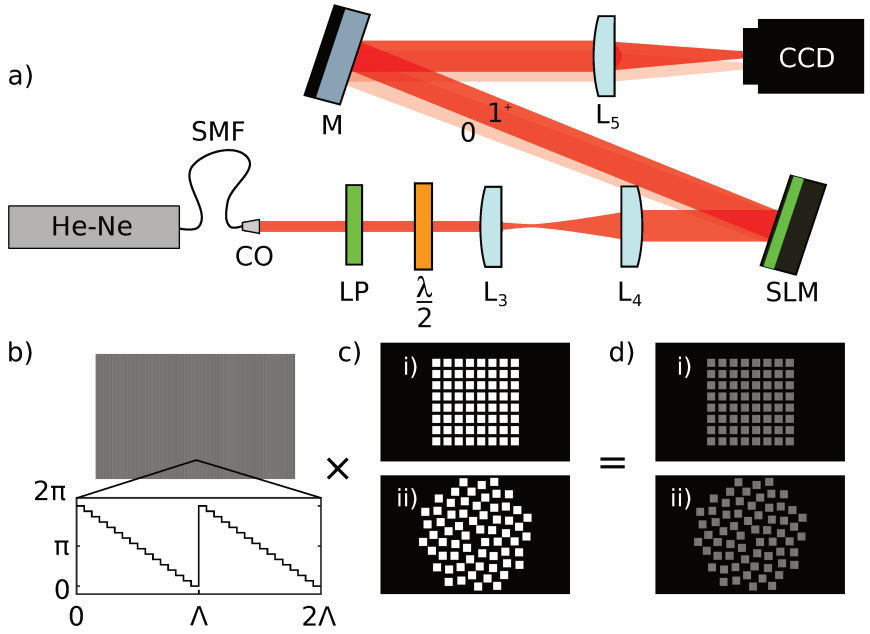

Figure 5.5: **Sparse array evaluation setup for flexible configurations.** (a) Setup for emulation of photonic arrays at 633 nm. SMF: single mode fiber; CO: collimator; LP: linear polarizer; L_3, L_4, and L_5: lenses; SLM: spatial light modulator; M: mirror. 0 and 1^+ indicate the two main diffraction orders. (b) Blazed grating on the SLM. The detailed view shows the phase profile for 2 grating periods, Λ. (c) Binary matrices (example with 64-elements) for (i) periodic and (ii) Fermat spiral arrays. (d) Resulting phase masks for the same arrays in (c). "Reprinted from [11]."

same directions. Similarly, Figs. 5.6(d), (e), and (f) represent phase masks, far fields and normalized intensities for aperiodic arrays. For the comparison, the same number of elements is used as in the two arrays. The high level of SLL for the periodic array is evident in the far-field images whereas, for the aperiodic case, the intensity levels of the secondary lobes are lower.

The SLL for the different array configurations are calculated analogously to the case of periodic array antennas, that is, extracting the AF by subtracting the normalized radiation pattern from a single element of array antenna. In Fig. 5.6(c), we can see that the SLL of the uniform arrays is, as theoretically predicted, 0 dB for the two arrays. On the other hand, the spiral arrangement of the elements results in a radiation pattern with a significantly lower SLL [Fig. 5.6(d)], which reveals a reduction of SLL of 5.9 dB and 6.9 dB for arrays with 25 and 64 elements, respectively. It is also noteworthy that, for the arrays that follow the Fermat spiral, the maximum intensity of the secondary lobe is reduced as the number of elements grows.

These experiments were repeated for array sizes ranging from 25 to 64-elements. The obtained results are presented in Fig. 5.7 alongside with the SLL of the uniform and Fermat arrays made of silicon. As expected from the theoretical analysis represented by solid lines, the uniform distribution leads to AFs with secondary lobes as intense as

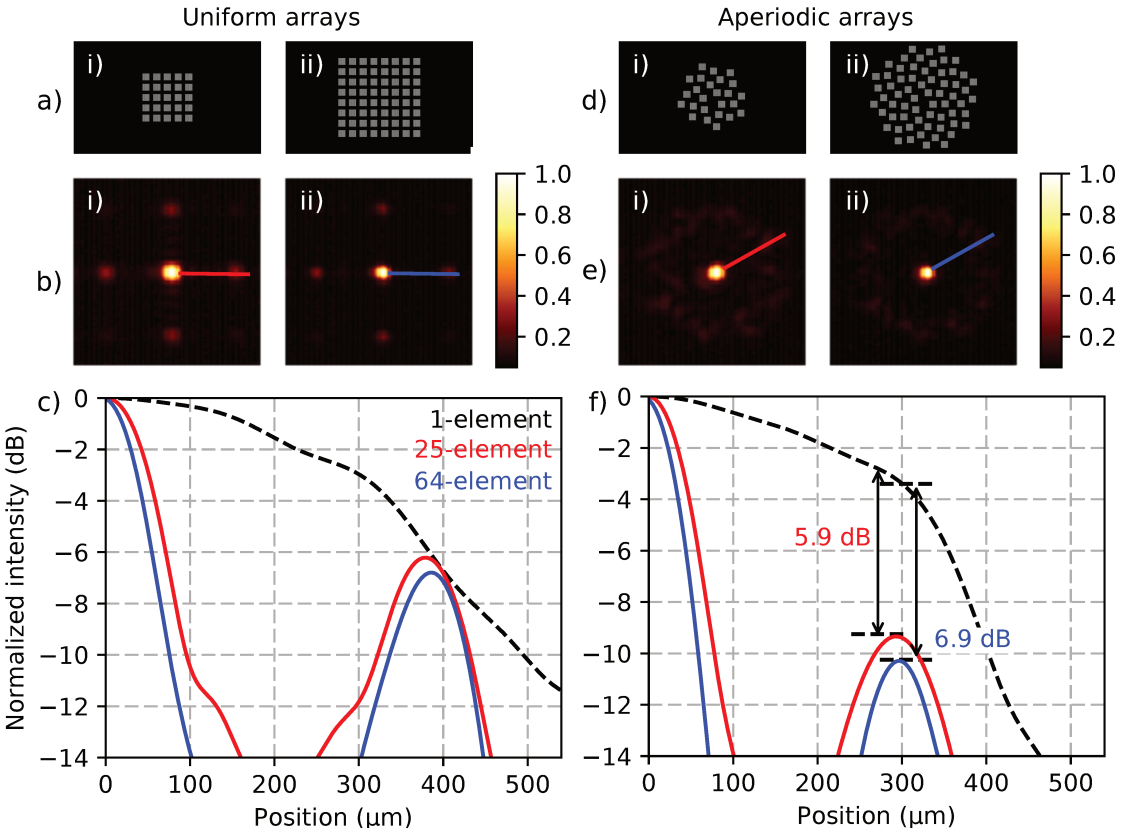

Figure 5.6: **Far-field radiation patterns for different array configurations.** (a) Phase masks of the emulated unifrom arrays. (b) Captured far-field radiation patterns for uniform arrays with (i) 25, and (ii) 64-elements. The lines in (b) represent the directions where the secondary lobe is maximum. (c) Normalized far-field intensity along the lines of maximal SLL, represented by the color straight lines in (b). For reference, the radiation intensity for a single element is represented in the black dashed line. (d-f) Phase-masks, captured far-fields, and normalized far-field intensities in the maximal SLL directions for Fermat's spiral with 25, and 64-elements. "Reprinted from [11]."

their main lobes, regardless of the size of the array. On the other hand, in the aperiodic arrays, the intensity levels of the secondary lobes are significantly lower than those of the main lobe, that is, the SLL is reduced. Fig. 5.7 shows that, as predicted in [148], the more elements in the array, the greater the SLL reduction. For example, in the case of the 8-elements array, the SLL of the Fermat array is 0.9 dB, whereas for 64-elements array, it increases up to 6.9 dB. The observed disagreement between the theory and the fabricated arrays can be attributed to the limited manufacturing resolution and roughness. While for arrays with sizes larger than 36, it is most likely to be caused by the combined effects of the limited resolution in the positioning of the antenna in the SLM (spatial discretization of the phase mask) and the limited width of the illumination beam in SLM, which results in a reduced contribution of the elements in the periphery of the array to the total distant field. It is worth noting that an additional advantage of the aperiodic array is the flexibility to allow any number of antennas, not just perfect squares, as it is the case with periodic square arrays.

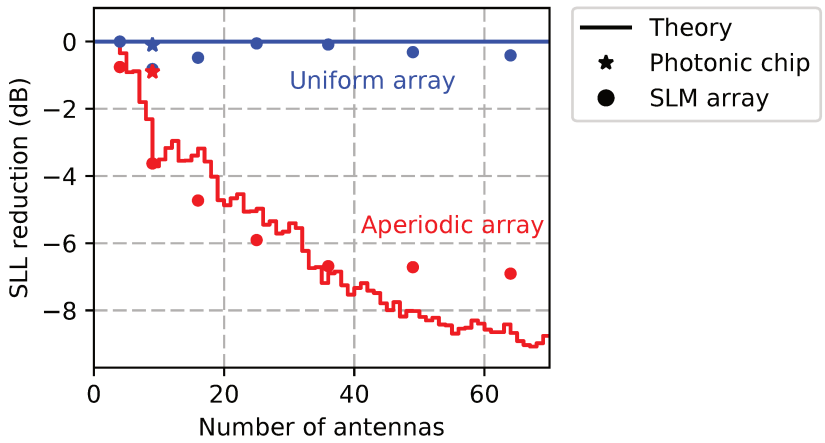

Figure 5.7: **SLL reduction for both periodic square arrays and Fermat's spiral with different numbers of antennas.** As predicted by theory, the SLL remains around 0 dB for the uniform arrays, being independent of the number of elements. In contrast, for the Fermat's spiral array, as the number of antennas increases, the SLL decreases. "Reprinted from [11]."

5.2 Conclusions

In this chapter we have shown that the arranging the elements according to the Fermat spiral the SLL of an optical array can be reduced. We achieved a SLL reduction of 0.9 dB for an array of 8 elements fabricated on SOI CMOS platform. We also confirmed the reduction of the SLL for arrays with a greater number of elements through SLM-based emulation, getting a reduction of up to 6.9 dB for 64 elements. Our results also show that the performance of the Fermat spiral array extends far beyond the usual spacings between antennas in sparse arrays. We demonstrate the reduction even for distances of 581 λ. The presented solution is, therefore, an attractive design to prevent the interference, security breaches and crosstalk caused by the presence of multiple radiation lobes with the same level of radiation from causing interference.

Chapter 6

Conclusions and future work

This thesis presents important contributions in the development of photonic antennas with counterintuitive designs. We show that topological optimization is a very useful tool for miniaturizing components and maximize integration in photonic chips. Our contribution is not limited to the design of high-performance compact novel devices, but we also contribute to the development of local knowledge regarding the manufacturing of SOI photonic antennas of complex designs with high fidelity and repeatability. These at-home manufacturing process drastically reduces the turn-around time for prototyping in comparison to third party commercial fabrication from more than a year down to less than a month. We also contribute to the development of photonic antenna characterization systems, since in our laboratories now it is possible to completely characterize both their near-field and the far-field radiated pattern, as well as their performance when used for coupling. In addition, we implement a high-performance parallel optimization environment in our cluster.

Regarding photonic antennas for coupling applications, we validated a design that reveals an unprecedented footprint of $49\,\mu m^2$. This represents an approximate reduction of 85 % with respect to conventional grating couplers. This antenna has a vertical coupling efficiency of $-6.3\,dB$ and a 3 dB bandwidth of approximately 60 nm. The reduced size of our antenna enables its use in multicore fibers and even in few-mode fibers. In addition, its full compatibility with the CMOS technology makes it a promising candidate for high-speed data communication links at data-center level. Even if we already have a good antenna prototype with reduced footprint for coupling applications, it is still necessary to improve its efficiency. It is also necessary a prototype that supports the two polarization states of the fundamental mode of the fiber. The experimental demonstration of a communications link between chips through a multi-core fiber is also left for future work.

In this work we also demonstrate a SOI ultra-compact photonic antenna designed with a broadside radiation pattern. We achieved the smallest footprint to date for a photonic antenna directly fed by a waveguide, as small as $1.78\,\mu m \times 1.78\,\mu m$ and with four different silicon layers. For a wavelengths range between 1470 nm and 1550 nm, numerical

simulations and experimental measurements show a practically wavelength-independent near-field profile (a deviation of only 4° in the main lobe of the far-field radiation pattern). The reduced size of the optimized antenna, together with an operating bandwidth of more than 100 nm, makes this design an ideal candidate for implementation in large-scale arrays.

Finally, we have demonstrated for the first time, the reduction of the SLL of 0.9 dB in an 8-element integrated array of by arranging its elements according to the Fermat spiral at NIR wavelengths. We also confirm the reduction of the SLL for arrays with a greater number, up to 64 elements, through a SLM-based emulation, getting a maximum SLL reduction of 6.9 dB. Our results show this arranging approach for SLL reduction is efficient beyond the common spacings in sparse arrays. We show the reduction even for a distance of 581 λ. The presented solution is, therefore, an attractive design to avoid multiple grating lobes that cause interference, security breaches and crosstalk in optical wireless communication systems. It would also be very interesting to experimentally demonstrate a large-scale integrated active array antenna (more than 256 elements) following Fermat's distribution since its SLL would be among the lowest reported in the literature to date.

Bibliography

[1] Cisco-VNI, "The Zettabyte Era: Trends and Analysis." https://www.cisco.com/c/en/us/solutions/collateral/service-provider/visual-networking-index-vni/vni-hyperconnectivity-wp.pdf, 2017. [Online; accessed 27-February-2018].

[2] P. Corcoran and A. Andrae, "Emerging trends in electricity consumption for consumer ict," *National University of Ireland, Galway, Connacht, Ireland, Tech. Rep*, 2013.

[3] R. Buyya, C. Vecchiola, and S. T. Selvi, *Mastering cloud computing: foundations and applications programming*. Newnes, 2013.

[4] F. M. Wanlass, "Low stand-by power complementary field effect circuitry," Dec. 5 1967. US Patent 3,356,858.

[5] N. A. Hatab, C.-H. Hsueh, A. L. Gaddis, S. T. Retterer, J.-H. Li, G. Eres, Z. Zhang, and B. Gu, "Free-standing optical gold bowtie nanoantenna with variable gap size for enhanced raman spectroscopy," *Nano Letters*, vol. 10, pp. 4952–4955, Dec. 2010.

[6] C. D'Andrea, J. Bochterle, A. Toma, C. Huck, F. Neubrech, E. Messina, B. Fazio, O. M. Maragò, E. D. Fabrizio, M. L. de La Chapelle, P. G. Gucciardi, and A. Pucci, "Optical nanoantennas for multiband surface-enhanced infrared and raman spectroscopy," *ACS Nano*, vol. 7, pp. 3522–3531, apr 2013.

[7] P. C. Wuytens, A. G. Skirtach, and R. Baets, "On-chip surface-enhanced raman spectroscopy using nanosphere-lithography patterned antennas on silicon nitride waveguides," *Opt. Express*, vol. 25, pp. 12926–12934, May 2017.

[8] H. Huang, H. Li, W. Li, A. Wu, X. Chen, X. Zhu, Z. Sheng, S. Zou, X. Wang, and F. Gan, "High-efficiency vertical light emission through a compact silicon nanoantenna array," *ACS Photonics*, vol. 3, pp. 324–328, mar 2016.

[9] A. Alù and N. Engheta, "Wireless at the nanoscale: Optical interconnects using matched nanoantennas," *Physical Review Letters*, vol. 104, p. 213902, may 2010.

[10] G. N. Malheiros-Silveira, G. S. Wiederhecker, and H. E. Hernández-Figueroa, "Dielectric resonator antenna for applications in nanophotonics," *Optics express*, vol. 21, no. 1, pp. 1234–1239, 2013.

[11] J. L. Pita, I. Aldaya, O. J. S. Santana, L. E. E. de Araujo, P. Dainese, and L. H. Gabrielli, "Side-lobe level reduction in bio-inspired optical phased-array antennas," *Opt. Express*, vol. 25, pp. 30105–30114, Nov 2017.

[12] S. Pillai, K. R. Catchpole, T. Trupke, and M. A. Green, "Surface plasmon enhanced silicon solar cells," *Journal of Applied Physics*, vol. 101, p. 093105, may 2007.

[13] K. R. Catchpole and A. Polman, "Plasmonic solar cells," *Optics Express*, vol. 16, p. 21793, dec 2008.

[14] N. Liu, M. Tang, M. Hentschel, H. Giessen, and A. P. Alivisatos, "Nanoantenna-enhanced gas sensing in a single tailored nanofocus," in *CLEO:2011 - Laser Applications to Photonic Applications*, p. PDPC11, Optical Society of America, OSA, 2011.

[15] J. C. Reed, H. Zhu, A. Y. Zhu, C. Li, and E. Cubukcu, "Graphene-enabled silver nanoantenna sensors," *Nano Letters*, vol. 12, pp. 4090–4094, aug 2012.

[16] J. Sun, E. Timurdogan, A. Yaacobi, E. S. Hosseini, and M. R. Watts, "Large-scale nanophotonic phased array," *Nature*, vol. 493, pp. 195–199, jan 2013.

[17] S. A. Miller, C. T. Phare, Y.-C. Chang, X. Ji, O. Jimenez, A. Mohanty, S. Roberts, M. C. Shin, B. Stern, M. Lipson, *et al.*, "512-element actively steered silicon phased array for low-power lidar," in *CLEO: Science and Innovations*, pp. JTh5C–2, Optical Society of America, 2018.

[18] J. J. López, S. A. Skirlo, D. Kharas, J. Sloan, J. Herd, P. Juodawlkis, M. Soljačić, and C. Sorace-Agaskar, "Planar-lens enabled beam steering for chip-scale lidar," in *CLEO: Science and Innovations*, pp. SM3I–1, Optical Society of America, 2018.

[19] C. V. Poulton, P. Russo, E. Timurdogan, M. Whitson, M. J. Byrd, E. Hosseini, B. Moss, Z. Su, D. Vermeulen, and M. R. Watts, "High-performance integrated optical phased arrays for chip-scale beam steering and lidar," in *CLEO: Applications and Technology*, pp. ATu3R–2, Optical Society of America, 2018.

[20] G. Marconi, "Wireless telegraphic communication," *Resonance*, vol. 7, no. 1, pp. 95–101, 2002.

[21] "Ieee standard definitions of terms for antennas," *IEEE Std 145-1983*, pp. 1–31, June 1983.

[22] C. A. Balanis, "Antenna theory: A review," *Proceedings of the IEEE*, vol. 80, no. 1, pp. 7–23, 1992.

[23] Á. C. Aznar, J. R. Robert, J. M. R. Casals, L. J. Roca, S. B. Boris, and M. F. Bataller, *Antenas*, vol. 3. Univ. Politèc. de Catalunya, 2004.

[24] H. Abediasl and H. Hashemi, "Monolithic optical phased-array transceiver in a standard SOI CMOS process," *Opt. Express*, vol. 23, no. 5, pp. 6509–6519, 2015.

[25] F. Aflatouni, B. Abiri, A. Rekhi, and A. Hajimiri, "Nanophotonic projection system," *Opt. Express*, vol. 23, no. 16, pp. 21012–21022, 2015.

[26] L. Vivien and L. Pavesi, *Handbook of silicon photonics*. Taylor & Francis, 2016.

[27] A. E. Krasnok, A. E. Miroshnichenko, P. A. Belov, and Y. S. Kivshar, "All-dielectric optical nanoantennas," *Optics Express*, vol. 20, p. 20599, aug 2012.

[28] T. Komljenovic, R. Helkey, L. Coldren, and J. E. Bowers, "Sparse aperiodic arrays for optical beam forming and lidar," *Opt. Express*, vol. 25, no. 3, pp. 2511–2528, 2017.

[29] M. J. R. Heck, "Highly integrated optical phased arrays: photonic integrated circuits for optical beam shaping and beam steering," *Nanophotonics*, vol. 6, no. 1, pp. 93–107, 2017.

[30] C. V. Poulton, M. J. Byrd, M. Raval, Z. Su, N. Li, E. Timurdogan, D. Coolbaugh, D. Vermeulen, and M. R. Watts, "Large-scale silicon nitride nanophotonic phased arrays at infrared and visible wavelengths," *Opt. Lett.*, vol. 42, no. 1, pp. 21–24, 2017.

[31] K. V. Acoleyen, W. Bogaerts, J. Jágerská, N. L. Thomas, R. Houdré, and R. Baets, "Off-chip beam steering with a one-dimensional optical phased array on silicon-on-insulator," *Opt. Lett.*, vol. 34, no. 9, pp. 1477–1479, 2009.

[32] J. K. Doylend, M. J. R. Heck, J. I. Bovington, J. D. Peters, L. A. Coldren, and J. E. Bowers, "Two-dimensional free-space beam steering with an optical phased array on silicon-on-insulator," *Opt. Express*, vol. 19, no. 22, pp. 21595–21604, 2011.

[33] D. Kwong, A. Hosseini, J. Covey, Y. Zhang, X. Xu, H. Subbaraman, and R. T. Chen, "On-chip silicon optical phased array for two-dimensional beam steering," *Opt. Lett.*, vol. 39, no. 4, pp. 941–944, 2014.

[34] A. Yaacobi, J. Sun, M. Moresco, G. Leake, D. Coolbaugh, and M. R. Watts, "Integrated phased array for wide-angle beam steering," *Opt. Lett.*, vol. 39, no. 15, pp. 4575–4578, 2014.

[35] K. V. Acoleyen, H. Rogier, and R. Baets, "Two-dimensional optical phased array antenna on silicon-on-insulator," *Opt. Express*, vol. 18, no. 13, pp. 13655–13660, 2010.

[36] J. Wessel, "Surface-enhanced optical microscopy," *JOSA B*, vol. 2, no. 9, pp. 1538–1541, 1985.

[37] E. Ozbay, "Plasmonics: merging photonics and electronics at nanoscale dimensions," *science*, vol. 311, no. 5758, pp. 189–193, 2006.

[38] P. Bharadwaj, B. Deutsch, and L. Novotny, "Optical antennas," *Adv. Opt. Photonics*, vol. 1, pp. 438–483, Nov 2009.

[39] A. Andryieuski, R. Malureanu, G. Biagi, T. Holmgaard, and A. Lavrinenko, "Compact dipole nanoantenna coupler to plasmonic slot waveguide," *Optics letters*, vol. 37, no. 6, pp. 1124–1126, 2012.

[40] A. Alu and N. Engheta, "Input impedance, nanocircuit loading, and radiation tuning of optical nanoantennas," *Physical review letters*, vol. 101, no. 4, p. 043901, 2008.

[41] J.-S. Huang, V. Callegari, P. Geisler, C. Brüning, J. Kern, J. C. Prangsma, X. Wu, T. Feichtner, J. Ziegler, P. Weinmann, *et al.*, "Atomically flat single-crystalline gold nanostructures for plasmonic nanocircuitry," *Nature communications*, vol. 1, p. 150, 2010.

[42] P. Schuck, D. Fromm, A. Sundaramurthy, G. Kino, and W. Moerner, "Improving the mismatch between light and nanoscale objects with gold bowtie nanoantennas," *Physical review letters*, vol. 94, no. 1, p. 017402, 2005.

[43] A. Berrier, R. Ulbricht, M. Bonn, and J. G. Rivas, "Ultrafast active control of localized surface plasmon resonances in silicon bowtie antennas," *Optics express*, vol. 18, no. 22, pp. 23226–23235, 2010.

[44] S. Sederberg and A. Elezzabi, "Nanoscale plasmonic contour bowtie antenna operating in the mid-infrared," *Optics Express*, vol. 19, no. 16, pp. 15532–15537, 2011.

[45] T. Kosako, Y. Kadoya, and H. F. Hofmann, "Directional control of light by a nano-optical yagi–uda antenna," *Nature Photonics*, vol. 4, no. 5, p. 312, 2010.

[46] D. Dregely, R. Taubert, J. Dorfmüller, R. Vogelgesang, K. Kern, and H. Giessen, "3D optical Yagi-Uda nanoantenna array," *Nat. Commun.*, vol. 2, p. 267, 2011.

[47] T. Coenen, E. J. R. Vesseur, A. Polman, and A. F. Koenderink, "Directional emission from plasmonic yagi–uda antennas probed by angle-resolved cathodoluminescence spectroscopy," *Nano letters*, vol. 11, no. 9, pp. 3779–3784, 2011.

[48] G. N. Malheiros-Silveira, L. H. Gabrielli, C. J. Chang-Hasnain, and H. E. Hernandez-Figueroa, "Breakthroughs in photonics 2013: Advances in nanoantennas," *IEEE Photonics Journal*, vol. 6, pp. 1–6, apr 2014.

[49] A. B. Evlyukhin, S. M. Novikov, U. Zywietz, R. L. Eriksen, C. Reinhardt, S. I. Bozhevolnyi, and B. N. Chichkov, "Demonstration of magnetic dipole resonances of dielectric nanospheres in the visible region," *Nano letters*, vol. 12, no. 7, pp. 3749–3755, 2012.

[50] S. Kumar *et al.*, "Nanoantenna–a review on present and future perspective," 2016.

[51] J. Sun, P. S. Carney, and J. C. Schotland, "Strong tip effects in near-field scanning optical tomography," *Journal of Applied Physics*, vol. 102, no. 10, p. 103103, 2007.

[52] C. Höppener and L. Novotny, "Imaging of membrane proteins using antenna-based optical microscopy," *Nanotechnology*, vol. 19, no. 38, p. 384012, 2008.

[53] D. P. Fromm, A. Sundaramurthy, A. Kinkhabwala, P. J. Schuck, G. S. Kino, and W. Moerner, "Exploring the chemical enhancement for surface-enhanced raman scattering with au bowtie nanoantennas," 2006.

[54] A. Sundaramurthy, P. J. Schuck, N. R. Conley, D. P. Fromm, G. S. Kino, and W. Moerner, "Toward nanometer-scale optical photolithography: utilizing the near-field of bowtie optical nanoantennas," *Nano letters*, vol. 6, no. 3, pp. 355–360, 2006.

[55] P. Biagioni, J.-S. Huang, and B. Hecht, "Nanoantennas for visible and infrared radiation," *Reports on Progress in Physics*, vol. 75, no. 2, p. 024402, 2012.

[56] M. Kirkengen, J. Bergli, and Y. M. Galperin, "Direct generation of charge carriers in c-si solar cells due to embedded nanoparticles," *Journal of Applied Physics*, vol. 102, no. 9, p. 093713, 2007.

[57] P. M. Voroshilov, V. Ovchinnikov, A. Papadimitratos, A. A. Zakhidov, and C. R. Simovski, "Light trapping enhancement by silver nanoantennas in organic solar cells," *ACS Photonics*, vol. 5, no. 5, pp. 1767–1772, 2018.

[58] J. Homola, S. S. Yee, and G. Gauglitz, "Surface plasmon resonance sensors," *Sensors and Actuators B: Chemical*, vol. 54, no. 1-2, pp. 3–15, 1999.

[59] M. Mesch, C. Zhang, P. V. Braun, and H. Giessen, "Functionalized hydrogel on plasmonic nanoantennas for noninvasive glucose sensing," *Acs Photonics*, vol. 2, no. 4, pp. 475–480, 2015.

[60] C. V. Poulton, A. Yaacobi, D. B. Cole, M. J. Byrd, M. Raval, D. Vermeulen, and M. R. Watts, "Coherent solid-state lidar with silicon photonic optical phased arrays," *Optics letters*, vol. 42, no. 20, pp. 4091–4094, 2017.

[61] S. Malhouitre, D. Fowler, S. Garcia, O. Lemonnier, N. Tyler, and W. Rabaud, "Silicon nitride photonic platform for lidar applications," in *2018 IEEE 15th International Conference on Group IV Photonics (GFP)*, pp. 1–2, IEEE, 2018.

[62] A. Michaels and E. Yablonovitch, "Reinventing the circuit board with integrated optical interconnects," in *Conference on Lasers and Electro-Optics*, pp. STu4G–2, Optical Society of America, OSA, 2016.

[63] Z. Yang, N. Fang, A. Wu, J. Chen, M. Zhang, X. Wang, and S. Zou, "Fabrication and characterization of integrated three-dimensional linear taper on silicon-on-insulator," *Optical Engineering*, vol. 48, no. 3, p. 030503, 2009.

[64] V. Nguyen, T. Montalbo, C. Manolatou, A. Agarwal, C.-y. Hong, J. Yasaitis, L. Kimerling, and J. Michel, "Silicon-based highly-efficient fiber-to-waveguide coupler for high index contrast systems," *Applied physics letters*, vol. 88, no. 8, p. 081112, 2006.

[65] J. Doylend and A. Knights, "Design and simulation of an integrated fiber-to-chip coupler for silicon-on-insulator waveguides," *IEEE Journal of Selected Topics in Quantum Electronics*, vol. 12, no. 6, pp. 1363–1370, 2006.

[66] N. Fang, Z. Yang, A. Wu, J. Chen, M. Zhang, S. Zou, and X. Wang, "Three-dimensional tapered spot-size converter based on (111) silicon-on-insulator," *IEEE Photonics Technology Letters*, vol. 21, no. 12, pp. 820–822, 2009.

[67] A. Sure, T. Dillon, J. Murakowski, C. Lin, D. Pustai, and D. W. Prather, "Fabrication and characterization of three-dimensional silicon tapers," *Optics express*, vol. 11, no. 26, pp. 3555–3561, 2003.

[68] K. Kasaya, O. Mitomi, M. Naganuma, Y. Kondo, and Y. Noguchi, "A simple laterally tapered waveguide for low-loss coupling to single-mode fibers," *IEEE Photonics Technology Letters*, vol. 5, no. 3, pp. 345–347, 1993.

[69] O. Mitomi, K. Kasaya, and H. Miyazawa, "Design of a single-mode tapered waveguide for low-loss chip-to-fiber coupling," *IEEE Journal of Quantum Electronics*, vol. 30, no. 8, pp. 1787–1793, 1994.

[70] R. Takei, M. Suzuki, E. Omoda, S. Manako, T. Kamei, M. Mori, and Y. Sakakibara, "Silicon knife-edge taper waveguide for ultralow-loss spot-size converter fabricated by photolithography," *Applied Physics Letters*, vol. 102, no. 10, p. 101108, 2013.

[71] M. Pu, L. Liu, H. Ou, K. Yvind, and J. M. Hvam, "Ultra-low-loss inverted taper coupler for silicon-on-insulator ridge waveguide," *Optics Communications*, vol. 283, no. 19, pp. 3678–3682, 2010.

[72] G. Roelkens, P. Dumon, W. Bogaerts, D. Van Thourhout, and R. Baets, "Efficient silicon-on-insulator fiber coupler fabricated using 248-nm-deep uv lithography," *IEEE Photonics Technology Letters*, vol. 17, no. 12, pp. 2613–2615, 2005.

[73] J. Cardenas, C. B. Poitras, K. Luke, L.-W. Luo, P. A. Morton, and M. Lipson, "High coupling efficiency etched facet tapers in silicon waveguides," *IEEE Photon. Technol. Lett.*, vol. 26, no. 23, pp. 2380–2382, 2014.

[74] V. R. Almeida, R. R. Panepucci, and M. Lipson, "Nanotaper for compact mode conversion," *Optics letters*, vol. 28, no. 15, pp. 1302–1304, 2003.

[75] A. Khilo, M. A. Popović, M. Araghchini, and F. X. Kärtner, "Efficient planar fiber-to-chip coupler based on two-stage adiabatic evolution," *Optics express*, vol. 18, no. 15, pp. 15790–15806, 2010.

[76] L. Chrostowski and M. Hochberg, *Silicon Photonics Design*. Cambridge University Press, 2015.

[77] L. Vivien, D. Pascal, S. Lardenois, D. Marris-Morini, E. Cassan, F. Grillot, S. Laval, J.-M. Fédéli, and L. El Melhaoui, "Light injection in soi microwaveguides using high-efficiency grating couplers," *Journal of Lightwave technology*, vol. 24, no. 10, pp. 3810–3815, 2006.

[78] K. Van Acoleyen and R. Baets, "Compact lens-assisted focusing tapers fabricated on silicon-on-insulator," in *Group IV Photonics (GFP), 2011 8th IEEE International Conference on*, pp. 157–159, IEEE, 2011.

[79] L. H. Gabrielli and M. Lipson, "Integrated luneburg lens via ultra-strong index gradient on silicon," *Optics express*, vol. 19, no. 21, pp. 20122–20127, 2011.

[80] R. Wagner and W. Tomlinson, "Coupling efficiency of optics in single-mode fiber components," *Applied optics*, vol. 21, no. 15, pp. 2671–2688, 1982.

[81] D. Taillaert, W. Bogaerts, and R. Baets, "Efficient coupling between submicron soi-waveguides and single-mode fibers," in *Proceedings of Symposium IEEE/LEOS Benelux Chapter*, pp. 289–292, 2003.

[82] R. Halir, A. Ortega-Monux, J. H. Schmid, C. Alonso-Ramos, J. Lapointe, D.-X. Xu, J. G. Wanguemert-Perez, I. Molina-Fernandez, and S. Janz, "Recent advances in silicon waveguide devices using sub-wavelength gratings," *Selected Topics in Quantum Electronics, IEEE Journal of*, vol. 20, no. 4, pp. 279–291, 2014.

[83] G. Maire, L. Vivien, G. Sattler, A. Kazmierczak, B. Sanchez, K. B. Gylfason, A. Griol, D. Marris-Morini, E. Cassan, D. Giannone, *et al.*, "High efficiency silicon nitride surface grating couplers," *Optics express*, vol. 16, no. 1, pp. 328–333, 2008.

[84] S. Romero-García, F. Merget, F. Zhong, H. Finkelstein, and J. Witzens, "Silicon nitride cmos-compatible platform for integrated photonics applications at visible wavelengths," *Optics express*, vol. 21, no. 12, pp. 14036–14046, 2013.

[85] A. Z. Subramanian, S. Selvaraja, P. Verheyen, A. Dhakal, K. Komorowska, and R. Baets, "Near-infrared grating couplers for silicon nitride photonic wires," *Photonics Technology Letters, IEEE*, vol. 24, no. 19, pp. 1700–1703, 2012.

[86] L. Wang, Y. Li, M. G. Porcel, D. Vermeulen, X. Han, J. Wang, X. Jian, M. Zhao, and G. Morthier, "Grating couplers in polymer with a thin si3n4 layer embedded," in *SPIE OPTO*, pp. 825817–825817, International Society for Optics and Photonics, 2012.

[87] R. Waldhäusl, B. Schnabel, E.-B. Kley, and A. Bräuer, "Efficient focusing polymer waveguide grating couplers," *Electronics letters*, vol. 33, no. 7, pp. 623–624, 1997.

[88] Z. Yu, X. Xue-Jun, L. Zhi-Yong, Z. Liang, H. Wei-Hua, F. Zhong-Chao, Y. Yu-De, and Y. Jin-Zhong, "High efficiency and broad bandwidth grating coupler between nanophotonic waveguide and fibre," *Chinese Physics B*, vol. 19, no. 1, p. 5, 2010.

[89] J. Bolten, J. Hofrichter, N. Moll, S. Schönenberger, F. Horst, B. J. Offrein, T. Wahlbrink, T. Mollenhauer, and H. Kurz, "Cmos compatible cost-efficient fabrication of soi grating couplers," *Microelectronic Engineering*, vol. 86, no. 4, pp. 1114–1116, 2009.

[90] F. Van Laere, G. Roelkens, M. Ayre, J. Schrauwen, D. Taillaert, D. Van Thourhout, T. F. Krauss, and R. Baets, "Compact and highly efficient grating couplers between optical fiber and nanophotonic waveguides," *Journal of Lightwave Technology*, vol. 25, no. 1, pp. 151–156, 2007.

[91] S. K. Selvaraja, D. Vermeulen, M. Schaekers, E. Sleeckx, W. Bogaerts, G. Roelkens, P. Dumon, D. Van Thourhout, and R. Baets, "Highly efficient grating coupler between optical fiber and silicon photonic circuit," in *Conference on Lasers and Electro-Optics*, p. CTuC6, Optical Society of America, 2009.

[92] D. Vermeulen, S. Selvaraja, P. Verheyen, G. Lepage, W. Bogaerts, and G. Roelkens, "High-efficiency silicon-on-insulator fiber-to-chip grating couplers using a silicon overlay," in *6th IEEE International Conference on Group IV Photonics*, 2009.

[93] T. K. Saha and W. Zhou, "High efficiency diffractive grating coupler based on transferred silicon nanomembrane overlay on photonic waveguide," *Journal of Physics D: Applied Physics*, vol. 42, no. 8, p. 085115, 2009.

[94] X. Chen, C. Li, C. K. Fung, S. M. Lo, and H. K. Tsang, "Apodized waveguide grating couplers for efficient coupling to optical fibers," *Photonics Technology Letters, IEEE*, vol. 22, no. 15, pp. 1156–1158, 2010.

[95] A. Mekis, S. Gloeckner, G. Masini, A. Narasimha, T. Pinguet, S. Sahni, and P. De Dobbelaere, "A grating-coupler-enabled cmos photonics platform," *Selected Topics in Quantum Electronics, IEEE Journal of*, vol. 17, no. 3, pp. 597–608, 2011.

[96] Z. Can, S. Jing-Hua, X. Xi, S. Wei-Min, Z. Xiao-Jun, C. Tao, Y. Jin-Zhong, and Y. Yu-De, "High efficiency grating coupler for coupling between single-mode fiber and soi waveguides," *Chinese Physics Letters*, vol. 30, no. 1, p. 014207, 2013.

[97] Y. Wang, W. Shi, X. Wang, Z. Lu, M. Caverley, R. Bojko, L. Chrostowski, and N. A. Jaeger, "Design of broadband subwavelength grating couplers with low back reflection," *Optics letters*, vol. 40, no. 20, pp. 4647–4650, 2015.

[98] Y. Wang, X. Wang, J. Flueckiger, H. Yun, W. Shi, R. Bojko, N. A. Jaeger, and L. Chrostowski, "Focusing sub-wavelength grating couplers with low back reflections for rapid prototyping of silicon photonic circuits," *Optics express*, vol. 22, no. 17, pp. 20652–20662, 2014.

[99] P. Sethi, A. Haldar, and S. K. Selvaraja, "Ultra-compact low-loss broadband waveguide taper in silicon-on-insulator," *Optics Express*, vol. 25, no. 9, pp. 10196–10203, 2017.

[100] S. Scheerlinck, D. Taillaert, D. Van Thourhout, and R. Baets, "Flexible metal grating based optical fiber probe for photonic integrated circuits," *Applied Physics Letters*, vol. 92, no. 3, p. 031104, 2008.

[101] C. Grillet, C. Smith, D. Freeman, S. Madden, B. Luther-Davies, E. C. Magi, D. J. Moss, and B. J. Eggleton, "Efficient coupling to chalcogenide glass photonic crystal waveguides via silica optical fiber nanowires," *Optics Express*, vol. 14, no. 3, pp. 1070–1078, 2006.

[102] P. Dumon, W. Bogaerts, D. V. Thourhout, D. Taillaert, R. Baets, J. Wouters, S. Beckx, and P. Jaenen, "Compact wavelength router based on a silicon-on-insulator

arrayed waveguide grating pigtailed to a fiber array," *Optics Express*, vol. 14, no. 2, p. 664, 2006.

[103] B. J. Puttnam, R. S. Luís, W. Klaus, J. Sakaguchi, J. M. D. Mendinueta, Y. Awaji, N. Wada, Y. Tamura, T. Hayashi, M. Hirano, and J. Marciante, "2.15 pb/s transmission using a 22 core homogeneous single-mode multi-core fiber and wideband optical comb," in *Optical Communication (ECOC), 2015 European Conference on*, pp. 1–3, Sept 2015.

[104] R. J. Mailloux, *Phased array antenna handbook*, vol. 2. Artech House Boston, 2005.

[105] T. Yoshida, E. Omoda, Y. Atsumi, T. Nishi, S. Tajima, N. Miura, M. Mori, and Y. Sakakibara, "Vertically curved Si waveguide coupler with low loss and flat wavelength window," *Journal of Lightwave Technology*, vol. 34, pp. 1567–1571, apr 2016.

[106] R. Fatemi, A. Khachaturian, and A. Hajimiri, "Scalable optical phased array with sparse 2d aperture," in *CLEO: Science and Innovations*, pp. STu4B–6, Optical Society of America, 2018.

[107] S. Chung, H. Abediasl, and H. Hashemi, "15.4 a 1024-element scalable optical phased array in 0.18 μm soi cmos," in *Solid-State Circuits Conference (ISSCC), 2017 IEEE International*, pp. 262–263, IEEE, 2017.

[108] D. N. Hutchison, J. Sun, J. K. Doylend, R. Kumar, J. Heck, W. Kim, C. T. Phare, A. Feshali, and H. Rong, "High-resolution aliasing-free optical beam steering," *Optica*, vol. 3, no. 8, pp. 887–890, 2016.

[109] J. Notaros, N. Li, C. V. Poulton, Z. Su, M. J. Byrd, E. S. Magden, and M. R. Watts, "Cmos-compatible optical phased arrays with monolithically-integrated erbium lasers," in *CLEO: Science and Innovations*, pp. STu4B–2, Optical Society of America, 2018.

[110] C. T. Phare, M. C. Shin, S. A. Miller, B. Stern, and M. Lipson, "Silicon optical phased array with high-efficiency beam formation over 180 degree field of view," *arXiv preprint arXiv:1802.04624*, 2018.

[111] "Soitec, inc.." https://www.soitec.com/en/products/photonics-soi. 2018-03-06.

[112] "gdspy's documentation." http://gdspy.readthedocs.io/en/latest/. 2018-03-06.

[113] N. Posseme, *Plasma Etching Processes for Cmos Devices Realization*. Elsevier, 2017.

[114] P. Harvey-Collard, A. Jaouad, D. Drouin, and M. Pioro-Ladrière, "Inductively coupled plasma etching of amorphous silicon nanostructures over nanotopography using c4f8/sf6 chemistry," *Microelectronic Engineering*, vol. 110, pp. 408–413, 2013.

[115] M. D. Henry, *ICP etching of silicon for micro and nanoscale devices*. California Institute of Technology, 2010.

[116] F. Saffih, C. Con, A. Alshammari, M. Yavuz, and B. Cui, "Fabrication of silicon nanostructures with large taper angle by reactive ion etching," *Journal of Vacuum Science & Technology B, Nanotechnology and Microelectronics: Materials, Processing, Measurement, and Phenomena*, vol. 32, no. 6, p. 06FI04, 2014.

[117] H. Rhee, H. Kwon, C.-K. Kim, H. Kim, J. Yoo, and Y. W. Kim, "Comparison of deep silicon etching using sf 6/c 4 f 8 and sf 6/c 4 f 6 plasmas in the bosch process," *Journal of Vacuum Science & Technology B: Microelectronics and Nanometer Structures Processing, Measurement, and Phenomena*, vol. 26, no. 2, pp. 576–581, 2008.

[118] J. A. Kurvits, M. Jiang, and R. Zia, "Comparative analysis of imaging configurations and objectives for fourier microscopy," *JOSA A*, vol. 32, no. 11, pp. 2082–2092, 2015.

[119] A. Y. Piggott, J. Lu, K. G. Lagoudakis, J. Petykiewicz, T. M. Babinec, and J. Vučković, "Inverse design and demonstration of a compact and broadband on-chip wavelength demultiplexer," *Nature Photonics*, vol. 9, no. 6, pp. 374–377, 2015.

[120] B. Shen, P. Wang, R. Polson, and R. Menon, "An integrated-nanophotonics polarization beamsplitter with 2.4× 2.4 μm2 footprint," *Nature Photonics*, vol. 9, no. 6, pp. 378–382, 2015.

[121] P. I. Borel, A. Harpøth, L. H. Frandsen, M. Kristensen, P. Shi, J. S. Jensen, and O. Sigmund, "Topology optimization and fabrication of photonic crystal structures," *Optics Express*, vol. 12, no. 9, pp. 1996–2001, 2004.

[122] A. Y. Piggott, J. Lu, T. M. Babinec, K. G. Lagoudakis, J. Petykiewicz, and J. Vučković, "Inverse design and implementation of a wavelength demultiplexing grating coupler," *Scientific reports*, vol. 4, 2014.

[123] L. H. Frandsen, Y. Elesin, L. F. Frellsen, M. Mitrovic, Y. Ding, O. Sigmund, and K. Yvind, "Topology optimized mode conversion in a photonic crystal waveguide fabricated in silicon-on-insulator material," *Optics express*, vol. 22, no. 7, pp. 8525–8532, 2014.

[124] B. Shen, P. Wang, R. Polson, and R. Menon, "Ultra-high-efficiency metamaterial polarizer," *Optica*, vol. 1, no. 5, pp. 356–360, 2014.

[125] O. Sigmund, J. S. Jensen, and L. H. Frandsen, "On nanostructured silicon success," *Nature Photonics*, vol. 10, no. 3, p. 142, 2016.

[126] Y. ELI, "In the limelight," 2012.

[127] G. Allaire, "A review of adjoint methods for sensitivity analysis, uncertainty quantification and optimization in numerical codes," *Ingénieurs de l'Automobile*, vol. 836, pp. 33–36, 2015.

[128] P. E. Gill, W. Murray, and M. A. Saunders, "SNOPT: An SQP algorithm for large-scale constrained optimization," *SIAM Review*, vol. 47, pp. 99–131, jan 2005.

[129] P. E. Gill, W. Murray, and M. A. Saunders, "User's guide for sqopt version 7: Software for large-scale linear and quadratic programming," 2008.

[130] O. Module, "Users guide, comsol 4.3 b (2013)."

[131] R. Storn and K. Price, "Differential evolution–a simple and efficient heuristic for global optimization over continuous spaces," *Journal of global optimization*, vol. 11, no. 4, pp. 341–359, 1997.

[132] U. K. Chakraborty, *Advances in differential evolution*, vol. 143. Springer, 2008.

[133] Z. Yang, K. Tang, and X. Yao, "Self-adaptive differential evolution with neighborhood search," in *Evolutionary Computation, 2008. CEC 2008.(IEEE World Congress on Computational Intelligence). IEEE Congress on*, pp. 1110–1116, IEEE, 2008.

[134] Z. Zhang, Y. Tsuji, T. Yasui, and K. Hirayama, "Design of ultra-compact triplexer with function-expansion based topology optimization," *Optics Express*, vol. 23, no. 4, pp. 3937–3950, 2015.

[135] E. Hassan, E. Wadbro, and M. Berggren, "Topology optimization of metallic antennas," *IEEE Transactions on Antennas and Propagation*, vol. 62, no. 5, pp. 2488–2500, 2014.

[136] R. Díaz de León-Zapata, G. González, E. Flores-García, A. G. Rodríguez, and F. J. González, "Evolutionary algorithm geometry optimization of optical antennas," *International Journal of Antennas and Propagation*, vol. 2016, 2016.

[137] J. L. Pita, I. Aldaya, P. Dainese, H. E. Hernandez-Figueroa, and L. H. Gabrielli, "Design of a compact cmos-compatible photonic antenna by topological optimization," *Optics express*, vol. 26, no. 3, pp. 2435–2442, 2018.

[138] J. Sun, E. S. Hosseini, A. Yaacobi, D. B. Cole, G. Leake, D. Coolbaugh, and M. R. Watts, "Two-dimensional apodized silicon photonic phased arrays," *Opt. Lett.*, vol. 39, no. 2, pp. 367–370, 2014.

[139] M. G. Bray, D. H. Werner, D. W. Boeringer, and D. W. Machuga, "Optimization of thinned aperiodic linear phased arrays using genetic algorithms to reduce grating

lobes during scanning," *IEEE T. Antenn. Propag.*, vol. 50, no. 12, pp. 1732–1742, 2002.

[140] J. S. Petko and D. H. Werner, "The evolution of optimal linear polyfractal arrays using genetic algorithms," *IEEE T. Antenn. Propag.*, vol. 53, no. 11, pp. 3604–3615, 2005.

[141] M. A. Panduro, A. L. Mendez, R. Dominguez, and G. Romero, "Design of non-uniform circular antenna arrays for side lobe reduction using the method of genetic algorithms," *AEU-INT J. Electron. C.*, vol. 60, no. 10, pp. 713–717, 2006.

[142] M. M. Khodier and C. G. Christodoulou, "Linear array geometry synthesis with minimum sidelobe level and null control using particle swarm optimization," *IEEE T. Antenn. Propag.*, vol. 53, no. 8, pp. 2674–2679, 2005.

[143] S. K. Goudos, V. Moysiadou, T. Samaras, K. Siakavara, and J. N. Sahalos, "Application of a comprehensive learning particle swarm optimizer to unequally spaced linear array synthesis with sidelobe level suppression and null control," *IEEE Antenn. Wirel. Pr.*, vol. 9, pp. 125–129, 2010.

[144] T. G. Spence and D. H. Werner, "Design of broadband planar arrays based on the optimization of aperiodic tilings," *IEEE T. Antenn. Propag.*, vol. 56, no. 1, pp. 76–86, 2008.

[145] M. D. Gregory, J. S. Petko, T. G. Spence, and D. H. Werner, "Nature-inspired design techniques for ultra-wideband aperiodic antenna arrays," *IEEE Antenn. Propag. M.*, vol. 52, no. 3, pp. 28–45, 2010.

[146] D. W. Boeringer, "Phased array including a logarithmic spiral lattice of uniformly spaced radiating and receiving elements," 2002. US Patent 6,433,754.

[147] M. C. Viganó, G. Toso, G. Caille, C. Mangenot, and I. E. Lager, "Sunflower array antenna with adjustable density taper," *Int. J. Antenn. Propag.*, vol. 2009, pp. 1–10, 2009.

[148] L. H. Gabrielli and H. E. Hernandez-Figueroa, "Aperiodic antenna array for secondary lobe suppression," *IEEE Photonic Tech. L.*, vol. 28, no. 2, pp. 209–212, 2016.

[149] J. N. Ridley, "Packing efficiency in sunflower heads," *Math. Biosci.*, vol. 58, no. 1, pp. 129–139, 1982.

[150] M. W. Niaz, Z. Ahmed, and M. B. Ihsan, "Reflectarray with logarithmic spiral lattice of elementary antennas on its aperture," *AEU-Int. J. Electron.F C*, vol. 70, no. 8, pp. 1050–1054, 2016.

[151] J. L. Pita, P. C. Dainese, H. E. Hernandez-Figueroa, and L. H. Gabrielli, "Ultra-compact broadband dielectric antenna," in *CLEO: Science and Innovations*, pp. SM3G–7, Optical Society of America, 2016.

[152] W. H. Bragg and W. L. Bragg, "The reflection of x-rays by crystals," *Proceedings of the Royal Society of London A: Mathematical, Physical and Engineering Sciences*, vol. 88, no. 605, pp. 428–438, 1913.

[153] H. Meyers and H. Myers, *Introductory solid state physics*. CRC press, 1997.

[154] X. Chen and H. K. Tsang, "Polarization-independent grating couplers for silicon-on-insulator nanophotonic waveguides," *Optics letters*, vol. 36, no. 6, pp. 796–798, 2011.

[155] A. Michaels and E. Yablonovitch, "Gradient-based inverse electromagnetic design using continuously-smoothed boundaries," *arXiv preprint arXiv:1705.07188*, 2017.

[156] C.-L. Chen, *Foundations for guided-wave optics*. John Wiley & Sons, 2006.

Appendix A

In-house polishing recipe

1. Materials for the polishing process at LCO.

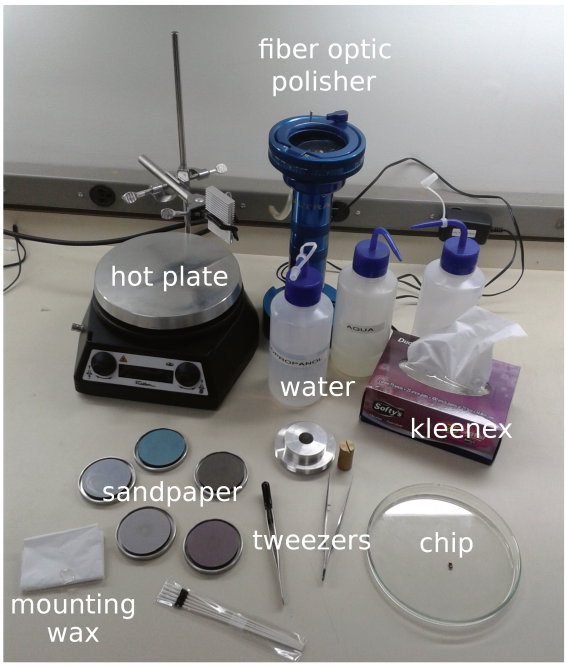

Figure A.1: **Materials used to polish.** Fiber optics polisher, hotplate, sandpaper, metal mounting piece, mounting wax, tweezers, kleenex, water, acetone, and the chip.

2. Sticking the chip:

   (a) Cover the chip with e-resist.

   (b) Heat the metal mounting piece up to 120 °C with the hotplate.

   (c) Use a little portion of the mounting wax on the metallic piece and glue the chip as indicated in Fig. A.2.

   (d) Turn off the hotplate, remove the metallic piece and check the chip orientation in the microscope to ensure a good polish.

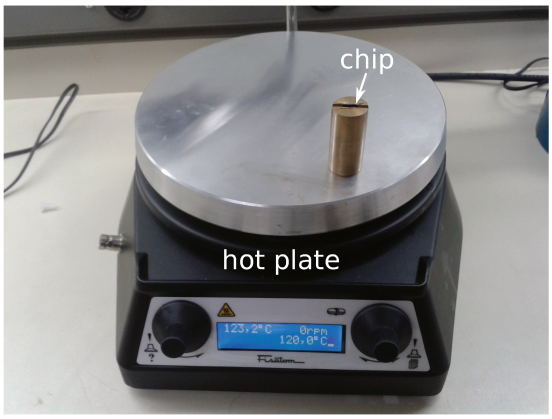

Figure A.2: **Metal piece with the fixed chip on the hotplate.**

3. Polishing:

   (a) Remove the e-resist at chip edge as illustrated in Fig. A.3.

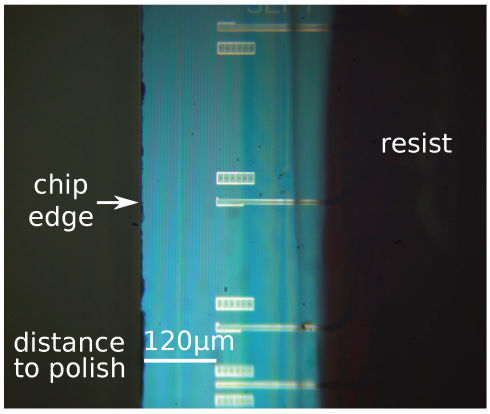

Figure A.3: **Chip ready to start the polishing process.** The distance to be polished is approximately 120 µm.

   (b) Select the appropriate sandpaper to begin polish according the table A.1.

   (c) Put a few drops of water over the polishing disk (see Fig. A.4).

   (d) Put the metallic piece with the chip in the polisher and start the polishing process.

   (e) Observe each step in the microscope.

   (f) Continue with the process to arrive at devices as presented in Fig. A.5.

4. Chip unsticking:

   (a) Set the hotplate at 120 °C and remove the chip with the tweezers.

   (b) Clean the chip with acetone (5 min), isopropanol (3 min) and dry it with nitrogen.

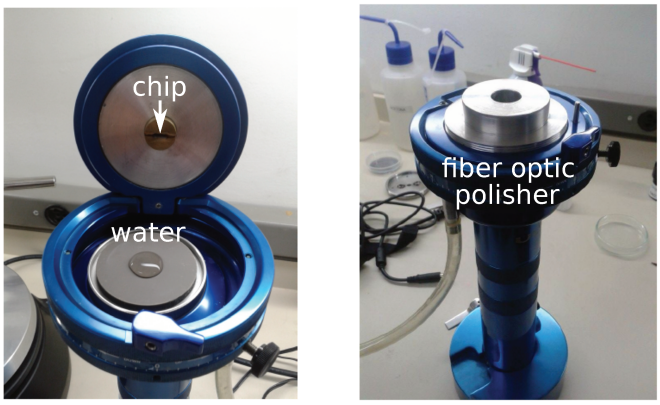

Figure A.4: **Fiber optics polisher adapted to polish chips.**

(c) Organize all the used material.

(d) Enjoy and have fun with the polished chip.

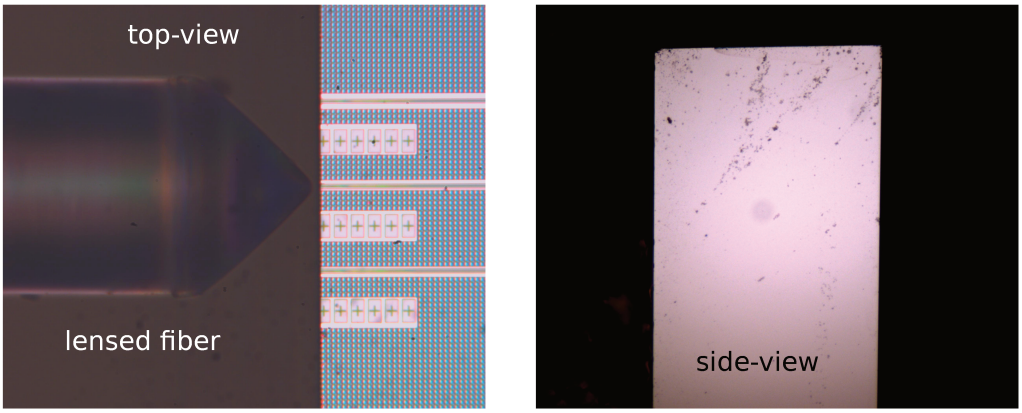

Figure A.5: **Chip after the polishing process.**

Next, we summarize a polishing recipe for chips fabricated at imec/Europractice.

Table A.1: Polishing recipe.

Distance to polish (µm)	Time (min)	Disk resolution (µm)
105	6	6
39	3	3
18	5	1
1	6	<1

Appendix B

Grating design

To understand the design of a grating coupler we must first understand Bragg's law. It was first proposed by Lawrence Bragg and his father William Henry Bragg in 1913 [152], in response to his discovery that crystalline solids produced striking X-ray reflection patterns in contrast to, for example, reflection from a liquid. They discovered that these crystals, at certain specific wavelengths and angles of incidence, produced intense peaks of reflected radiation. Although simple, Bragg's law confirmed the existence of real particles at the atomic scale in addition to providing a powerful new tool for the study of crystals in the form of X rays and neutron diffraction. Lawrence Bragg and his father, William Henry Bragg, received the Nobel Prize in physics in 1915 for their studies in the analysis of crystalline structures by means of X rays and by the important breakthrough in the development of X-ray crystallography. They are the only team of father and son to win the Nobel prize together. Furthermore, Lawrence Bragg was 25 years old, which made him the youngest winner of the Nobel Prize in Physics.

The Bragg's demonstrated that X-ray diffraction in solids can be explained if we consider them as crystals, which act as three-dimensional diffraction gratings. When the incident wave arrives, each atom acts as a scattering center and produces a wave that interferes with the waves that scatter from the other atoms. When the emitted waves interfere constructively, they remain in phase since the difference between the path lengths of the two waves is equal to an integer number (n) of wavelengths (λ). The path difference between two waves experiencing interference is given by $2d \cdot \sin\theta$, where d is the interplanar distance, as shown in Fig. B.1. This leads to Bragg's law, which describes the condition of θ so that the constructive interference is maximum [153]:

$$2d \cdot \sin\theta = n\lambda, \tag{B.1}$$

The grating couplers are periodic structures in one direction, and can be designed based on the Bragg law. The incident wave on the grating is a wave that propagates in a waveguide, with the direction of propagation in the same plane as the grating and normal

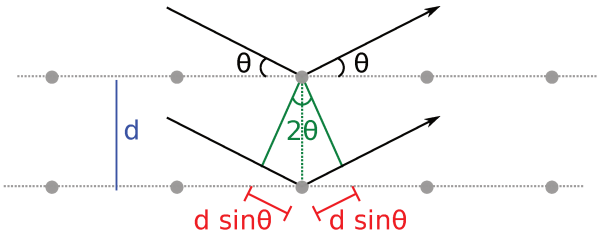

Figure B.1: **Bragg diffraction scheme.** Two beams with identical wavelength and phase approach a crystalline solid and are scattered by two different atoms. Constructive interference occurs when this length is equal to an integer number of the wavelength of the radiation. "Reprinted from [76]".

to the grating teeth. The propagation constant of the waveguide is $\beta = 2\pi n_{eff}/\lambda_0$, where λ_0 is the wavelength, and n_{eff} is the effective index of the waveguide.

The moment conservation in the z direction dictates that $k_z = \beta + mK$ with (m = 0, ± 1, ± 2, ...) [26], where k_z is the wave vector of the diffracted wave in the direction of the incident wave as can be seen in Fig. B.2. The diffracted wave has in the cladding an effective index of n_{cld}, therefore it has a wave vector $k = 2\pi n_{cld}/\lambda_0$.

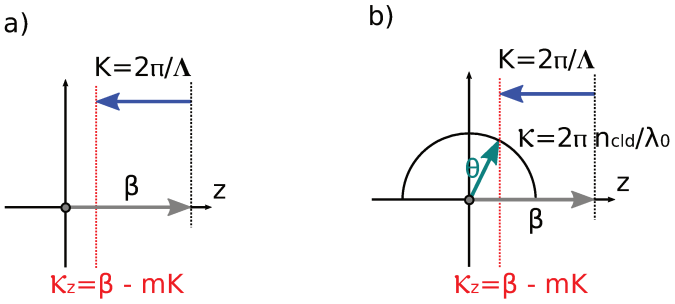

Figure B.2: **Operational principle of a grating coupler (k-vector diagram).**

The angle of the diffracted wave can be calculated using the wave vector of the diffracted wave, and its component in the direction of z, as follows:

$$sin\theta = \frac{k_z}{k}, \tag{B.2}$$

substituting the value of k_z and k, we arrive at a simplified Bragg equation that includes the desired diffraction angle in its respective wavelength:

$$n_{eff} - n_{cld} sin\theta = \frac{\lambda}{\Lambda}, \tag{B.3}$$

and to obtain the diffraction angle in free space, we use Snell's law and we obtain:

$$n_{eff} - sin\theta_{ar} = \frac{\lambda}{\Lambda}. \tag{B.4}$$

Now, if we consider the diffraction in the direction of the substrate, the resulting wave vector diagram stay as illustrated in Fig. B.3. For a perfectly vertical angle, we find that the Bragg relation is simplified to $\Lambda = \lambda/n_{eff}$, where n_{eff} is the average refractive index of the grating, which can be approximated by the weighted average of the etched and unetched region [76, 154]. This is the condition for vertical coupling, shown in Fig. B.3(b). It is denominated as second-order grating because there is also a solution for $m = 2$, so the grating can reflect the light back to the waveguide. Therefore, most practical gratings are designed at a coupling angle of 7°-13° from the vertical.

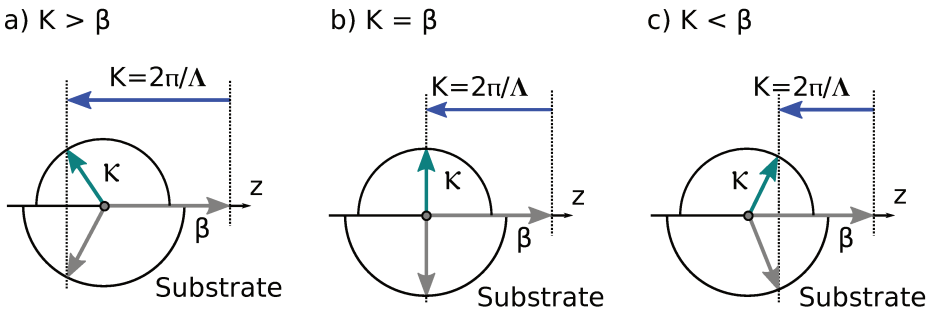

Figure B.3: **k-vector diagram of a grating coupler with different period.** (a) $< 2^{nd}$ order. (b) Exactly 2^{nd} order. (c) $> 2^{nd}$ order. "Reprinted from [26]".

The design of the grating couplers can perform a forward coupling, using a period longer than the second pure order period as seen in Fig. B.3(c) or a backward coupling, with a grid of first order as seen in fig. B.3(a). The gratings usually have a period with an order of magnitude similar to that of a wavelength. Fig. B.4 represents the cross section diagram of a grating coupler engraved on a SOI platform. The thicknesses of the silicon layer and of the BOX layer are determined by the employed wafer type and, therefore, they become design restrictions. The oxide cladding layer used to protect the grating and to enable layers of electrical interconnections, in contrast, can be optimized to improve the overall coupling efficiency.

Several design parameters can be adjusted to design the grating coupler to operate at wavelength (λ) and and diffraction toward the desired angle. The period of the grating (Λ), the fill factor (W/Λ) and the corrosion depth (d), are parameters that can be adjusted according to our needs. To maximize the coupling efficiency, the directionality must be optimized (P_{up}/P_{in}), while decreasing the penetration losses (P_{subs}/P_{in}), the reflected power towards the waveguide (R/P_{in}), and the transmitted power (T/P_{in}). Initially, we calculate the effective index of the two thicknesses of silicon assuming that the grid has an infinite width. This assumption is a good approximation since the width of the typical grating coupler is 11 µm, which is more than 6 times the central wavelength for a grid in the NIR. If we denote the effective index of the grating teeth as n_{eff1}, and the effective index of the grating slots as n_{eff2}, then the effective index of the grating region can be

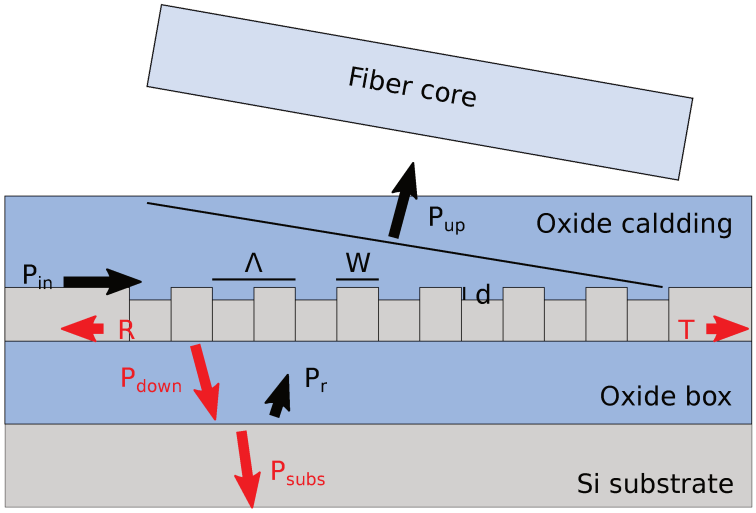

Figure B.4: **Cross-section of a shallow etched grating coupler.**

expressed as:

$$n_{eff} = ff \cdot n_{eff1} + (1 - ff) \cdot n_{eff2}. \tag{B.5}$$

So far we have addressed the design of a uniform grating coupler. With this approach, a taper of hundreds of micrometers will be required to convert the mode of a silicon waveguide from 450 nm to a mode of a silicon waveguide of approximately 10 µm. Consequently, instead of using straight gratings, we can use focused gratings to make the device more compact, as first proposed in [87]. The layout of a focused grating is shown in Fig. B.5, were the grating lines form an ellipse with a common focal point that matches the optical focal point of the coupler.

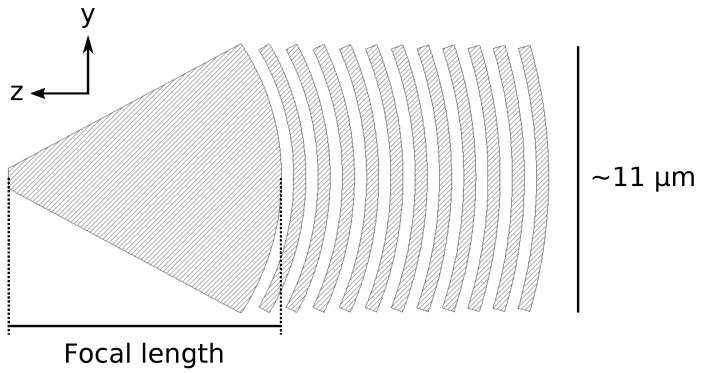

Figure B.5: **Focused grating coupler layout.**

According to [87], a compact focused grating structure can be obtained by following the equation:

$$q\lambda = zn_{cld}cos\theta - n_{eff}(y^2 + z^2)^{1/2}, \quad q = 1, 2..., \tag{B.6}$$

where z is the coordinate in the propagation direction of the mode, y is the coordinate in the lateral direction, and q is the number of the grating line. The focal point is at the origin of the coordinate system. The condition of the Eq. B.6 is valid under the assumption that the effective index of the grating and the waveguide is constant, as follows:

$$n_{eff}^{grt} = n_{eff}^{wg}. \tag{B.7}$$

The Eq. B.6 is only true for shallow grating. Therefore, it represents a second order algebraic equation in y y z. Consequently, the grating lines describe elliptical curved lines with a common ellipse focal point:

$$\frac{\left(z + \frac{q\lambda n_1 cos\theta}{n_{eff}^2 - n_{cld}^2 cos^2\theta}\right)^2}{\left(z + \frac{q\lambda n_{eff}}{n_{eff}^2 - n_{cld}^2 cos^2\theta}\right)^2} + \frac{y}{\left[\frac{q\lambda}{(n_{eff}^2 - n_{cld}^2 cos^2\theta)^{1/2}}\right]^2} = 1. \tag{B.8}$$

Once the theoretical design is finished, we proceed to validate the device with $2d$ simulations, where several sweeps are made in the parameters theoretically obtained to adjust the desired central wavelength. After setting the parameters, a final verification must be done with a $3d$ simulation. After this verification, the layout for manufacturing can be created.

Appendix C

Summary of fabrication recipes

This appendix summarizes the fabrication recipes reported in the chapter 3.

Table C.1: 6 in SOI wafer for Dicing.

Process	Parameters	Description
AZ-4620 spin	45 s at 3000 rpm	e-resist coating
Soft bake	120 s at 110 °C	removes e-resist solvent
Wafer dicing	1.3 cm × 1.3 cm	cuts with a saw at CTI
Chips tape off	3 min at MJB4	remove the dicing chips from the tape

Table C.2: Surface preparation processes.

Process	Parameters	Description
RCA cleaning	$H_2SO_4 + H_2O_2$ (4:1) at 80 °C for 10 min,	removes organic residues
	$HF + H_2O$ (10:1) for 30 s,	removes native SiO_2
	$NH_4OH + H_2O_2 + H_2O$ (1:1:5) at 80 °C for 10 min,	removes some metals
	$HCl + H_2O_2 + H_2O$ (1:1:5) at 80 °C for 10 min,	removes some metals
Oxygen barrel plasma	50 sccm of 0_2	oxygen flow
	100 mTorr	pressure
	350 W	RF power

Table C.3: Spin coating and lithography for MAN-2403.

Process	Parameters	Description
Dehydration	120 °C for 13 min	removes water
HDMS	3000 rpm for 30 s, wait 90 s	adhesion promotion
MAN-2403 spin	3000 rpm for 30 s	e-resist coating
Soft bake	90 °C for 90 s	removes e-resist solvent
Lithography	125 µC/cm^2 for 90 s,	dose
	7 µm,	aperture
	10 nA,	beam current
	100 µm × 100 µm,	write field
	2 nm	step size/line spacing
AZ-300 MIF	3.5 min	develops lithographic pattern
DI water	30 s	rinses AZ-300 MIF
Nitrogen	weak	drying

Table C.4: Pseudo Bosch silicon etch recipe.

Process	Parameters	Description
Oxygen plasma	50 sccm of 0_2	oxygen flow
(cleaning)	15 mTorr	pressure
	15 W	RIE power
	1200 W	RF power
chamber conditioning	12 sccm of SF_6	Sulfur hexafluoride flow
	26 sccm of C_4F_8	Octafluorocyclobutane flow
	15 mTorr	pressure
	15 W	RIE power
	1200 W	RF power
	5 min	time
Silicon ecthing	12 sccm of SF_6	Sulfur hexafluoride flow
(112 nm/min)	26 sccm of C_4F_8	Octafluorocyclobutane flow
	15 mTorr	pressure
	15 W	RIE power
	1200 W	RF power
	2.23 min	time to etch 250 nm

Appendix D

Mode overlap integral

As we saw in the previous sections, the coupling efficiency is one of the most important performance parameters of a coupler. Although several methods have been developed to theoretically calculate the coupling efficiency between a grating coupler and a standard siglemode fiber, simulation is still necessary to model a variety of non-periodic or sub-wavelengths couplers. Then, once the electric and magnetic fields are obtained in the output plane of the simulation, the computation of the mode overlap integral is essential to determine the efficiency of a great variety of optical devices.

Next, we present a detailed derivation of the overlap integral based on [155], first we express the input field as a sum of the propagation modes allowed in the system. Specifically, the basis we will use consists of the electric and magnetic fields of the forward and backward waves, as follows:

$$E = E_{fwd} + E_{back}. \tag{D.1}$$

where the forward and backward components can be written as a superposition of modes:

$$E_{fwd} = \sum_n e_n a_n e^{i\beta_n z}, \tag{D.2}$$

$$E_{back} = \sum_n e_n b_n e^{-i\beta_n z}. \tag{D.3}$$

In the previous expressions, e_n is the electric field profile of the n-th cross section mode of the system. Applying Faraday's Law and assuming harmonic time dependence of the electric field, the magnetic field can also be written as an expansion of the forward and backward waves, as we see below:

$$H = H_{fwd} + H_{back} = \sum_n h_n (a_n e^{i\beta_n z} - b_n e^{-i\beta_n z}). \tag{D.4}$$

In Eq. D.4 the backward propagation term is preceded by a negative sign. This

arises from the requirement that the power flows in the negative direction. In general, given an arbitrary field, we do not know the forward and backward components separately but its sum. Now, to find the coefficients a_n and b_n, we will separate the different forward and backward travelling modes that make up an arbitrary field. To do so, we use the orthogonality condition that emerges as a result of Lorentz reciprocity [156] and is given by:

$$\frac{\int_s (e_n \times h_m^*) \cdot ds}{\int_s (e_n \times h_n^*) \cdot ds} = \delta_{nm}, \tag{D.5}$$

where δ_{mn} is the Kronecker delta. We apply this condition of orthogonality by calculating the surface integral of $e \times h_n^*$ and reorder the terms to generate an expression that relates a_n and b_n to the electric field and the n-th mode, as follows:

$$a_n e^{i\beta_n z} + b_n e^{-i\beta_n z} = \frac{\int_s (e \times h_n^*) \cdot ds}{S_n}, \tag{D.6}$$

where S_n is the power propagated in the n-th mode and is given by:

$$S_n = \int_s (e_n \times h_n^*) \cdot ds. \tag{D.7}$$

A second expression can be found for a_n and b_n by calculating the surface integral of $e_n^* \times h$ is:

$$a_n e^{i\beta_n z} - b_n e^{-i\beta_n z} = \frac{\int_s (e_n^* \times h) \cdot ds}{S_n^*}, \tag{D.8}$$

with two equations and two unknowns, we obtain the following expressions:

$$a_n = \frac{1}{2}\left(\frac{\int_s (e \times h_n^*) \cdot ds}{S_n} + \frac{\int_s (e_n^* \times h) \cdot ds}{S_n^*}\right) e^{-i\beta_n z}. \tag{D.9}$$

$$b_n = \frac{1}{2}\left(\frac{\int_s (e \times h_n^*) \cdot ds}{S_n} - \frac{\int_s (e_n^* \times h) \cdot ds}{S_n^*}\right) e^{-i\beta_n z}. \tag{D.10}$$

Using these equations, we can decompose any given field in the modes of the system by a direct calculation. Now we will determine the coupling efficiency. This efficiency is most conveniently expressed as follows:

$$\eta_n = |a_n|^2 \frac{1/2Re\left\{\int_s (e_n \times h_n^*) \cdot ds\right\}}{1/2Re\left\{\int_s (e \times h^*) \cdot ds\right\}} = |a_n|^2 \frac{P_n}{P_{in}}, \tag{D.11}$$

where P_n is the power in the desired mode, and P_{in} is the input power as seen in Fig. B.4. Eq. D.11 describes the amount of power that can be coupled from an incident field to a desired mode of the system. This expression can be further simplified if the backward wave is not present at the system output. In this case, b_n is equal to zero and we have to:

$$\frac{\int_s (e \times h_n^*) \cdot ds}{S_n} = \frac{\int_s (e_n^* \times h) \cdot ds}{S_n^*}, \tag{D.12}$$

Taking this into account to simplify the eq. D.11 we obtain:

$$\eta_n = \frac{\left| \int_s (e \times h_n^*) \cdot ds \right|^2}{\left| \int_s (e_n \times h_n^*) \cdot ds \right|^2} \frac{Re\left[\int_s (e_n \times h_n^*) \cdot ds \right]}{Re\left[\int_s (e \times h^*) \cdot ds \right]}, \tag{D.13}$$

where e_n and h_n are the field profiles that we want to generate with the coupler. This equation is a more general form of efficiency, however, in many applications e_n and h_n will correspond to a guided mode. Therefore, we can further simplify the expression by observing that the integral $\int_s (e_n \times h_n^*) \cdot ds$ has a real value, therefore we obtain:

$$\eta_n = \left| \int_s (e \times h_n^*) \cdot ds \right|^2 \frac{1}{Re\left\{ \int_s (e_n \times h_n^*) \cdot ds \right\} Re\left\{ \int_s (e \times h^*) \cdot ds \right\}}, \tag{D.14}$$

$$\eta_n = \left| \int_s (e \times h_n^*) \cdot ds \right|^2 \frac{1}{4 P_n P_{in}}. \tag{D.15}$$